



New very high-order upwind multi-layer compact (MLC) schemes with spectral-like resolution for flow simulations

Zeyu Bai*, Xiaolin Zhong

Mechanical and Aerospace Engineering Department, University of California, Los Angeles, CA 90095, USA



ARTICLE INFO

Article history:

Received 24 February 2018

Received in revised form 26 October 2018

Accepted 29 October 2018

Available online 6 November 2018

Keywords:

High-order methods

Spectral-like resolution

Multi-layer compact scheme

Upwind scheme

Finite difference

Hypersonic boundary-layer transition

ABSTRACT

Numerical simulations of multi-scale flow problems such as hypersonic boundary layer transition, turbulent flows, computational aeroacoustics and various other flow problems with complex physics require high-order methods with high spectral resolutions. For instance, the receptivity mechanisms in the hypersonic boundary layer are the resonant interactions between forcing waves and boundary-layer waves, and the complex wave interactions are difficult to be accurately predicted by conventional low-order numerical methods. High-order methods, which are robust and accurate in resolving a wide range of time and length scales, are required. Currently, the high-order finite difference methods for simulations of hypersonic flows are usually upwind schemes or compact schemes with fifth-order accuracy or lower [1]. The objective of this paper is to develop and analyze a new very high-order numerical scheme with the spectral-like resolution for flow simulations on structured grids, with focus on smooth flow problems involving multiple scales. Specifically, a new upwind multi-layer compact (MLC) scheme with spectral-like resolution up to seventh order is derived in a finite difference framework. By using the ‘multi-layer’ idea, which introduces first derivatives into the MLC schemes and approximates the second derivatives, the resolution of the MLC schemes can be significantly improved within a compact grid stencil. The auxiliary equations are required and they are the only nontrivial equations, which contributes to good computational efficiency. In addition, the upwind MLC schemes are derived based on the idea of constructing upwind schemes on centered stencils with adjustable parameters to control the dissipation. Fourier analysis is performed to show that the MLC schemes have small dissipation and dispersion in a very wide range of wavenumbers in both one- and two-dimensional cases, and the anisotropic error is much smaller than conventional finite difference methods in the two-dimensional case. Furthermore, the stability analysis with matrix method shows that high-order boundary closure schemes are stable because of compactness of the stencils. The accuracies and rates of convergence of the new schemes are validated by numerical experiments of the linear advection equation, the nonlinear Euler equations, and the Navier–Stokes equations. The numerical results show that good computational efficiency, very high-order accuracies, and high spectral resolutions especially on coarse meshes can be attained with the MLC schemes. Overall, the MLC scheme has the properties of simple formulations, high-order accuracies, spectral-like resolutions, and compact stencils, and it is suitable for accurate simulation of smooth multi-scale flows with complex physics.

© 2018 Elsevier Inc. All rights reserved.

* Corresponding author.

E-mail addresses: zeyubai21@engineering.ucla.edu (Z. Bai), xiaolin@seas.ucla.edu (X. Zhong).

1. Introduction

In the recent few decades, direct numerical simulation (DNS) has become one of the most important methods for the numerical study of various fluid dynamics problems with multiple scales and complex physics. An example is the prediction of the laminar-turbulent transition of hypersonic boundary layers, which is critically important to the development of hypersonic vehicles that are to be used for rapid space access [2]. In general, the transition is a result of the nonlinear response of a laminar boundary layer to various environmental disturbances, but transition mechanisms of hypersonic and supersonic boundary layers are much more complex and much less understood compared with incompressible flows. The transition of hypersonic boundary layers over blunt bodies, which are representative examples, can be affected by the additional effects of shock waves, entropy-layer instabilities, nose bluntness and thermochemical nonequilibrium at high temperatures [3]. As a natural consequence, the DNS of hypersonic boundary layer requires highly accurate numerical methods to resolve a wide range of time and length scales in the flow. At the end of the transition process, the boundary layer becomes fully turbulent, which are more complicated than laminar or transitional flows. The investigation of turbulent flows still face many difficulties because of the strong nonlinearity, the large number of degrees of freedom (DOFs), high sensitivity to small differences in flow conditions, and many other factors [4]. The numerical simulation of turbulent flows is even more challenging because of the wide range and flat distribution of energy spectrum, and the instantaneous range of scales in turbulent flows increases rapidly with the Reynolds number [5]. However, due to the limitation of computational resources, it is impossible to resolve all the tiny structures in turbulent flows for practical Reynolds numbers. To accurately simulate the turbulent flows, it is required the numerical methods should resolve a significant portion of the scales in the flow fields on feasible grid resolutions. Computational aeroacoustics [6] is another instance which involves complex physics. The generation and propagation of acoustic waves have different features from common aerodynamic problems. In aeroacoustics, the frequency range of acoustic waves is wide, and their amplitude is very small compared with mean flow properties. Meanwhile, flows that generate noises are nonlinear, unsteady and turbulent. These features make the accurate simulation of acoustic wave propagation challenging especially in far-field that requires long-time integration [7]. A common feature of all the flow problems above is the multiple scales embedded in the fields which are difficult to be captured with schemes of low-order accuracy. In the DNS investigation of multi-scale flow problems, the schemes should have very high-order accuracy and high spectral resolution for a wide range of wavelength scales. Moreover, the numerical dissipation and dispersion of such high-order schemes should be low enough to ensure that physical wave components with small amplitude are not suppressed or distorted, which is particularly important in computational aeroacoustics.

High-order methods have received increasing attention for flow simulations. They have the advantage of achieving the desired accuracy with fewer grid points in the computational domain, improving the computational efficiency, saving the required computer memory, and facilitating large simulations. For these reasons, the high-order methods such as spectral methods, and high-order compact schemes have been commonly used in DNS of turbulent flows [8]. There are many high-order numerical methods developed in the past few decades. Ekaterinaris [9] presented a comprehensive review of the development of high-order methods with low numerical diffusion. Wang [10] discussed high-order methods with emphasize on unstructured grids. Roughly speaking, high-order methods can be classified as linear schemes and nonlinear schemes. Linear schemes, such as spectral methods [11–13], discontinuous-Galerkin (DG) methods [14–17], high-order finite difference methods [1,18–22], etc., are mainly designed for smooth flows without discontinuities. There exist other flow problems with discontinuities such as shock waves. For simulation of these flows, nonlinear schemes, such as TVD [23,24], ENO [25], WENO [26,27], etc., are designed. These are also hybridizations of linear and nonlinear schemes, which combine the advantages of both methods [28–31].

The conventional numerical methods for multi-scale problems have been the spectral methods [11–13], which are especially suitable for incompressible turbulent flow. Spectral methods use modal basis functions of orthogonal polynomials, such as Fourier series, to represent the solution in the entire computational domain, which leads to very high spectral resolutions and exponential convergence. However, high-order spectral methods have been limited to flows with simple geometries and face difficulties when dealing with complicated boundary conditions. In addition, spectral methods are less accurate for compressible flow problems, such as hypersonic boundary layer where the critical layer is important.

In an effort to simulate flows over complex geometries more accurately, many discontinuous finite element methods have been developed, such as discontinuous-Galerkin (DG) methods [14–17], spectral difference (SD) methods [32–34], and spectral volume (SV) methods [35–38], etc. These methods use the localized function representation within each element, hence they are suitable to deal with flows over very complex geometries with unstructured grids. Among them, discontinuous-Galerkin (DG) methods may receive the most attention. DG methods combine the characteristics of finite volume methods and finite element methods by using high-order piecewise polynomials within elements and solving numerical fluxes on element interfaces. They have very high-order accuracy and there is no reconstruction needed in DG methods because the entire trial function with multiple degrees of freedom (DOFs) is evolved. Whatever the order of accuracy is, the local stencil can be attained. In other words, each element only interacts with its neighboring elements, which makes DG methods very efficient for parallel computing. However, high-order DG methods have much more degrees of freedom in trial functions, especially for multi-dimensional simulations. Storing and evolving these extra degrees of freedom require larger memory and more CPU time compared with finite volume methods, although they save some computational cost on reconstructions [8].

Compared with other high-order methods, finite difference methods have the advantages of simple formulations and high computational efficiencies with the precondition that the geometry is relatively simple and structured grid can be

used. However, conventional explicit finite difference schemes face difficulty in resolving the short waves, which limits their applications in multi-scale problems such as boundary layer transition, turbulent flows, etc. To relax this constraint, finite difference schemes with spectral-like resolutions have been widely investigated. The compact finite difference scheme [18,19,21,39–44] is an influential alternative. Lele [18] performed extensive analysis on compact finite difference schemes and showed that through the implicit relation between the derivatives and function values on several grid points, the error in large wavenumber region is reduced and resolutions for short waves are improved. The spectral properties can be further improved by imposing the wavenumber constraints at certain points, i.e., let the modified wavenumber equal to the exact wavenumber at these points. Simultaneously, the maximal truncation order is abandoned on a stencil. Compared with spectral methods, compact schemes are also more flexible with complex geometries and boundary conditions. Lele's compact schemes have been extended by Chu & Fan [22,44] and Mahesh [19], by introducing the second derivatives in the implicit difference equation. The resulting scheme, which is termed the combined compact difference (CCD) scheme, can achieve higher orders in accuracy and have better spectral resolution than the normal compact schemes on the same stencils. The dispersion-relation-preserving (DRP) scheme [45–49] is another widely used finite difference scheme with the spectral-like resolution. Tam and Webb [49] first proposed the DRP scheme by optimizing an explicit finite difference approximation in the wavenumber and frequency space, minimizing the L_2 norm error in modified wavenumbers, hence achieved spectral-like resolution. The general idea of these optimizing finite difference schemes is to lower the error at marginal resolution related to high-frequency wave at the expense of allowing more error for low-frequency wave [50]. Another main difficulty in applying high-order finite difference methods is the numerical instability from boundaries when used on solid wall boundary layer [51]. The stencil is usually wide for high-order finite difference methods and it is difficult to construct stable boundary closure schemes. In most DNS studies of transitional and turbulent flows of the boundary layer, the orders of numerical methods are often limited due to the numerical instability from boundaries. Many approaches have been proposed to improve the stability of boundary conditions in high-order finite difference methods. Zhong [1] showed that using an adjustable parameter to control dissipation in inner schemes would stabilize the boundary conditions. The non-uniform grid schemes proposed by Zhong and Tatineni [51] use an appropriate grid stretching and cluster grid points near the boundary to attain stable high-order boundary closure schemes. Ashcroft & Zhang [40] and Hixon [41] derived prefactored compact schemes which require smaller stencils and offer simpler boundary condition. By narrowing the grid stencil, the boundary closure schemes can be simplified because narrower boundary stencils are required, which is commonly known as the main advantage of stencil compactness.

The high-order methods discussed above are linear schemes designed for smooth flows. They usually have difficulties in capturing discontinuities, such as shock wave, where they produce spurious oscillations known as the Gibbs phenomenon. For flows with shock, shock-capturing methods based on nonlinear schemes are required. Total-variation-diminishing (TVD) [23], essentially-nonscillatory (ENO) [25], and weighted-essentially-nonscillatory (WENO) [26] schemes are representative examples of nonlinear schemes. Many advanced nonlinear schemes have been developed from these ideas or their variations [8–10,52,53]. In past twenty years, WENO-based methods receive the most attention among nonlinear schemes. The core idea of WENO scheme is using low-order polynomials and adaptive stencils in reconstruction. The high-order numerical flux or conserved variable is approximated as a weighted summation of low-order polynomials. By using smoothness indicators and automatically selecting the optimal stencil, WENO scheme can achieve very high-order accuracy in the smooth region and maintain nonoscillatory property across shock waves in the discontinuous region. Shu [54] presented a detailed review of the development of high-order WENO schemes. There are three general problems exist in most nonlinear schemes. First, nonlinear schemes are usually computationally expensive. Second, the accuracy near the shock is reduced because the shock location is only known to $O(h)$ on a finite grid [53]. Last, their performance in the smooth region is not as good as linear schemes due to excessive damping [53]. Although WENO-based schemes can achieve very high-order accuracies in a smooth region, they generate large phase error when resolving small waves in multi-scale flow simulations. In fact, spectral-like resolution can only be achieved by linear schemes as mentioned by Hill & Pullin [55] and Taylor et al. [56]. As a result, these nonlinear schemes may not be accurate enough for DNS studies of hypersonic boundary layers, where short wavelength shock/disturbance interactions need to be resolved with high accuracy [1]. As an alternative approach to deal with shocks, shock-fitting methods [1,57–59] have been used to treat the bow shock as a computational boundary and the flow region behind the shock can be simulated with high-order linear schemes.

This paper presents a new very high-order upwind multi-layer compact (MLC) scheme with the spectral-like resolution which is based on the finite difference framework. The features of the new method include: (i) the multi-layer framework to reduce stencil size, increase order of accuracy, and improve resolution; (ii) the centered grid stencil for upwind schemes and the adjustable parameter to control numerical dissipation; (iii) the explicit finite difference formula derived on uniform structured grids; (iv) the linear approximation to maintain low computational costs and spectral-like resolution for multi-scale smooth flows.

As the main aspect of our new methods, the multi-layer scheme in this paper refers to a numerical approximation on a layered grid stencil which includes the value layer and derivative layers. Both the value and derivatives are used for approximations of higher derivatives, i.e., every grid point has multiple degrees of freedom (DOFs). Most conventional finite difference and finite volume methods can be considered as mono-layer schemes because the only DOF is the value on every grid point. In our multi-layer scheme, the auxiliary equation is introduced and both value and first derivatives are treated as unknowns. There are two DOFs in one-dimensional simulations, three in two-dimensional simulations, and four in three-dimensional simulations. The original governing equation becomes an exact equation and only approximation for

auxiliary equations are required, which is a benefit for computational efficiency. Details of the methods will be presented in Section 2.

Researchers have developed many numerical methods with multiple degrees of freedom, which is similar to the multi-layer idea in our new scheme. Discontinuous-Galerkin (DG) methods are a typical example, in which the degrees of freedom (DOFs) in each element is determined by the order of accuracy. Orthogonal basis functions are usually utilized to construct the high-order piecewise polynomials within the element, and all the weights of the basis are solved as unknowns. To increase the order, more DOFs are added in each element. All unknowns in DG methods are numerical quantities, so there is no exact equation in the formulations. This feature becomes a major difference in methodology with the proposed MLC scheme. Spectral difference (SD) methods [32–34] and spectral volume (SV) methods [35–38] also have multiple DOFs in each element, they are similar to DG methods but the way the piecewise polynomials are constructed is different. SV methods define the sub-cells and the averaged conservative variables in these sub-cells are DOFs, while SD methods define the solution points within each element and point values are DOFs [10]. These point or sub-cell values are then used to construct polynomials. DG methods and other finite element methods usually have high-order accuracy and can be easily applied to flow simulations over complex geometries with unstructured grids, and they are very compact because the high-order polynomials are defined, and no reconstructions are required. However, they require a large number of memories, especially in multi-dimensional simulations. In addition, controlling of numerical oscillations in the vicinity of strong discontinuities remains one of challenging issues in these methods.

The idea of evolving multiple degrees of freedom has also appeared in finite volume or finite difference methods. Qiu and Shu, et al. developed a fifth-order Hermite WENO (HWENO) scheme [60–62] in the finite volume framework, where both function value and its first derivative is evolved in time and used in the reconstruction. Balsara et al. [63] also used HWENO approach in their hybrid RKDG+HWENO schemes, where a monotonicity preserving strategy that is scale-free and problem-independent for detecting troubled zones is proposed. They proved that they are good alternatives with lower storage and narrower stencils to Runge–Kutta Discontinuous Galerkin (RKDG) schemes. Luo et al. [64–66] did extensive work on the HWENO schemes with a focus on unstructured grids. They applied HWENO approach as limiters to both original discontinuous-Galerkin (DG) methods and reconstructed DG methods and found that it can save computational cost, enhance accuracy, and ensure linear stability. The major advantage of these HWENO approaches is compactness of stencils in reconstructions, so they are also very suitable as limiters for discontinuous-Galerkin methods.

There are still many other numerical methods where the use of multiple degrees of freedom can be found. Chang et al. [67–69] proposed the space–time conservation element and solution element (CE/SE) method which includes a unified treatment of spatial and temporal discretization in the space–time domain. The core of the CE/SE method is the two-level, explicit and non-dissipative scheme so the stencil is minimized while maintaining accuracy. Sundar and Yeo [70] designed a meshless method for attaining high-order approximation with compact support by using high-order information at nodes for solution reconstruction. They avoided the trouble of a very large set of supporting points required in conventional meshless methods, thus, successfully increased the accuracy to sixth order. Nishikawa [71–74] developed the first-order hyperbolic system (FOHS) for solving diffusion and advection–diffusion problems. By introducing an additional equation for first derivatives using a relaxation technique, the diffusion term is formulated in a hyperbolic way. An upwind scheme can be applied to the entire system, which leads to a uniform order of accuracy and faster convergence.

In general, the numerical schemes with multiple degrees of freedom (DOFs) attain benefits from their compact support stencil, leading to better efficiency for parallel computing and simpler stable boundary conditions. Most of the methods mentioned above utilized this desirable feature to improve their performance. On the other hand, using multiple DOFs in a linear scheme leads to an additional advantage of a better spectral resolution for small wave components. A prominent explanation can be obtained from Fourier analysis that the resolving ability of a linear scheme depends mainly on degrees of freedom on each grid, i.e. the upper limit of wavenumber (k_{max}) that can be resolved is determined by DOFs (K) through the relation $k_{max} = K\pi$. As mentioned in the previous part of the introduction, it has been a long history to improve spectral resolutions of finite difference methods, and most of the work follows the idea of Lele [18]. They improve the spectral resolution through the implicit relation between derivatives and values in a stencil, but they still face a limit of $k_{max} = \pi$. At the same time, many of these methods comprise the formal order when pursuing better marginal resolution, which is not good for global accuracy. As a comparison, in finite element methods such as discontinuous-Galerkin (DG) methods, the resolution limit k_{max} increases with the order of accuracy benefit from multiple DOFs. This gives us the inspiration to construct a new finite difference method with spectral-like resolution using the multi-layer approach without comprising the order of accuracy. Also, the compact stencil is attained as other numerical methods with multiple DOFs which benefits the construction of boundary closure schemes.

It should be noted that our multi-layer idea differs from the combined compact difference (CCD) scheme [19,22,44] on the role these additional derivatives play and how they are updated. In CCD scheme, the use of second derivatives provides additional implicit relations but does not increase the DOFs. Both first and second derivatives are solved simultaneously from their implicit formulas. While in our MLC schemes, the use of the first derivative provides additional DOFs and each DOF is solved separately from a discrete equation. As a result, the multi-layer idea further improves the resolution. It has been noticed that the first derivative and its auxiliary equation are also used in Nishikawa's method [71–74]. However, the auxiliary equation is derived in a relaxation technique, so the approximation still applies to the first derivatives. While in our new method, the auxiliary equation is derived directly from the original equation by taking its gradients, so the

approximation will apply to the second derivatives. As for the motivation, Nishikawa used the first derivative and additional equation to unify the advection and diffusion term, while our purpose is to improve the spectral resolution.

The second aspect of the current multi-layer compact (MLC) schemes is the construction of upwind scheme based on a centered grid stencil with an adjustable parameter to control dissipation. Most high-order finite difference methods used in direct numerical simulation (DNS) are central difference schemes which introduce only phase errors but no dissipative errors in numerical solutions. However, central schemes are not robust enough for convection dominated flows such as supersonic and hypersonic flows. On the other hand, upwind schemes have been widely investigated because of their robustness and they have received much attention in convection dominated flows. In our very high-order upwind MLC schemes, the idea of centered-stencil upwind schemes with an adjustable parameter proposed by Zhong [1] is followed to stabilize the MLC schemes and maintain low dissipation. The main philosophy behind this idea is to attain the upwind schemes so that the dissipative errors are smaller than the dispersive errors inherent in equivalent central schemes and are large enough to stabilize high-order inner schemes coupled with boundary closure schemes. The orders of accuracies of the upwind schemes are one order lower than the highest orders the centered stencils can achieve so that there is an adjustable parameter in the leading dissipative truncation term.

The third aspect of our methods is the use of finite difference approximation based on uniform structured grids. One of the major areas of application of our MLC schemes is the direct numerical simulation of laminar-turbulent boundary layer transition. Although the physics is complex because of a wide range of scales in these flows, the geometries are usually relatively simple such as flat plates, conical cones and blunt bodies with circular or parabolic cross-sections. Smooth curvilinear meshes can be used to discretize the computational domain. So, our MLC scheme is constructed in the finite difference framework which has simple formulations and good computational efficiencies on structured grids.

The fourth aspect of our methods is the use of the linear approximation. As summarized in the previous part of the introduction, high-order linear schemes with spectral-like resolution would be ideal for DNS studies of multi-scale flows in the smooth region. They have smaller dissipation and can achieve better spectral resolution compared with nonlinear schemes. In the simulation for supersonic or hypersonic flow over blunt bodies where the bow shock exists, the smooth region behind the shock can be solved by high-order linear schemes and shock-fitting methods can be applied to capture the bow shocks. In the shock-fitting method of Zhong [1], the bow shock can be treated as a moving computational boundary so that the discontinuity across the shock is avoided. The transient shock location and movement are solved as part of the solutions together with the Navier–Stokes equations. The flow variables immediately behind the shock are determined by Rankine–Hugoniot relation and a characteristic compatibility equation from the flow field behind the shock. Different variations of shock-fitting methods are discussed in [59]. In the future, the shock-fitting methods will be extended to the MLC schemes for direct numerical simulation of hypersonic flows.

In summary, the goal of developing the new schemes is to accurately simulate smooth multi-scale flows with complex physics but over simple geometries. Besides the laminar-turbulent boundary layer transition simulations, the new schemes should also be valuable for other multi-scale flows such as turbulence and computational aeroacoustics. The advantages of the present scheme include the very high-order accuracy and high spectral resolution; the simplicity of the explicit finite difference approximations; the compact stencils and simple boundary closure schemes.

The paper is organized as follows. In Section 2, the derivations of the current new very high-order upwind multi-layer compact (MLC) schemes are illustrated in one-dimensional and two-dimensional cases respectively. The MLC schemes with up to seventh-order accuracy are presented. In Section 3, the Fourier analysis and stability analysis for boundary closure schemes is carried out to show the high-order accuracy and spectral-like resolution of the MLC schemes. The effect of adjustable damping parameters in upwind schemes is analyzed. In Section 4, the accuracies of the schemes are assessed on the linear advection equation, the nonlinear Euler equations, and the Navier–Stokes equations with multiple test cases in one and two dimensions. In Section 5, the summary and main conclusions of this paper are given.

2. Very high-order upwind multi-layer compact (MLC) schemes

The hypersonic boundary layer transition and other compressible viscous flow problems are governed by the Navier–Stokes equations, which can be written in the following conservation-law form in the Cartesian coordinate,

$$\frac{\partial U}{\partial t} + \frac{\partial F_j}{\partial x_j} + \frac{\partial F_{vj}}{\partial x_j} = 0 \quad (1)$$

where U , F_j , and F_{vj} are the vectors of conservative variables, inviscid convective flux, and viscous flux in the direction of x_j respectively,

$$U = [\rho, \rho u_1, \rho u_2, \rho u_3, E_t]^T \quad (2)$$

$$F_j = \begin{bmatrix} \rho u_j \\ \rho u_1 u_j + p \delta_{1j} \\ \rho u_2 u_j + p \delta_{2j} \\ \rho u_3 u_j + p \delta_{3j} \\ (E_t + p) u_j \end{bmatrix} \quad (3)$$

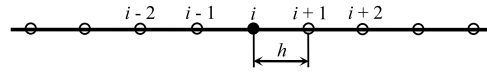


Fig. 1. A uniform mesh for conventional finite difference approximations.

$$F_{vj} = \begin{bmatrix} 0 \\ \tau_{1j} \\ \tau_{2j} \\ \tau_{3j} \\ \tau_{ij}u_i + q_j \end{bmatrix} \quad (4)$$

In a wide range of temperature and pressure, the perfect gas assumption can be used, and the total energy per unit volume E_t is calculated from,

$$E_t = \frac{p}{\gamma - 1} + \frac{1}{2} \rho u_k u_k \quad (5)$$

In Eq. (4), τ_{ij} is the viscous stress which has the form,

$$\tau_{ij} = -\mu \left(\frac{\partial u_i}{\partial x_j} + \frac{\partial u_j}{\partial x_i} \right) - \lambda \frac{\partial u_k}{\partial x_k} \delta_{ij} \quad (6)$$

where μ is the molecular viscosity coefficient and λ is second viscous coefficient which is usually assumed to be $-2\mu/3$. The heat flux q_j in Eq. (4) is calculated from,

$$q_j = -\kappa \frac{\partial T}{\partial x_j} \quad (7)$$

where the heat conductivity coefficient κ is computed through a constant Prandtl number $Pr = 0.72$ as follows,

$$\kappa = \frac{C_p}{Pr} \mu = \frac{\gamma R}{(\gamma - 1) Pr} \mu \quad (8)$$

The Navier–Stokes equations reduce to the Euler equations, which are the governing equations for inviscid flows and $F_{vj} = 0$.

The method of lines can be used to discretize the governing equations by separating spatial and temporal discretization. The main difficulty in the spatial discretization is the approximation of the hyperbolic-type convective term in Eq. (1), which plays an important role in numerical stability. To construct a stable numerical algorithm, the high-order upwind scheme is commonly utilized to discretize the convective term. Meanwhile, the elliptic-type viscous flux term in the Navier–Stokes equations can be approximated by high-order central schemes. Therefore, in the remaining part of the section, the focus is mainly on the derivation and analysis of the convective term.

In this paper, a family of very high-order upwind multi-layer compact (MLC) schemes is derived and presented which are applied to the discretization of inviscid flux term in the Euler equations, and both the inviscid and viscous flux terms in the Navier–Stokes equations. The model equation of the inviscid Euler equations is linear advection equation, which is used to illustrate the derivation of the very high-order MLC schemes.

2.1. One-dimensional MLC schemes

The one-dimensional advection equation is used to introduce the very high-order upwind MLC scheme for one-dimensional simulations,

$$\frac{\partial u}{\partial t} + c \frac{\partial u}{\partial x} = 0, \quad a \leq x \leq b \quad (9)$$

where it is assumed that the wave speed c is a positive constant. Downwind schemes for $c < 0$ can be easily obtained from upwind schemes. The computational domain for one-dimensional wave propagation is a periodic domain in the range of $a \leq x \leq b$, where two boundaries located in $x = a$ and $x = b$ can be either periodic or non-periodic. In the spatial discretization of Eq. (9), a uniform mesh with a grid spacing h is used, as presented in Fig. 1. Conventional finite difference schemes use only value u_i in each node to approximate the first derivative $\partial u / \partial x$. Therefore, the grid stencil is usually wide for high-order schemes which may cause difficulty on numerical stability and boundary closure schemes. There are different methods which can reduce stencil size including the influential work of Lele [18].

In this paper, we present a new MLC scheme which achieves both high-order accuracy and high spectral resolution within a compact stencil. In the new methods, the additional governing equation for the first derivatives is introduced by taking the gradient of Eq. (9), and the resulting Eq. (10) is called the auxiliary equation,

$$\frac{\partial u'}{\partial t} + c \frac{\partial u'}{\partial x} = 0 \quad (10)$$

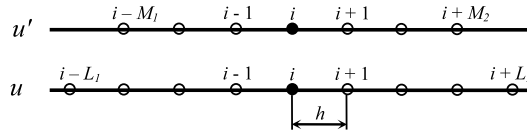


Fig. 2. Stencil of the L_1 - L_2 - M_1 - M_2 scheme for second derivative approximations.

Equations (9) and (10) form a system of partial differential equations in the following form,

$$\frac{\partial}{\partial t} \begin{bmatrix} u \\ u' \end{bmatrix} = -c \begin{bmatrix} u' \\ u'' \end{bmatrix} \tag{11}$$

where u and u' are treated as unknowns. Therefore, there are two degrees of freedom (DOFs) at each grid point. Instead of approximating the first derivative $\partial u / \partial x$ in Eq. (9) in conventional finite difference scheme, the MLC schemes only need the approximation of u'' in the right-hand side of Eq. (11) to solve the unknowns (u, u'). The original advection equation showed in Eq. (9) needs no spatial discretization because u' is solved at each grid point. Therefore, the computational cost is not significantly increased although the MLC scheme involves two equations for the one-dimensional advection problem. To solve the system of equations, finite difference approximation for u'' ($= \partial u' / \partial x$) in Eq. (11) are needed and it can be constructed from u_i and u'_i . Because there are two DOFs at each grid point, higher-order accuracy and better spectral resolution can be obtained in a smaller stencil, which is presented in the following part of this section.

Same uniform mesh with grid spacing h , as shown in Fig. 1, is used in the MLC approximations. For a base point i , the approximation of u'' is of the form,

$$\left(\frac{\partial u'}{\partial x} \right)_i = u''_i = \frac{1}{h^2} \sum_{l=-L_1}^{L_2} a_l u_{i+l} + \frac{1}{h} \sum_{m=-M_1}^{M_2} b_m u'_{i+m} - \frac{\alpha}{(p+2)!} u_i^{p+2} h^p + \dots \tag{12}$$

$$p = L_1 + L_2 + M_1 + M_2 - 1 \tag{13}$$

where there is a summation of u_{i+l} and u'_{i+m} with coefficients a_l and b_m , which can be derived from the Taylor series expansion with respect to base point i . In Eq. (12), u_{i+l} , u'_{i+m} , and u''_i are exact solutions at grid points. In the truncation error term, p is the order of accuracy, and α is the coefficient of leading truncation error term. If the truncation error term is taken out, Eq. (12) can be considered as a finite difference approximation and u_{i+l} , u'_{i+m} , and u''_i becomes approximate solutions. For simplicity, we use same symbols for exact and approximate variables in this paper. The corresponding stencil is shown in Fig. 2, which shows a value layer and first derivative layer. A total of $L_1 + L_2 + 1$ grid points are picked in the value layer, with L_1 points on the upwind side and L_2 points on the downwind side with respect to the base point i . Similarly, $M_1 + M_2 + 1$ points are used in the derivative layer, with M_1 points on the upwind side and M_2 points on the downwind side. A scheme with this grid stencil is termed the L_1 - L_2 - M_1 - M_2 scheme in this paper. In the derivation of the inner scheme, the centered stencils ($L_1 = L_2, M_1 = M_2$) are used, and both upwind schemes and central schemes are constructed on the same centered stencils.

The maximum order that the approximation in Eq. (12) can achieve is $L_1 + L_2 + M_1 + M_2$, while in the upwind scheme, p is set to be $L_1 + L_2 + M_1 + M_2 - 1$, which means the coefficient of the leading truncation term α is a free parameter in the coefficients a_l and b_m . All schemes with nonzero α have a p -th order of accuracy, and the maximum $(p + 1)$ -th order is obtained when $\alpha = 0$. The choice of α is not unique, and the value and sign of α play important roles in the magnitude of numerical dissipation and stability of the numerical scheme. The stability of a high-order scheme is critical when applying it to discretize the inviscid flux terms. Meanwhile, deriving a low dissipative upwind scheme is a common goal for accuracy and spectral resolution requirement. Therefore, the value of α needs to be large enough to make the MLC scheme stable and needs to be relatively small to control the dissipation error. Positive or negative α lead to upwind or downwind schemes. It should be noted that the sign of α of upwind schemes varies with the stencils. The idea of adjustable α is similar to what is presented in [1].

Several specific MLC schemes with various orders of accuracy and grid stencils are presented in this section. First, the third-order 1-1-1-1 scheme and the seventh-order 2-2-2-2 scheme are discussed, and they are analyzed and tested comprehensively later in this paper. The fifth-order 2-2-1-1 and 1-1-2-2 scheme are also presented, as examples where stencils for value and derivative layers are different.

1-1-1-1 scheme (3rd order)

Using a three-point stencil in both value and first derivative layers as shown in Fig. 3, the 1-1-1-1 scheme can be derived as,

$$\left(\frac{\partial u'}{\partial x} \right)_i = u''_i = \frac{1}{h^2} \sum_{l=-1}^1 a_l u_{i+l} + \frac{1}{h} \sum_{m=-1}^1 b_m u'_{i+m} - \frac{\alpha}{5!} u_i^5 h^3 + \dots \tag{14}$$

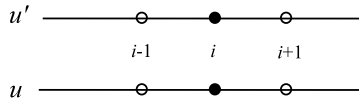


Fig. 3. Stencil of the 1-1-1-1 scheme (3rd order) for second derivative approximations.

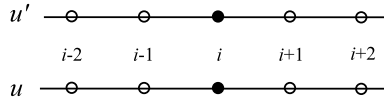


Fig. 4. Stencil of the 2-2-2-2 scheme (7th order) for second derivative approximations.

$$\begin{aligned}
 a_{\pm 1} &= 2 \mp \frac{3}{4}\alpha, & a_0 &= -4, \\
 b_{\pm 1} &= \mp \frac{1}{2} + \frac{1}{4}\alpha, & b_0 &= \alpha,
 \end{aligned}
 \tag{15}$$

where α is the free parameter in coefficients a_l and b_m . The formula leads a third-order upwind scheme when $\alpha > 0$, and it recovers to the fourth-order central scheme when $\alpha = 0$. As a benefit of the multi-layer idea, compactness of grid stencil is achieved. In this case, the third-order upwind scheme or fourth-order central scheme is constructed on the three-point stencil. As a comparison, the grid for conventional finite difference schemes of the same order of accuracy is much wider. For example, a five-point stencil is required in Zhong’s third-order upwind scheme or fourth-order central scheme [1].

Different α values lead to different stability conditions and numerical dissipation which affects accuracy and spectral resolution. In this paper, the recommended value of α in Eq. (15) is chosen based on Fourier analysis results in Section 3.1. The value of α for the 1-1-1-1 scheme is 1.5, and the corresponding third-order 1-1-1-1 scheme is,

$$\left(\frac{\partial u'}{\partial x}\right)_i = u''_i = \frac{1}{h^2} \left(\frac{25}{8}u_{i-1} - 4u_i + \frac{7}{8}u_{i+1} \right) + \frac{1}{h} \left(\frac{7}{8}u'_{i-1} + \frac{3}{2}u'_i - \frac{1}{8}u'_{i+1} \right)
 \tag{16}$$

By choosing some specific α values, the 1-1-1-1 scheme can reduce to upwind schemes on bias stencils. For example, if $\alpha = 2$, then b_1 in Eq. (15) is zero and the algorithm reduces to the 1-1-1-0 scheme. Similarly, if $\alpha = 8/3$, then a_1 in Eq. (15) is zero and the algorithm reduces to the 1-0-1-1 scheme. Both schemes have larger α values than the recommend value 1.5. Fourier analysis in Section 3.1 will show that a larger α leads to more dissipation. Therefore, the upwind scheme on a bias stencil is more dissipative than the 1-1-1-1 upwind scheme on a centered stencil.

2-2-2-2 scheme (7th order)

Similarly, using a five-point stencil in both value and first derivative layers as shown in Fig. 4, the 2-2-2-2 scheme can be derived as,

$$\left(\frac{\partial u'}{\partial x}\right)_i = u''_i = \frac{1}{h^2} \sum_{l=-2}^2 a_l u_{i+l} + \frac{1}{h} \sum_{m=-2}^2 b_m u'_{i+m} - \frac{\alpha}{9!} u_i^9 h^7 + \dots
 \tag{17}$$

$$\begin{aligned}
 a_{\pm 2} &= \frac{7}{54} \mp \frac{25}{3456}\alpha, & a_{\pm 1} &= \frac{64}{27} \mp \frac{5}{108}\alpha, & a_0 &= -5, \\
 b_{\pm 2} &= \mp \frac{1}{36} + \frac{1}{576}\alpha, & b_{\pm 1} &= \mp \frac{8}{9} + \frac{1}{36}\alpha, & b_0 &= \frac{1}{16}\alpha.
 \end{aligned}
 \tag{18}$$

The formula leads to a seventh-order upwind scheme when $\alpha > 0$, and it recovers to the eighth-order central scheme when $\alpha = 0$. Compactness of grid stencil is significant in this 2-2-2-2 scheme compared with conventional finite difference methods. For example, a nine-point stencil is required in Zhong’s seventh-order upwind scheme or eighth-order central scheme [1], while only five points are used in the MLC scheme.

Again, the recommended value of α in Eq. (18) is chosen based on Fourier analysis results in Section 3.1. The optimal value of α for the 2-2-2-2 scheme is 12, and the corresponding seventh-order 2-2-2-2 scheme is,

$$\begin{aligned}
 \left(\frac{\partial u'}{\partial x}\right)_i = u''_i &= \frac{1}{h^2} \left(\frac{187}{864}u_{i-2} + \frac{79}{27}u_{i-1} - 5u_i + \frac{49}{27}u_{i+1} + \frac{37}{864}u_{i+2} \right) \\
 &+ \frac{1}{h} \left(\frac{7}{144}u'_{i-2} + \frac{11}{9}u'_{i-1} + \frac{3}{4}u'_i - \frac{5}{9}u'_{i+1} - \frac{1}{144}u'_{i+2} \right)
 \end{aligned}
 \tag{19}$$

By choosing some specific α values, the 2-2-2-2 scheme can also reduce to upwind schemes on bias stencils. For example, if $\alpha = 16$, then b_2 in Eq. (18) is zero and the algorithm reduces to the 2-2-2-1 scheme. Similarly, if $\alpha = 448/25$, then a_2

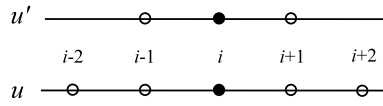


Fig. 5. Stencil of the 2-2-1-1 scheme (5th order) for second derivative approximations.

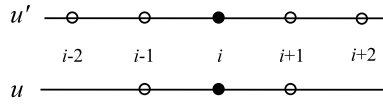


Fig. 6. Stencil of the 1-1-2-2 scheme (5th order) for second derivative approximations.

in Eq. (18) is zero and the algorithm reduces to the 2-1-2-2 scheme. Again, both scheme has larger α values than the recommended value 12, which means they are more dissipative.

2-2-1-1 scheme (5th order)

The stencils in the value layer and the derivative layer can be different in the MLC schemes. For example, using five-point stencil for values and three-point stencil for first derivatives as shown in Fig. 5, the 2-2-1-1 scheme can be derived as,

$$\left(\frac{\partial u'}{\partial x}\right)_i = u''_i = \frac{1}{h^2} \sum_{l=-2}^2 a_l u_{i+l} + \frac{1}{h} \sum_{m=-1}^1 b_m u'_{i+m} - \frac{\alpha}{7!} u''_i h^5 + \dots \tag{20}$$

$$\begin{aligned} a_{\pm 2} &= \frac{1}{36} \pm \frac{1}{144} \alpha, & a_{\pm 1} &= \frac{20}{9} \pm \frac{7}{36} \alpha, & a_0 &= -\frac{9}{2}, \\ b_{\pm 1} &= \mp \frac{2}{3} - \frac{1}{12} \alpha, & b_0 &= -\frac{1}{4} \alpha. \end{aligned} \tag{21}$$

Here, α needs to be negative for upwind schemes. The formula leads to a fifth-order upwind scheme when $\alpha < 0$, and it recovers to the sixth-order central scheme when $\alpha = 0$. The compactness of grid stencil in this 2-2-1-1 scheme is also achieved compared with conventional finite difference schemes. For example, the seven-point stencil is required in Zhong’s fifth-order upwind scheme or sixth-order central scheme [1], while only five points are used in the MLC scheme.

By choosing some specific α values, the 2-2-1-1 scheme can also reduce to upwind schemes on bias stencils. For example, if $\alpha = -4$, then a_2 in Eq. (20) is zero and the algorithm reduces to 2-1-1-1 scheme as,

$$\left(\frac{\partial u'}{\partial x}\right)_i = u''_i = \frac{1}{h^2} \left(\frac{1}{18} u_{i-2} + 3u_{i-1} - \frac{9}{2} u_i + \frac{13}{9} u_{i+1} \right) + \frac{1}{h} \left(u'_{i-1} + u'_i - \frac{1}{3} u'_{i+1} \right) \tag{22}$$

Similarly, if $\alpha = -8$, then b_1 in Eq. (20) is zero and the algorithm reduces to 2-2-1-0 scheme as,

$$\left(\frac{\partial u'}{\partial x}\right)_i = u''_i = \frac{1}{h^2} \left(\frac{1}{12} u_{i-2} + \frac{34}{9} u_{i-1} - \frac{9}{2} u_i + \frac{2}{3} u_{i+1} - \frac{1}{36} u_{i+2} \right) + \frac{1}{h} \left(\frac{4}{3} u'_{i-1} + 2u'_i \right) \tag{23}$$

1-1-2-2 scheme (5th order)

The stencils in the derivative layer can be wider than that in the value layer in MLC schemes. For example, using three-point stencil for values and five-point stencil for first derivatives as shown in Fig. 6, the 1-1-2-2 scheme can be derived as,

$$\left(\frac{\partial u'}{\partial x}\right)_i = u''_i = \frac{1}{h^2} \sum_{l=-1}^1 a_l u_{i+l} + \frac{1}{h} \sum_{m=-2}^2 b_m u'_{i+m} - \frac{\alpha}{7!} u''_i h^5 + \dots \tag{24}$$

$$\begin{aligned} a_{\pm 1} &= \frac{24}{11} \pm \frac{3}{20} \alpha, & a_0 &= -\frac{48}{11}, \\ b_{\pm 2} &= \pm \frac{1}{132} + \frac{1}{600} \alpha, & b_{\pm 1} &= \mp \frac{20}{33} - \frac{17}{300} \alpha, & b_0 &= -\frac{19}{100} \alpha. \end{aligned} \tag{25}$$

Like the case of fifth-order 2-2-1-1 scheme, α also needs to be negative for upwind schemes. It should be noted that although both the 1-1-2-2 and 2-2-1-1 schemes have fifth-order of accuracy, their stability can be different. According to our experience in simulations, the 1-1-2-2 scheme would be less stable than 2-2-1-1 scheme. So, it is recommended to use a wider stencil in the value layer, if not the same, than that in the derivative layer.

With one-dimensional MLC schemes, all the spatial derivatives in Eq. (11) can be approximated and discretized. The spatial discretization of Eq. (11) leads to a system of first-order ordinary differential equations,

$$\frac{d\bar{\mathbf{U}}}{dt} = \mathcal{L}(\bar{\mathbf{U}}, t) \quad (26)$$

where $\bar{\mathbf{U}}$ is the discretized flow field variables including function values u_i and first derivatives u'_i , and \mathcal{L} is the approximate operator for spatial discretization through MLC schemes. Time-dependent boundary conditions may be included in Eq. (26). The explicit Runge–Kutta schemes can be used to integrate the system of equations in time. For example, the solution procedure from t^n to t^{n+1} using classical fourth-order Runge–Kutta method (RK4) is,

$$\mathbf{k}_1 = dt\mathcal{L}(\bar{\mathbf{U}}^n, t^n) \quad (27)$$

$$\mathbf{k}_2 = dt\mathcal{L}\left(\bar{\mathbf{U}}^n + \frac{\mathbf{k}_1}{2}, t^n + \frac{dt}{2}\right) \quad (28)$$

$$\mathbf{k}_3 = dt\mathcal{L}\left(\bar{\mathbf{U}}^n + \frac{\mathbf{k}_2}{2}, t^n + \frac{dt}{2}\right) \quad (29)$$

$$\mathbf{k}_4 = dt\mathcal{L}(\bar{\mathbf{U}}^n + \mathbf{k}_3, t^n + dt) \quad (30)$$

$$\bar{\mathbf{U}}^{n+1} = \bar{\mathbf{U}}^n + \frac{\mathbf{k}_1}{6} + \frac{\mathbf{k}_2}{3} + \frac{\mathbf{k}_3}{3} + \frac{\mathbf{k}_4}{6} \quad (31)$$

2.2. Two-dimensional MLC schemes

The advection equation is also used as the model equation to illustrate the construction of the very high-order upwind MLC schemes in multi-dimensional cases. The advection equation in three-dimensional flow is,

$$\frac{\partial u}{\partial t} + (\mathbf{c} \cdot \nabla)u = 0 \quad (32)$$

where, u is a scalar, and $\mathbf{c} = (c_1, c_2, c_3)$ is a constant vector representing the velocity. For simplicity, only the two-dimensional case is discussed here, and three-dimensional case follows the same methodology. In Cartesian grids, it can be written in scalar form as follows,

$$\frac{\partial u}{\partial t} + c_1 u_x + c_2 u_y = 0 \quad (33)$$

Then, two auxiliary equations are introduced by taking derivatives of Eq. (33) with respect to x and y ,

$$\frac{\partial(u_x)}{\partial t} + c_1 u_{xx} + c_2 u_{xy} = 0 \quad (34)$$

$$\frac{\partial(u_y)}{\partial t} + c_1 u_{xy} + c_2 u_{yy} = 0 \quad (35)$$

Equations (33)–(35) form a system of partial differential equations as follows,

$$\frac{\partial}{\partial t} \begin{bmatrix} u \\ u_x \\ u_y \end{bmatrix} = -c_1 \begin{bmatrix} u_x \\ u_{xx} \\ u_{xy} \end{bmatrix} - c_2 \begin{bmatrix} u_y \\ u_{xy} \\ u_{yy} \end{bmatrix} \quad (36)$$

where u , u_x , u_y are treated as unknowns. Therefore, there are three degrees of freedom (DOFs) at each grid point. The system of equations (36) is solved by the method of lines simultaneously. Same as the one-dimensional case, the original equation (33) needs no approximation because u_x and u_y are part of the solution. On the other hand, u_{xx} , u_{xy} , u_{yy} in auxiliary equations (34) and (35) need approximations through the MLC schemes. Thus, there are three equations to solve and three terms to approximate, while conventional finite difference method only solves Eq. (33) and approximates two terms (u_x , u_y). However, the computational costs are not increased significantly, because much fewer grid points are needed in multi-dimensional simulations with our MLC schemes due to their spectral-like resolutions.

The second derivative terms u_{xx} , u_{yy} in Eq. (36) are approximated in the same way as the one-dimensional case, and all the formulas in Section 2.1 can be applied. On the other hand, the cross-derivative term u_{xy} , which is not present in one-dimensional MLC schemes, needs to be estimated through another multi-layer approximation based on the similar idea as one-dimensional cases. Discretized function values $u_{i,j}$ and first derivatives $(u_x)_{i,j}$, $(u_y)_{i,j}$ are available for the approximation. Different from one-dimensional MLC schemes, stencils for cross derivatives in two-dimensional MLC schemes are squares in the (x, y) plane, which include the corner points. Fig. 7 shows the stencil of the L_1 - L_2 - M_1 - M_2 scheme for cross derivatives, where the value layer contains $(L_1 + L_2 + 1)^2$ grid points and the first derivative layer contains $(M_1 + M_2 + 1)^2$ grid points. The centered stencil is used which is similar to one-dimensional stencils. In other words, the base point (i, j) is always located in the center of the square, and both u_x and u_y use the same stencil shown in Fig. 7(b). Consequently, the projection of this stencil on either axis is identical with the stencil for one-dimensional MLC schemes in Fig. 2.

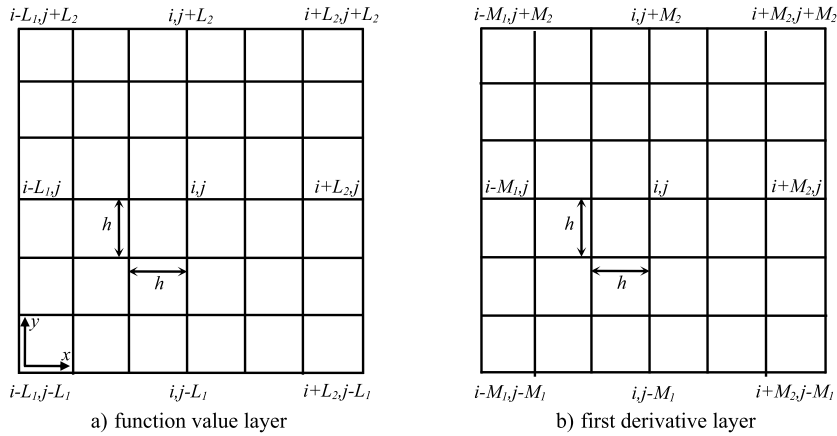


Fig. 7. Stencil of the $L_1-L_2-M_1-M_2$ scheme for cross derivative approximations.

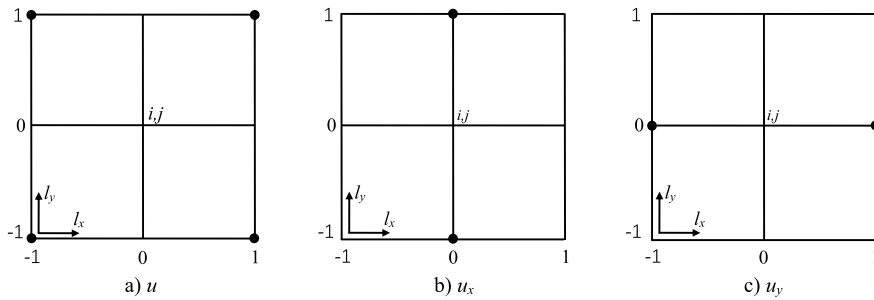


Fig. 8. Stencil and supporting points of the 1-1-1-1 scheme (4th order) for cross derivative approximations.

The approximation can be derived from the following equation,

$$(u_{xy})_{i,j} = \frac{1}{h^2} \sum_{\substack{l_x=-L_2 \\ l_y=-L_1}}^{L_2} a_{l_x,l_y} u_{i+l_x,j+l_y} + \frac{1}{h} \sum_{\substack{m_x=-M_1 \\ m_y=-M_1}}^{M_2} b_{m_x,m_y} (u_x)_{i+m_x,j+m_y} + \frac{1}{h} \sum_{\substack{n_x=-M_1 \\ n_y=-M_1}}^{M_2} c_{n_x,n_y} (u_y)_{i+n_x,j+n_y} + o(h^{p+1}) \tag{37}$$

where p is given in Eq. (13), and it is the order of corresponding one-dimensional upwind MLC scheme. It is noted that the $L_1-L_2-M_1-M_2$ scheme has the same maximum order of accuracy in one- and two-dimensional case, which is $p + 1$. In Eq. (37), the scheme with the maximum order of accuracy is derived. The truncation error term is a summation of multiple higher derivatives.

The coefficients a, b, c in Eq. (37) can be derived by multivariate Taylor series expansion with respect to base point (i, j) . In the approximations for cross derivatives, there are many freedoms due to redundant points in a square stencil. As a result, the resulting linear system of equations from Taylor series is underdetermined, and the solution of a, b, c is not unique although the maximum order has been used in Eq. (37). To get a unique solution, we must preselect supporting points for both values and derivatives before solving the coefficients. In other words, only the coefficients for preselected points are unknowns, and the coefficients for other points are set to be zero. In our derivation, the goal is to find the simplest formula which contains the fewest non-zero terms and the most concise coefficients. On the other hand, only the central scheme is used to approximate the cross derivatives, because the upwind setting for cross derivatives can be cumbersome and complicated. The results of numerical tests in this paper show that central schemes for cross derivatives are stable when coupled with one-dimensional upwind schemes. Because they are one order higher than upwind schemes, they can maintain the overall accuracy of one-dimensional upwind schemes.

Several specific MLC schemes for cross derivatives are presented in this section. Same as the one-dimensional case, the 1-1-1-1 scheme, the 2-2-2-2 scheme, the 2-2-1-1 scheme, and the 1-1-2-2 scheme are derived. All of them are one order higher than their corresponding one-dimensional upwind schemes.

1-1-1-1 scheme (4th order)

The stencil to approximate the cross derivative u_{xy} for the 1-1-1-1 scheme is shown in Fig. 8. The maximum order of accuracy achievable in this stencil is 4. To get a unique and simplest solution of coefficients a, b, c in Eq. (37), supporting

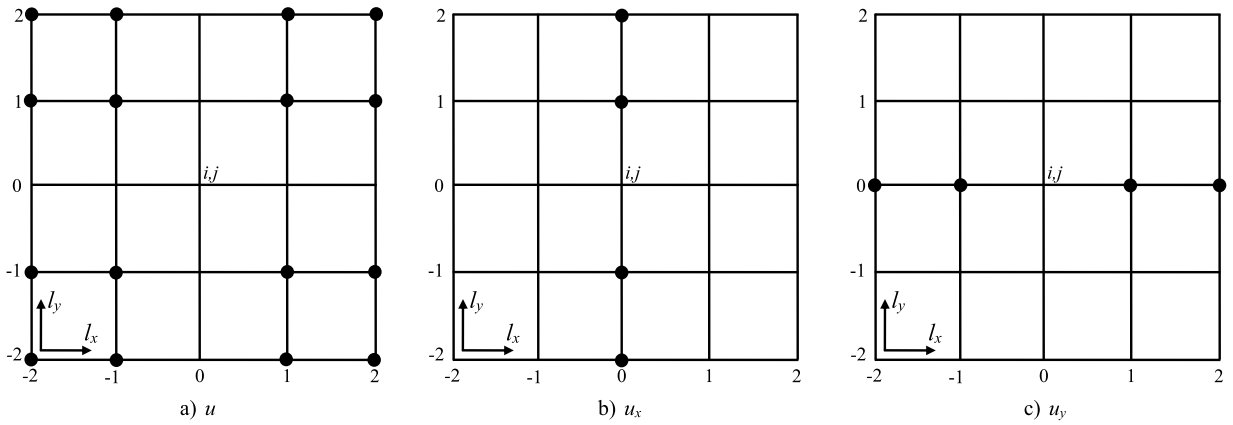


Fig. 9. Stencil and supporting points of the 2-2-2-2 scheme (8th order) for cross derivative approximations.

points for values and first derivatives are preselected and marked with black dots in Fig. 8. All the points on the corner are used to provide information of u and all the points along the central x and y lines are used to provide information of u_y and u_x respectively. In total, four value points, two x derivative points, and two y derivative points are preselected. It is noted that the points are distributed symmetrically, which is the requirement of central schemes.

Using Taylor series expansion, the specific formula for this fourth-order 1-1-1-1 scheme is derived as follows,

$$(u_{xy})_{i,j} = \frac{1}{h^2} \left(-\frac{1}{4}u_{i-1,j-1} + \frac{1}{4}u_{i+1,j-1} + \frac{1}{4}u_{i-1,j+1} - \frac{1}{4}u_{i+1,j+1} \right) + \frac{1}{h} \left(-\frac{1}{2}(u_x)_{i,j-1} + \frac{1}{2}(u_x)_{i,j+1} \right) + \frac{1}{h} \left(-\frac{1}{2}(u_y)_{i-1,j} + \frac{1}{2}(u_y)_{i+1,j} \right) \quad (38)$$

In the derivation of cross derivatives, all possible formulas with the fourth-order accuracy have been searched. It turns out Eq. (38) has the simplest form with the fewest non-zero terms and the most concise coefficients.

2-2-2-2 scheme (8th order)

Similarly, the stencil and preselected supporting points to approximate the cross derivative u_{xy} for the 2-2-2-2 scheme are shown in Fig. 9. The maximum order of accuracy achievable in this stencil is 8. A similar methodology is followed as in the 1-1-1-1 scheme to attain the simplest formula. All the points which are not on the central x and y lines are used to provide information of u , and points on central x and y lines are used to provide information of u_y and u_x respectively. In total, sixteen value points, four x derivative points, and four y derivative points are preselected.

Using Taylor series expansion, the specific formula for this eighth-order 2-2-2-2 scheme is derived as follows,

$$(u_{xy})_{i,j} = \frac{1}{h^2} \left(-\frac{1}{144}u_{i-2,j-2} + \frac{1}{18}u_{i-1,j-2} - \frac{1}{18}u_{i+1,j-2} + \frac{1}{144}u_{i+2,j-2} + \frac{1}{18}u_{i-2,j-1} - \frac{4}{9}u_{i-1,j-1} + \frac{4}{9}u_{i+1,j-1} - \frac{1}{18}u_{i+2,j-1} \right) - \frac{1}{18}u_{i-2,j+1} + \frac{4}{9}u_{i-1,j+1} - \frac{4}{9}u_{i+1,j+1} + \frac{1}{18}u_{i+2,j+1} + \frac{1}{144}u_{i-2,j+2} - \frac{1}{18}u_{i-1,j+2} + \frac{1}{18}u_{i+1,j+2} - \frac{1}{144}u_{i+2,j+2} \right) + \frac{1}{h} \left(\frac{1}{12}(u_x)_{i,j-2} - \frac{2}{3}(u_x)_{i,j-1} + \frac{2}{3}(u_x)_{i,j+1} - \frac{1}{12}(u_x)_{i,j+2} \right) + \frac{1}{h} \left(\frac{1}{12}(u_y)_{i-2,j} - \frac{2}{3}(u_y)_{i-1,j} + \frac{2}{3}(u_y)_{i+1,j} - \frac{1}{12}(u_y)_{i+2,j} \right) \quad (39)$$

Again, Eq. (39) has the simplest form with the fewest non-zero terms and the most concise coefficients among all possible formulas with eighth-order accuracy.

2-2-1-1 scheme (6th order)

The stencils for values and derivatives can also be different in two-dimensional MLC schemes as well. For example, 2-2-1-1 scheme has a 25-point square stencil for values and a 9-point square stencil for first derivatives. Consequently, the maximum order of accuracy achievable is 6. The stencil and preselected supporting points to approximate the cross derivative u_{xy} for the 2-2-1-1 scheme are shown in Fig. 10. The way the supporting points are selected here is different from the 1-1-1-1 or 2-2-2-2 schemes. Only the diagonal points are selected as supporting points. In total, eight value points, four x derivative points, and four y derivative points are preselected.

Using Taylor series expansion, the specific formula for this sixth-order 2-2-1-1 scheme is derived as follows,

$$(u_{xy})_{i,j} = \frac{1}{h^2} \left(\frac{1}{144}u_{i-2,j-2} - \frac{1}{144}u_{i+2,j-2} + \frac{5}{9}u_{i-1,j-1} - \frac{5}{9}u_{i+1,j-1} - \frac{5}{9}u_{i-1,j+1} + \frac{5}{9}u_{i+1,j+1} - \frac{1}{144}u_{i-2,j+2} + \frac{1}{144}u_{i+2,j+2} \right)$$

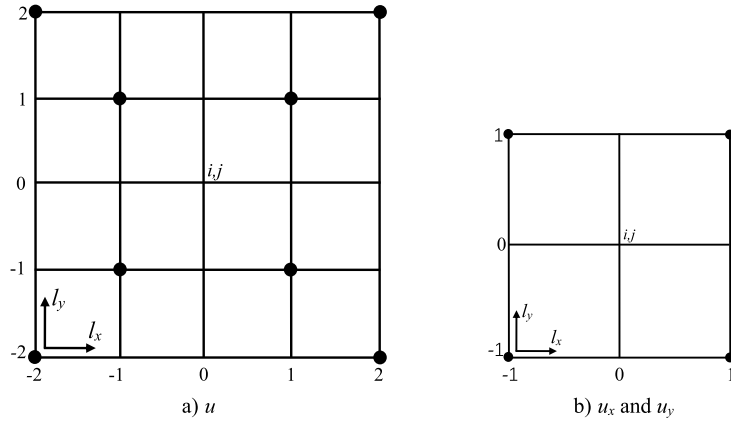


Fig. 10. Stencil and supporting points of the 2-2-1-1 scheme (6th order) for cross derivative approximations.

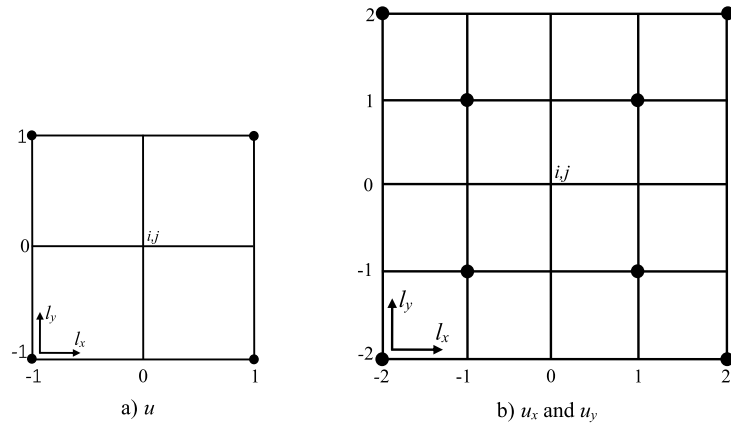


Fig. 11. Stencil and supporting points of the 1-1-2-2 scheme (6th order) for cross derivative approximations.

$$\begin{aligned}
 & + \frac{1}{h} \left(\frac{1}{6}(u_x)_{i-1,j-1} + \frac{1}{6}(u_x)_{i+1,j-1} - \frac{1}{6}(u_x)_{i-1,j+1} - \frac{1}{6}(u_x)_{i+1,j+1} \right) \\
 & + \frac{1}{h} \left(\frac{1}{6}(u_y)_{i-1,j-1} - \frac{1}{6}(u_y)_{i+1,j-1} + \frac{1}{6}(u_y)_{i-1,j+1} - \frac{1}{6}(u_y)_{i+1,j+1} \right)
 \end{aligned} \tag{40}$$

1-1-2-2 scheme (6th order)

Similar to the situation in one-dimensional MLC schemes, we can use a wider stencil in the derivative layer than the value layer. For example, 1-1-2-2 scheme has a 9-point square stencil for values and a 25-point square stencil for first derivatives. The maximum order of accuracy achievable is 6. The stencil and preselected supporting points to approximate the cross derivative u_{xy} for the 1-1-2-2 scheme are shown in Fig. 11. The preselected supporting points are the same as 2-2-1-1 scheme, i.e., only the diagonal points are selected. In total, four value points, eight x derivative points, and eight y derivative points are preselected.

Using Taylor series expansion, the specific formula for this sixth-order 1-1-2-2 scheme is derived as follows,

$$\begin{aligned}
 (u_{xy})_{i,j} = & \frac{1}{h^2} \left(\frac{6}{11}u_{i-1,j-1} - \frac{6}{11}u_{i+1,j-1} - \frac{6}{11}u_{i-1,j+1} + \frac{6}{11}u_{i+1,j+1} \right) \\
 & + \frac{1}{h} \left(-\frac{1}{528}(u_x)_{i-2,j-2} - \frac{1}{528}(u_x)_{i+2,j-2} + \frac{5}{33}(u_x)_{i-1,j-1} + \frac{5}{33}(u_x)_{i+1,j-1} - \frac{5}{33}(u_x)_{i-1,j+1} \right. \\
 & \left. - \frac{5}{33}(u_x)_{i+1,j+1} + \frac{1}{528}(u_x)_{i-2,j+2} + \frac{1}{528}(u_x)_{i+2,j+2} \right) \\
 & + \frac{1}{h} \left(-\frac{1}{528}(u_y)_{i-2,j-2} + \frac{1}{528}(u_y)_{i+2,j-2} + \frac{5}{33}(u_y)_{i-1,j-1} - \frac{5}{33}(u_y)_{i+1,j-1} + \frac{5}{33}(u_y)_{i-1,j+1} \right. \\
 & \left. - \frac{5}{33}(u_y)_{i+1,j+1} - \frac{1}{528}(u_y)_{i-2,j+2} + \frac{1}{528}(u_y)_{i+2,j+2} \right)
 \end{aligned} \tag{41}$$

Although 1-1-2-2 scheme and 2-2-1-1 scheme have the same order of accuracy, Eq. (41) has more terms than Eq. (40) which means the computational efficiency will be lower, and the coefficients are more trivial. Consistent with one-dimensional MLC scheme, it is recommended to use a wider stencil in the value layer, if not the same, than the derivative layer.

With one-dimensional and two-dimensional MLC schemes, all the spatial derivatives in Eq. (36) can be approximated and discretized. Same as one-dimensional case, the spatial discretization of Eq. (36) leads to a system of first-order ordinary differential equations. Explicit Runge–Kutta schemes can be applied to the system of equations, and solution procedures are the same as the one-dimensional case in Section 2.1.

3. Fourier and stability analysis of MLC schemes

3.1. One-dimensional Fourier analysis

The dissipative and dispersive errors of the upwind MLC schemes applied to advection equation (11) are investigated by the Fourier analysis. The trial solutions in Fourier mode are of the following form,

$$\begin{bmatrix} u \\ u' \end{bmatrix} = \begin{bmatrix} \hat{u} \\ \hat{u}' \end{bmatrix} e^{\hat{a}t + i\hat{k}x} \quad (42)$$

where \hat{k} is the wavenumber, and \hat{a} is a complex characteristic parameter as a function of \hat{k} . If a uniform mesh with spacing h is used, the Fourier modes can also be written in discrete form as,

$$\begin{bmatrix} u_i \\ u'_i \end{bmatrix} = \begin{bmatrix} \hat{u} \\ \hat{u}' \end{bmatrix} e^{\hat{a}t + i\hat{k}x_i} \quad (43)$$

where $x_i = x_0 + ih$. The temporal derivative is assumed to be exact and does not introduce any error. Using the L_1 - L_2 - M_1 - M_2 scheme given by Eq. (12) with the stencil in Fig. 2 to discretize the spatial derivative u'' , the advection equation (11) becomes two semi-discrete equations as follows,

$$\frac{d}{dt} u_i + c u'_i = 0 \quad (44)$$

$$\frac{d}{dt} u'_i + \frac{c}{h} \left(\frac{1}{h} \sum_{l=-L_1}^{L_2} a_l u_{i+l} + \sum_{m=-M_1}^{M_2} b_m u'_{i+m} \right) = 0 \quad (45)$$

where u_{i+l} and u'_{i+m} can be represented in discrete Fourier modes according to Eq. (43) in this analysis,

$$u_{i+l} = \hat{u} e^{\hat{a}t + i\hat{k}(x_i + lh)} \quad (46)$$

$$u'_{i+m} = \hat{u}' e^{\hat{a}t + i\hat{k}(x_i + mh)} \quad (47)$$

Substituting Eqs. (46) and (47) into Eq. (44) leads to the following relation between \hat{u} and \hat{u}' ,

$$\hat{u}' = -\frac{\hat{a}}{c} \hat{u} \quad (48)$$

Then, substituting Eqs. (46) and (47) into Eq. (45) and using the relation in Eq. (48) results in a quadratic characteristic equation for a ,

$$a^2 + Ba + C = 0 \quad (49)$$

where a is the non-dimensional dissipation factor defined as,

$$a = R\left(\frac{\hat{a}h}{c}\right) - i \cdot I\left(\frac{\hat{a}h}{c}\right) \quad (50)$$

Operators R and I represent taking real and imaginary parts respectively, and B and C are complex constants dependent on the specific choice of the MLC schemes and wavenumber \hat{k} , as given below,

$$B = \sum_{m=-M_1}^{M_2} b_m e^{-imh\hat{k}}, \quad C = - \sum_{l=-L_1}^{L_2} a_l e^{-ilh\hat{k}} \quad (51)$$

Equation (49) has two complex solutions,

$$a_{1,2} = \frac{-B \pm \sqrt{B^2 - 4C}}{2} \quad (52)$$

where one is the physical mode, and the other is spurious mode. The real part $R(a)$ is a dissipation factor which is related to stability and dissipative error, and the imaginary part $I(a)$ is the modified wavenumber and it can reveal the dispersive error. Meanwhile, the exact solution of a can be derived by substituting Eq. (42) into Eq. (11),

$$a_{exc} = i\hat{k}h = ik \tag{53}$$

where k is the non-dimensional wavenumber. Since there are two solutions of a for the new MLC scheme, we use a_1 to represent the physical mode, and a_2 to represent the spurious mode. The physical mode a_1 should be as close as possible to a_{exc} for better accuracy. From the following formula,

$$a_1 - a_{exc} = R(a_1) + i(I(a_1) - k) \tag{54}$$

it is required that $R(a_1)$ is small to reduce dissipative error, and $I(a_1)$ is close to k for small dispersive error. On the other hand, $R(a_1)$ and $R(a_2)$ should be non-positive to ensure the stability of the MLC scheme. Meanwhile, $R(a_2)$ is related to the stiffness of the MLC scheme. If its magnitude is too large, the numerical problem will be too stiff.

Before we present the Fourier analysis results for MLC schemes, the benefit of introducing the derivative layer can be briefly explained through aliasing in the discrete domain. At an arbitrary time, the Fourier mode sampled at the grid point x_i can be represented as,

$$u_i = \hat{u}e^{i(kn+\varphi)} = \hat{u}[\cos(kn + \varphi) + i \sin(kn + \varphi)] \tag{55}$$

where n is the index of grid point x_i , and φ is a time-dependent real number. Without the derivative layer, the Fourier mode with a different wavenumber

$$k_{alias} = k + 2N\pi \tag{56}$$

can produce the same samples, where N can be any integer. When the mode is reconstructed from these samples, the reconstructed wavenumber k_{rec} is the k_{alias} with the smallest magnitude. As a result, only the k in $[-\pi, \pi]$ can be corrected reconstructed from the sample values. Specifically, the following relation can be obtained,

$$k_{rec} = \begin{cases} k, & k \in (0, \pi] \\ k - 2\pi, & k \in (\pi, 2\pi] \end{cases} \tag{57}$$

Therefore, the wave components with $k > \pi$ cannot be resolved by a mono-layer scheme like conventional finite difference methods, because these waves cannot be represented correctly in the discrete domain. The aliasing is the main reason limiting the marginal resolution of finite difference methods. However, with the introducing of the derivative layer in our MLC schemes, another sample is generated at the grid point x_i ,

$$u'_i = k\hat{u}e^{i(kn+\varphi+\pi/2)}/h = k\hat{u}[-\sin(kn + \varphi) + i \cos(kn + \varphi)]/h \tag{58}$$

Because the magnitude of derivatives is dependent on k , Fourier modes with different k 's cannot generate the same samples. In another word, the aliasing is avoided. Therefore, the small waves with large k 's can also be represented correctly in the discrete domain, which makes it possible to resolve them with the MLC schemes. More discussion about the spectral resolution is presented in the Fourier analysis results.

Fourier analysis of the seventh-order 2-2-2-2 scheme

In the first place, the seventh-order 2-2-2-2 scheme is analyzed using the approach presented above. Fig. 12 presents the Fourier analysis results for the 2-2-2-2 scheme with a typical α value of 12, where the results of Zhong's sixth-order and fifth-order compact scheme with $\alpha = 0$ and -1 , and Zhong's fifth-order explicit scheme with $\alpha = -6$ [1] are also presented for comparison. Here, only physical mode a_1 is plotted for the MLC scheme. Fig. 12(a) shows that all these schemes are stable with non-positive dissipation factors. Zhong's sixth-order central scheme with $\alpha = 0$ has no dissipation and coincides with the exact solution. With upwind setting, all schemes become dissipative for large k . Compared with Zhong's explicit scheme, Zhong's compact scheme has smaller dissipation when $k < 2.4$, however, the dissipation grows rapidly and surpass explicit scheme for large k . Both schemes have the largest dissipation when $k = \pi$. On the other hand, the 2-2-2-2 scheme is much less dissipative in all the plotted k range compared with Zhong's compact and explicit schemes, which indicates a better accuracy as well.

Fig. 12(b) compares the modified wavenumbers of these schemes, where the straight line represents the exact wavenumber. As expected, Zhong's compact schemes with two different α values have a better resolution than Zhong's explicit scheme. However, the accuracies of these 3 schemes decrease rapidly as k increases and drop to zero at $k = \pi$, which is the maximum resolution that most explicit and compact finite difference scheme can achieve in theory. On the other hand, the 2-2-2-2 scheme shows a very high resolution for $k > \pi$, which is similar to the resolution of spectral methods. That means the MLC scheme is much more accurate for resolving flow with very small wavelengths. In other words, it can compute the wave solutions accurately with much fewer grid points per period. This advantage in the resolution of the new

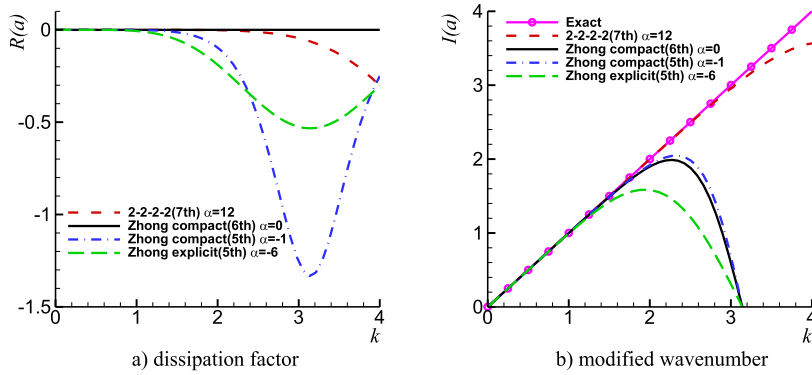


Fig. 12. Fourier analysis results of the 2-2-2 scheme (7th order), in comparison with Zhong's compact scheme (5th and 6th order) and Zhong's explicit scheme (5th order) [1]. (For interpretation of the colors in the figure(s), the reader is referred to the web version of this article.)

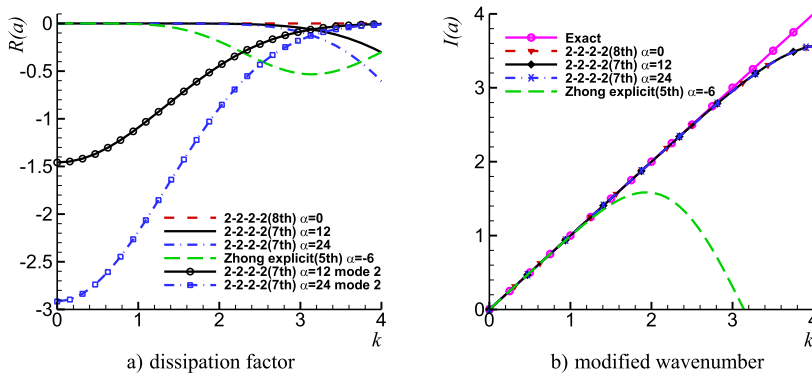


Fig. 13. Fourier analysis results of the 2-2-2 scheme (7th order) with different upwind coefficients.

MLC schemes is due to additional degrees of freedom contained in each grid point, i.e., both the point value and its first derivative. It should be noted that both the seventh-order 2-2-2-2 scheme and Zhong's fifth-order explicit scheme use the explicit formula, but the former is constructed on a five-point grid stencil while the latter needs a seven-point stencil. In other words, the resolution of the 2-2-2-2 scheme is much better on a shorter stencil, which validates the idea that the MLC scheme can reach very high-order accuracy and spectral-like resolution within a compact stencil.

The effects of different α values on the accuracy of the 2-2-2-2 scheme are presented. The choice of α has an impact on dissipation, dispersion, and stiffness of the numerical schemes. Fig. 13 presents the Fourier analysis results for three different 2-2-2-2 schemes with $\alpha = 0, 12, 24$, where the result of Zhong's fifth-order explicit scheme with $\alpha = -6$ is presented for comparison. To analyze the effect of α on stiffness, the dissipation factor of spurious mode – $R(a_2)$ of the 2-2-2-2 scheme is also presented. Different from $R(a_1)$, which are consistent with exact solution for small k and deviate for large k , $R(a_2)$ show large dissipation for small k . This behavior benefits the accuracy of the scheme because the spurious wave will damp out in the simulation when grid resolution is good enough. Another important information revealed by $R(a_2)$ is the restriction on the time step size in the temporal discretization or termed the stiffness of the scheme. It is well known from the numerical analysis theory that $|\hat{a}\Delta t|$ should fall into the stability region of time integration scheme if the resulting ordinary differential equation is discretized by explicit methods such as Runge–Kutta methods. Since $R(a_2)$ is much larger than $R(a_1)$, $I(a_1)$, and $I(a_2)$ in magnitude when k is small, the stiffness of the scheme is mainly determined by $R(a_2)$. A larger magnitude of $R(a_2)$ indicates a smaller time step size Δt under the same stability condition, i.e., the integral of the resulting ordinary differential equation is more restrictive in terms of choosing time step size. Fig. 13(a) shows that larger upwind coefficient α makes $R(a_2)$ much more dissipative for small k , which should result in more restrictive time step size. In addition, larger α also make $R(a_1)$ more dissipative for large k , which can affect the accuracy when small length wave is important in the flow.

On the other hand, Fig. 13(b) shows that 2-2-2-2 schemes with different upwind coefficients have similar resolutions in terms of wavenumber. All of them are much better than Zhong's fifth-order explicit scheme. In summary, α should be large enough to ensure stability, but not too large to avoid stiffness and keep small dissipation. For seventh-order 2-2-2-2 scheme, $\alpha = 12$ is recommended, although other values of α may also be considered.

Fourier analysis of the third-order 1-1-1-1 scheme

In the next place, the third-order 1-1-1-1 scheme is analyzed and the impact of different values of α is discussed. Fig. 14 presents the Fourier analysis results of two different 1-1-1-1 schemes with $\alpha = 1.5$ and 3, where results of the

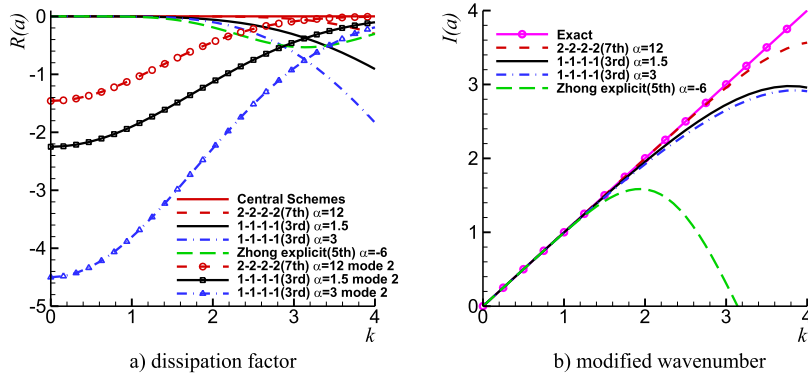


Fig. 14. Fourier analysis results of the 1-1-1-1 scheme (3rd order) with different upwind coefficients.

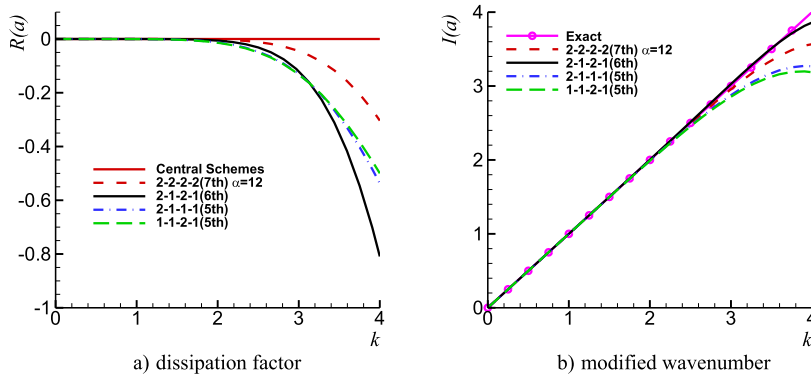


Fig. 15. Comparison of the MLC schemes on the centered and bias stencils.

seventh-order 2-2-2-2 scheme with $\alpha = 12$ and Zhong’s fifth-order explicit scheme with $\alpha = -6$ are also presented for comparison. Same as Fig. 13, dissipation factors of both physical and spurious modes $-R(a_1)$ and $R(a_2)$ are plotted to show dissipation and stiffness of the 1-1-1-1 scheme, and modified wavenumber of spurious mode $-I(a_1)$ is plotted to show resolution. Fig. 14(a) shows that the 1-1-1-1 schemes with both α values have larger dissipation factors than the 2-2-2-2 scheme, as well as errors in modified wavenumber showed in Fig. 14(b). This is reasonable that high-order MLC scheme is more accurate than low-order MLC scheme considering both dissipative and dispersive errors. Furthermore, Fig. 14(b) indicates the third-order 1-1-1-1 scheme has a much better resolution for large k than Zhong’s fifth-order explicit scheme though the former is two orders lower than the latter. This advantage can be explained by the additional degrees of freedom contained on each grid points. In addition, Fig. 14(a) shows that the 1-1-1-1 scheme has smaller dissipation than Zhong’s explicit scheme for a wide range of k as well. Specifically, the 1-1-1-1 scheme with $\alpha = 3$ are less dissipative than Zhong’s fifth-order explicit scheme when $k < 2.8$; and the 1-1-1-1 scheme with $\alpha = 1.5$ are less dissipative than Zhong’s fifth-order explicit scheme when $k < 3.4$, which covers the entire significant range $[0, \pi]$ of conventional finite difference scheme.

Increasing upwind coefficients α introduces more dissipation for both $R(a_1)$ and $R(a_2)$ as Fig. 14(a) shows. Meanwhile, increasing α also decreases the resolving ability slightly as observed in Fig. 14(b). So, larger α makes the 1-1-1-1 scheme less accurate. Similar to the discussion for the 2-2-2-2 scheme, the magnitude of $R(a_2)$ affects the stiffness of the problem, which indicates an increase of α leads to increase of stiffness. On the other hand, α should be large enough to ensure stability. Considering stability, accuracy, and stiffness, the recommended value for α is 1.5 for third-order 1-1-1-1 scheme. Again, other values may also be considered.

Fourier analysis of MLC schemes on bias stencils

MLC schemes with bias grid stencils including the 2-1-2-1, 2-1-1-1 and 1-1-2-1 schemes are also analyzed using Fourier analysis approach. Formulas of these schemes can be found in Appendix A.1. These MLC schemes follow traditional upwind schemes, where the bias stencil introduces enough numerical dissipation to control the aliasing errors and to enhance the numerical stability [1]. On the other hand, the upwind MLC schemes presented in Section 2 follow Zhong’s upwind compact and explicit scheme [1] by using the centered stencil with an adjustable parameter α in the leading dissipative truncation term. Fig. 15 compares the Fourier analysis results of the sixth-order 2-1-2-1 scheme, the fifth-order 2-1-1-1 scheme, and the fifth-order 1-1-2-1 scheme on bias stencils, where the seventh-order 2-2-2-2 scheme on the centered stencil with $\alpha = 12$ is also presented for comparison. Only physical mode a_1 is plotted to compare accuracies. Fig. 15(b) shows that all the schemes have a spectral-like resolution. Specifically, the seventh-order 2-2-2-2 scheme on centered stencil

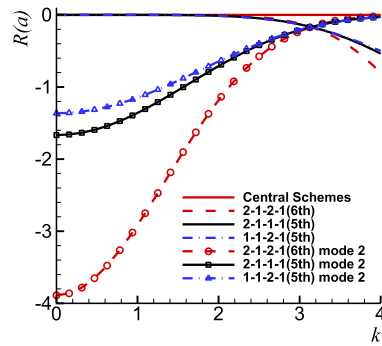


Fig. 16. Dissipation factors of physical and spurious modes of the MLC schemes on bias stencils.

has better resolution than the fifth-order 2-1-1-1 and 1-1-2-1 schemes on bias stencils, but worse than the sixth-order 2-1-2-1 scheme on bias stencil. However, Fig. 15(a) shows the 2-1-2-1 scheme has the largest dissipation among all schemes while the 2-2-2-2 scheme has the smallest dissipation. Overall, the upwind 2-2-2-2 scheme is more favorable, because it has the smallest dissipation and very good spectral resolution, although lower than the resolution of the 2-1-2-1 scheme for large k . This observation is consistent with the conclusion in [1] that upwind scheme on centered grid stencil have smaller dissipation than those on upwind-bias grid stencil. As for the comparison of fifth-order 2-1-1-1 scheme which has bias stencil on the value layer, and fifth-order 1-1-2-1 scheme which has bias stencil on the derivative layer, there is no much difference except the latter is slightly more dispersive and less dissipative. Therefore, using bias stencil on value layer introduces slightly larger dissipation than the bias setting for the derivative layer.

Fig. 16 presents $R(a_1)$ and $R(a_2)$ together for the three MLC schemes on bias stencils to compare the stiffness of these different MLC schemes. The 2-1-2-1 scheme which uses bias stencil on both value and derivative layers have the largest dissipation in $R(a_1)$ and $R(a_2)$; the 2-1-1-1 scheme which uses bias stencil on the value layer has slightly larger dissipation than the 1-2-1-1 scheme which uses bias stencil on the derivative layer. Therefore, using bias stencil introduces larger dissipation in both $R(a_1)$ and $R(a_2)$, and its effect is more obvious when applied to the value layer. In addition, using bias stencil on both the value and derivative layer may introduce too much dissipation in $R(a_2)$. For example, the maximum magnitude of $R(a_2)$ is about 3.9 for 2-1-2-1 scheme. As comparison, the maximum is about 1.5 for the 2-2-2-2 scheme with $\alpha = 12$ in Fig. 13(a), and it is about 2.2 for 1-1-1-1 scheme with $\alpha = 1.5$ in Fig. 14(a). As a result, the 2-1-2-1 scheme requires smaller time step size in temporal discretization. From the analysis on Figs. 15 and 16, it is more appropriate to construct upwind MLC schemes on centered stencils considering stability, dissipation, and stiffness. In fact, the 2-1-1-1 and 1-1-2-1 schemes can be considered as special cases on centered stencils with some large values of α , as mentioned in Section 2.

Fourier analysis of pure upwind MLC schemes

In conventional finite difference methods, stable upwind schemes can be derived on one-sided bias stencils. For example, a second-order upwind scheme

$$u'_i = \frac{1}{2h}(u_{i-2} - 4u_{i-1} + 3u_i) \quad (59)$$

can be derived by using two points on the upwind side. However, the fourth-order 2-0-2-0 scheme constructed on the similar stencil is unstable. Fig. 17 shows the Fourier analysis results of the 2-0-2-0 scheme and other unstable pure upwind MLC schemes, where the results of the seventh-order 2-2-2-2 scheme with $\alpha = 12$ is also presented for comparison. Here, only physical mode a_1 is plotted for the MLC schemes. Fig. 17(a) shows that the MLC schemes on one-sided bias stencils has positive $R(a_1)$'s which indicate instability of these schemes. The numerical instability increases with the rising order of accuracy. Fig. 17(b) shows their modified wavenumber $I(a_1)$'s fall on the other side of the exact solution for large k 's, which is different from the 2-2-2-2 scheme. The spectral resolution of the pure upwind MLC schemes are also not as good as the 2-2-2-2 scheme.

The instability of the pure upwind MLC schemes is unexpected because one-sided stencils usually leads to stable schemes in conventional finite difference methods. However, the MLC scheme introduces additional degrees of freedom which makes numerical stability more complicated. It is discovered through further Fourier analysis that the stability of the pure upwind MLC scheme is affected by the imbalance level of the stencils. Fig. 18(a) shows that the 1-0-1-0, 2-0-1-0, and 1-0-2-0 schemes are stable, which have less imbalance than the 2-0-2-0 scheme or other pure upwind schemes in Fig. 17. However, the $R(a_2)$ of these pure upwind MLC schemes show much larger dissipations for small k 's compared with previous examples (see Figs. 13, 14, and 16), which should result in more restrictive time step sizes. Fig. 18(b) shows that their dispersive error is also larger, and the spectral resolution reduces with the increasing imbalance level. On the other hand, any pure upwind MLC scheme with four- or higher order of accuracy are proven to be unstable through Fourier analysis, as shown in Fig. 17. Therefore, the stability and accuracy of pure MLC scheme are very sensitive to the imbalance level of stencils, and very high-order MLC scheme cannot be derived on one-sided bias stencils.

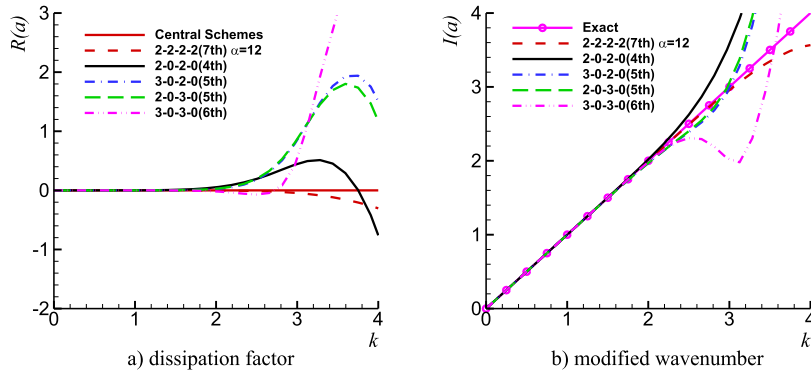


Fig. 17. Fourier analysis results of the unstable MLC schemes on one-sided bias stencils.

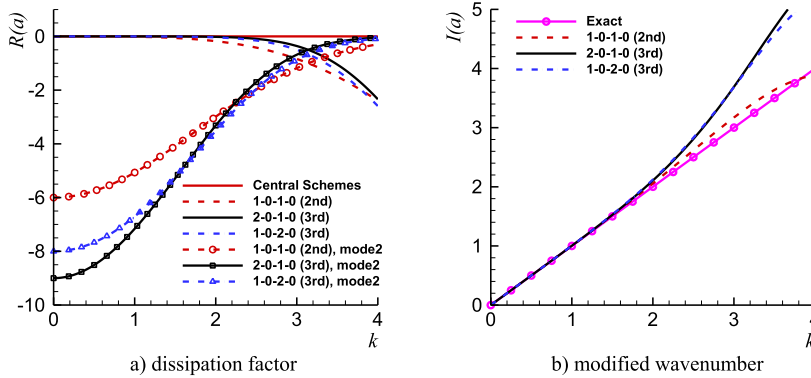


Fig. 18. Fourier analysis results of the stable MLC schemes on one-sided bias stencils.

In summary, the one-dimensional Fourier analysis in this section shows that: 1) the stable MLC scheme can be constructed on centered stencils with upwind coefficients α , or on upwind bias stencils; 2) it has very high resolution, small dissipative and dispersive errors, reasonable stiffness. Comparison of the 1-1-1-1 scheme and Zhong’s fifth-order explicit scheme indicates even lower order MLC scheme can have better resolution and smaller dissipation than conventional higher-order scheme; 3) the value of α has an impact on the stability, accuracy, and stiffness of the MLC scheme. The recommended value of α is 12 for the seventh-order 2-2-2-2 scheme and 1.5 for the third-order 1-1-1-1 scheme; 4) using upwind bias stencils for MLC schemes introduces larger dissipation than using a centered stencil and adjustable parameter α , and pure upwind MLC schemes with four- or higher order of accuracy are unstable.

3.2. Two-dimensional Fourier analysis

The dissipation and dispersive errors of the upwind MLC schemes applied to two-dimensional advection equation (36) are also investigated by the Fourier analysis. For multi-dimensional simulations, the approximation of the cross derivative terms given in Eq. (37) may lead to different stability and dissipative properties of the numerical scheme from the one-dimensional analysis. The discretization is based on Cartesian coordinates in this paper. To be generic, the convection angle θ and Fourier wave angle φ are defined in the Fourier analysis. The governing equations are the same as Eq. (36), where the dimensional wave speed can be written as,

$$\begin{aligned} c_1 &= c \cdot \cos \theta \\ c_2 &= c \cdot \sin \theta \end{aligned} \tag{60}$$

which are functions of convection angle θ and the magnitude of wave speed c . Fourier analysis is carried out by assuming the solution in the following form,

$$\begin{bmatrix} u \\ u_x \\ u_y \end{bmatrix} = \begin{bmatrix} \hat{u} \\ \hat{u}_x \\ \hat{u}_y \end{bmatrix} e^{\hat{a}t + i\hat{k}(x \cos \varphi + y \sin \varphi)} \tag{61}$$

where φ is an arbitrary Fourier wave angle, the definitions of \hat{k} and \hat{a} are the same as one-dimensional analysis. The procedure of the two-dimensional Fourier analysis follows the same methodology as in one-dimensional analysis. Substituting the trial solution above into Eq. (36), a relation between \hat{u} , \hat{u}_x and \hat{u}_y can be obtained as,

$$\hat{u} = -\frac{c}{\hat{a}}(\hat{u}_x \cos \theta + \hat{u}_y \sin \theta) \quad (62)$$

Applying the approximations of second and cross derivatives in Eqs. (17) and (37), a cubic characteristic equation of the non-dimensional dissipation factor a defined in Eq. (50) can be derived,

$$a^3 + Ba^2 + Ca + D = 0 \quad (63)$$

Same as one-dimensional analysis, B , C , and D are complex constants dependent on the choice of the finite difference formulas and wavenumber \hat{k} . Meanwhile, they are also functions of θ and φ in two-dimensional analysis as given below,

$$\begin{aligned} B &= (B_2 + B_3) \sin \theta + (B_1 + C_3) \cos \theta \\ C &= (B_2 B_3 - A_2) \sin^2 \theta + (B_1 C_3 - A_1) \cos^2 \theta + \left(\frac{1}{2} B_1 B_2 - A_3\right) \sin 2\theta \\ D &= [A_2(C_3 - B_1) - B_2 A_3] \sin^2 \theta \cos \theta - A_2 B_3 \sin^3 \theta \\ &\quad + [A_1(B_3 - B_2) - B_1 A_3] \sin \theta \cos^2 \theta - A_1 C_3 \cos^3 \theta \end{aligned} \quad (64)$$

and

$$\begin{aligned} A_1 &= \sum_{l=-L_1}^{L_2} a_l e^{i l \hat{k} \cos \varphi}, & A_2 &= \sum_{l=-L_1}^{L_2} a_l e^{i l \hat{k} \sin \varphi} \\ B_1 &= \sum_{m=-M_1}^{M_2} b_m e^{i m \hat{k} \cos \varphi}, & B_2 &= \sum_{m=-M_1}^{M_2} b_m e^{i m \hat{k} \sin \varphi} \\ A_3 &= \sum_{\substack{l_x=-L_1 \\ l_y=-L_1}}^{L_2} a_{l_x, l_y} e^{i \hat{k}(l_x \cos \varphi + l_y \sin \varphi)} \\ B_3 &= \sum_{\substack{m_x=-M_1 \\ m_y=-M_1}}^{M_2} b_{m_x, m_y} e^{i \hat{k}(m_x \cos \varphi + m_y \sin \varphi)} \\ C_3 &= \sum_{\substack{n_x=-M_1 \\ n_y=-M_1}}^{M_2} c_{n_x, n_y} e^{i \hat{k}(n_x \cos \varphi + n_y \sin \varphi)} \end{aligned} \quad (65)$$

Three roots of Eq. (63) correspond to one physical mode a_1 and two spurious modes a_2, a_3 . The real and imaginary part of a plays the same role as in one-dimensional analysis. The exact solution of a is,

$$a_{exc} = i \hat{k} h \cos(\theta - \varphi) = i k \cos(\theta - \varphi) \quad (66)$$

which is a product of one-dimensional exact solution in Eq. (53) and a cosine function of θ and φ .

In the two-dimensional Fourier analysis as well as two-dimensional numerical simulations presented later, the one-dimensional MLC schemes with recommended α values are used for the approximation of second derivatives, while cross derivatives are discretized by the two-dimensional MLC schemes with one order higher of accuracy than the one-dimensional scheme. Therefore, the overall accuracy depends on one-dimensional MLC schemes. Different θ and φ are considered in the two-dimensional Fourier analysis.

The two-dimensional Fourier analysis is first carried out to the third-order 1-1-1 scheme with $\alpha = 1.5$ as given in Eqs. (16) and (38). Fig. 19(a) presents the dissipation factors for the case of $\theta = 0$, and Fig. 19(b) shows results for the case of $\theta = \pi/4$. For each case of θ , two cases of φ are compared which also have the values of 0 and $\pi/4$. All three modes are presented, where a_1 is the physical mode and a_2, a_3 are two spurious modes. The figure shows a_1 and a_2 behave similarly as those of one-dimensional Fourier analysis, while a_3 is the distinctive mode for two-dimensional Fourier analysis. When both θ and φ are 0, the results are the same with one-dimensional Fourier results in Fig. 14. The value of $R(a_3)$ depends on both θ and φ . When θ is zero, it is always zero which means spurious mode will keep its initial condition during the simulation. When θ is not zero but φ is zero, $R(a_3)$ is a negative constant which means the spurious mode will be evenly decayed for all the wavenumbers. When both θ and φ is not zero, a_3 behaviors similarly to a_2 . Overall, all three modes are stable in two-dimensional Fourier analysis. Similar to one-dimensional analysis, stiffness is dominated by spurious modes.

The modified wavenumber of physical mode $I(a_1)$ for the same 1-1-1 scheme is shown in Fig. 20. It should be mentioned that the spurious modes a_2 and a_3 do not affect accuracy significantly. Even though they affect the stiffness of the

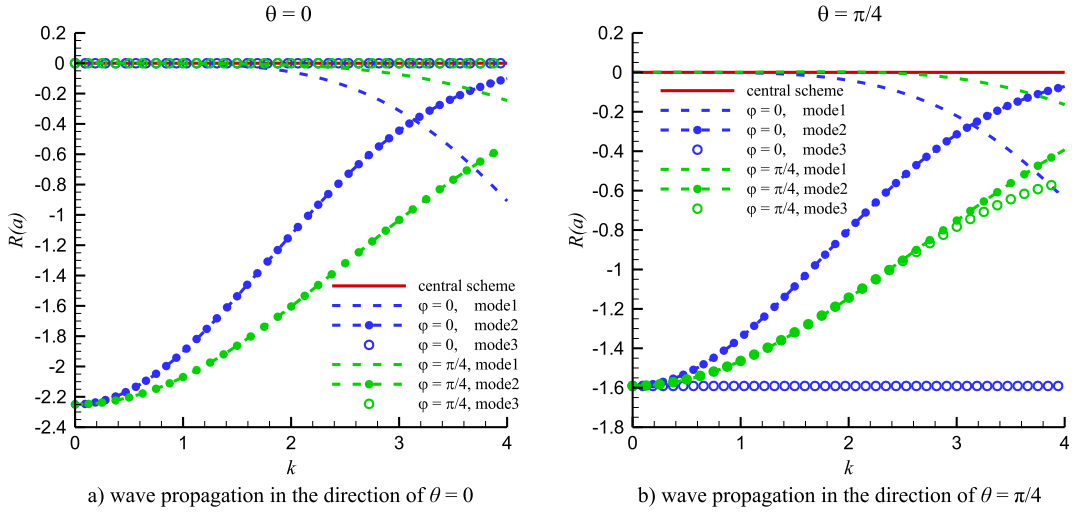


Fig. 19. Dissipation factor $R(a_1)$, $R(a_2)$, $R(a_3)$ of the 1-1-1 scheme (3rd order) for two-dimensional wave propagation.

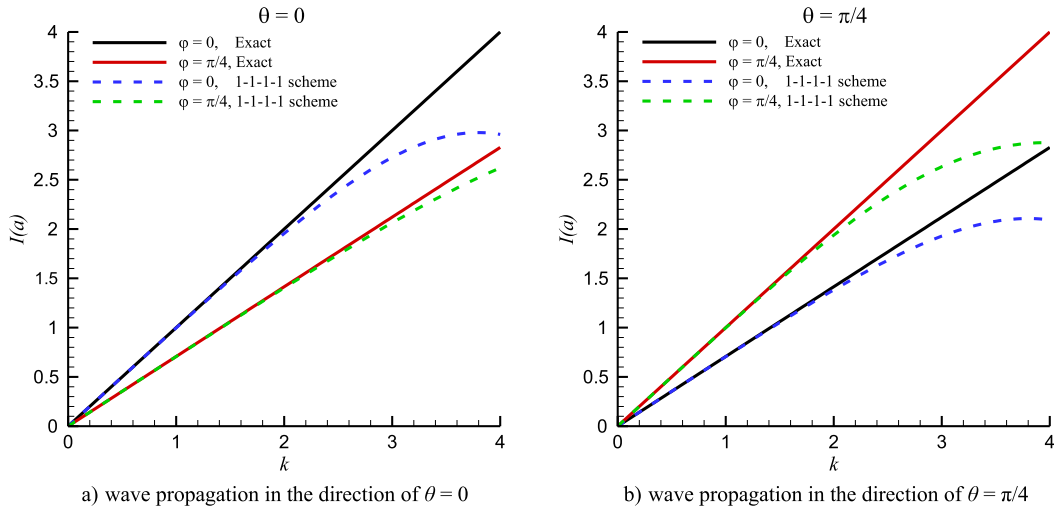


Fig. 20. Modified wavenumber $I(a_1)$ of the 1-1-1 scheme (3rd order) for two-dimensional wave propagation.

problem, the amplitudes of $R(a_2)$, $R(a_3)$ are much larger than those of $I(a_2)$, $I(a_3)$. Therefore, only $I(a_1)$ is plotted in two-dimensional Fourier analysis. In the figures, all the results with different combinations of θ and φ show a good resolution of the scheme for small k . When θ is zero as shown in Fig. 20(a), the scheme has the best resolution. Comparing the results of (a) and (b), we can observe that the accuracy is reduced when $\theta = \pi/4$. In fact, it is true for all non-zero θ , and this property is well known as the anisotropic error of finite difference methods for multi-dimensional simulations. However, Fig. 20 indicates that the difference is relatively small for the MLC scheme. This favorable property is probably because our MLC schemes take information from neighboring points in all different orientations in the approximation of cross derivatives. On the other hand, changing of φ does not have an obvious effect on the spectral resolution.

The two-dimensional Fourier analysis is then carried out to the seventh-order 2-2-2-2 scheme with $\alpha = 12$ as given in Eqs. (19) and (39). Dissipation factors of all three modes are presented in Fig. 21, and modified wavenumber of physical mode a_1 is shown in Fig. 22. Comparing Figs. 19 and 21, we observe that all modes of the 2-2-2-2 scheme are less dissipative than those of 1-1-1-1 scheme. Comparing Figs. 20 and 22, we can see the resolution of the 2-2-2-2 scheme for large k is better than that of the 1-1-1-1 scheme. Both aspects indicate 2-2-2-2 scheme is much more accurate than the 1-1-1-1 scheme in two-dimensional simulations. In addition, similar effects of θ and φ on the resolution as 1-1-1-1 scheme can be observed in the results of the 2-2-2-2 scheme which indicates the anisotropic error is still very small.

In order to further investigate the anisotropy, the phase speed (c_p) of MLC schemes is computed and analyzed, where c_p is defined as,

$$c_p(k, \theta) = \frac{I(a(k, \theta, \varphi))}{k}, \quad \text{and } \varphi = \theta \tag{67}$$

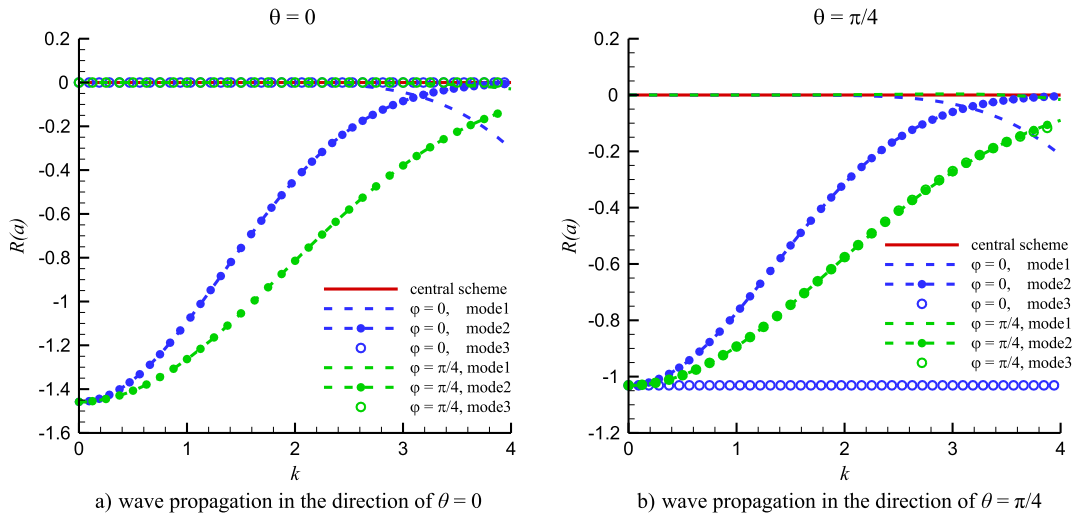


Fig. 21. Dissipation factor $R(a_1)$, $R(a_2)$, $R(a_3)$ of the 2-2-2-2 scheme (7th order) for two-dimensional wave propagation.

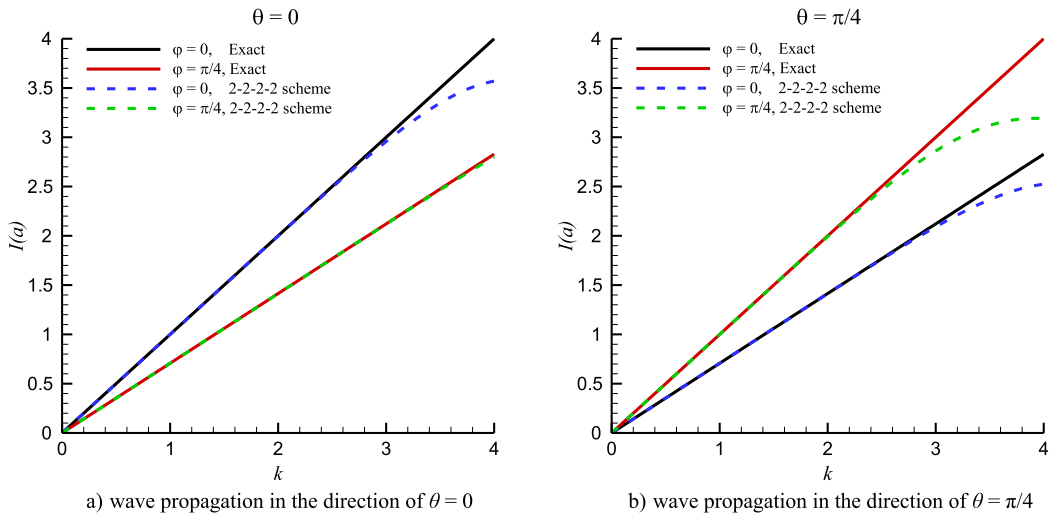


Fig. 22. Modified wavenumber $I(a_1)$ of the 2-2-2-2 scheme (7th order) for two-dimensional wave propagation.

where a is a function of wavenumber k , convection angle θ , and Fourier wave angle φ . The two-dimensional Fourier analysis above has shown that the effect of φ on the spectral resolution is not obvious. Therefore, we can follow Lele’s approach [18] in the anisotropy analysis by assuming θ and φ have the same value. For conventional finite difference methods, c_p can be computed from the modified wavenumber k' in one-dimensional Fourier analysis as,

$$c_p(k, \theta) = \frac{\cos \theta k'(k \cos \theta) + \sin \theta k'(k \sin \theta)}{k} \tag{68}$$

where $k'(x)$ is a function determined by coefficients of a finite difference scheme [18].

Fig. 23 compares the phase speed of various upwind MLC schemes and Zhong’s upwind explicit and compact schemes [1]. The phase speed contours are plotted in the range of $k = [0, \pi]$ and $\theta = [0, 2\pi]$, where each curve represents a fixed value of k . The exact value of c_p is 1 for any k and θ , which corresponds to the outer circle in the plots. Two properties can be shown from the figure; the distorted shape from a perfect circle represents the anisotropic error, and the shrink of the circle represents the dispersive error. Small k values correspond to outer contours, and contours for large k values are in the middle. As k increases from 0 to π , both anisotropic and dispersive errors increase. For a conventional finite difference scheme, the innermost curve drops to the center indicating that $k = \pi$ is the limit of spectral resolution of the scheme. Among Zhong’s explicit scheme (a), (b), (c) and compact scheme (d), the fifth-order compact scheme (d) has the smallest anisotropic error which is consistent with the conclusion of Lele [18]. In the results of MLC schemes (e), (f), (g), both the anisotropic error and dispersive error are much smaller than conventional finite difference schemes for any k and θ .

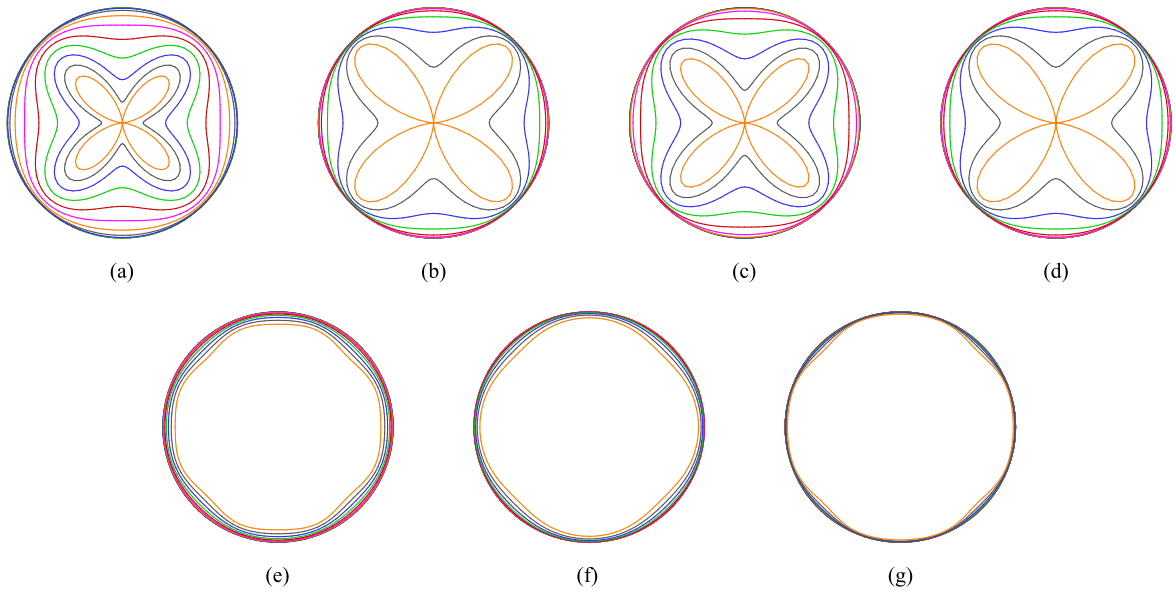


Fig. 23. Polar plot of phase speed anisotropy (contours are plotted at $k/\pi = 1/50, 5/50, \dots, 45/50, 50/50$): (a) Zhong's third-order explicit scheme; (b) Zhong's fifth-order explicit scheme; (c) Zhong's seventh-order explicit scheme; (d) Zhong's fifth-order compact scheme; (e) the third-order 1-1-1 scheme; (f) the fifth-order 2-2-1-1 scheme; (g) the seventh-order 2-2-2-2 scheme.

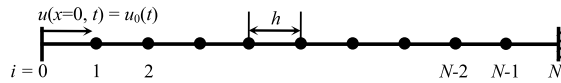


Fig. 24. Schematic for stability analysis on one-dimensional linear advection equation.

In summary, the two-dimensional Fourier analysis in this section shows that the MLC schemes maintain very high resolution, small dissipative and dispersive errors after extended to two-dimensional cases. The anisotropy analysis indicates that anisotropic errors of current MLC schemes are much smaller than conventional finite difference schemes, which is very important in multi-dimensional flow simulations.

3.3. Stability of boundary closure schemes

High-order finite difference methods often require boundary closure schemes at grid points on or near the boundaries of the computational domain. When the inner scheme is coupled with boundary closure schemes, the stability can be affected. It is known that for a p -th-order inner scheme, the stable boundary closure scheme can be one order lower to maintain the p -th-order global accuracy of the inner scheme. For the very high-order upwind MLC scheme, the corresponding boundary closure schemes are also expressed by the formula given in Eq. (12), where bias stencils are used and the adjustable parameter α is set to 0. All the formulations of the boundary closure schemes used in this paper are given in the Appendix A.1.

The matrix method is used in this paper to analyze the stability of boundary closure schemes. For the MLC schemes, the matrix method is implemented on one-dimensional advection equation and its auxiliary equation as shown in Eq. (11). A finite domain is discretized by a uniform grid mesh as shown in Fig. 24, where x has the range of $[0, Nh]$. A total of N grid panels is used, and h is grid spacing. Two non-periodic boundaries are fixed at $x = 0$ and $x = Nh$, i.e., they are numbered as $i = 0$ and $i = N$. Inflow boundary condition is used at $i = 0$, and characteristic boundary condition is used from at $i = N$. For the one-dimensional linear advection, the inflow condition is specified by $u_0(t)$ and characteristic boundary condition is implemented by using one-sided MLC scheme. The upwind MLC schemes on centered stencil are used at interior grid points, and different boundary closure schemes are applied when the stencil of inner scheme goes beyond the left and right boundaries.

In matrix method, Eq. (11) is discretized into a system of ordinary differential equations by using the inner and boundary closure schemes. The resulting equations can be represented in matrix form,

$$\frac{d}{dt} \begin{bmatrix} \mathbf{U} \\ \mathbf{U}' \end{bmatrix} + c \begin{bmatrix} \mathbf{0} & \mathbf{I} \\ \mathbf{A} & \mathbf{B} \end{bmatrix} \cdot \begin{bmatrix} \mathbf{U} \\ \mathbf{U}' \end{bmatrix} = \begin{bmatrix} \mathbf{0} \\ \mathbf{g}(t) \end{bmatrix} \tag{69}$$

Table 1
Selections of inner and boundary closure schemes with 3rd-order expected global accuracy.

| | Case 1 | Case 2 |
|--------------------|--------------------------------------|--------------------------------------|
| $i = 0$ | Inflow boundary condition | Inflow boundary condition |
| $i = 1$ to $N - 1$ | 3rd-order 1-1-1-1 scheme (Eq. (15)) | 3rd-order 1-1-1-1 scheme |
| $i = N$ | 2nd-order 1-0-1-0 scheme (Eq. (111)) | 3rd-order 2-0-1-0 scheme (Eq. (115)) |

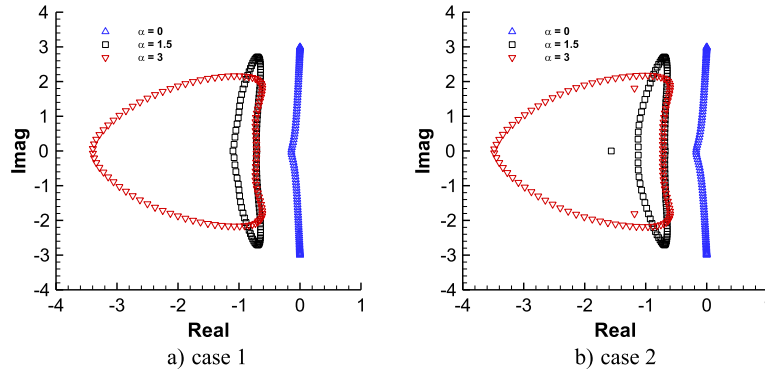


Fig. 25. Eigenvalue spectrum of the 3rd-order 1-1-1-1 scheme coupled with two different boundary closure schemes.

where $\mathbf{U} = (u_1, \dots, u_N)^T$, $\mathbf{U}' = (u'_1, \dots, u'_N)^T$ are the unknowns. The source term $\mathbf{g}(t)$ are a vector with N elements which are dependent on $u(x = 0, t) = u_0(t)$ and $u'(x = 0, t)$ – the inflow boundary condition given at $i = 0$. The derivative boundary condition $u'(x = 0, t)$ is obtained through the advection equation,

$$u'(x = 0, t) = -\frac{1}{c} \frac{d}{dt} u_0(t) \tag{70}$$

Matrices \mathbf{A} and \mathbf{B} consist of the coefficients of both inner and boundary closure schemes. Without losing generality, $c = 1$ is used in the analysis, and the equations can be written in a system of ordinary differential equations,

$$\frac{d}{dt} \bar{\mathbf{U}} = \mathbf{L} \cdot \bar{\mathbf{U}} + \mathbf{G}(t) \tag{71}$$

by introducing the definitions,

$$\bar{\mathbf{U}} = (\mathbf{U}, \mathbf{U}')^T, \quad \mathbf{L} = -\begin{bmatrix} \mathbf{0} & \mathbf{I} \\ \mathbf{A} & \mathbf{B} \end{bmatrix}, \quad \mathbf{G}(t) = \begin{bmatrix} \mathbf{0} \\ \mathbf{g}(t) \end{bmatrix} \tag{72}$$

The stability of Eq. (71) is determined by eigenvalue of matrix \mathbf{L} , which only depends on the particular inner and boundary closure schemes. For asymptotic stability, the real part of all the eigenvalues of \mathbf{L} needs to be non-positive. The boundary source terms $\mathbf{G}(t)$ can be ignored in the stability analysis. In this paper, the eigenvalue of \mathbf{L} is solved numerically, and the eigenvalue spectrum is used to show stability.

First, the stability of boundary closure schemes is performed for the third-order 1-1-1-1 scheme. Table 1 lists two cases with different selections of boundary closure schemes based on the same inner scheme. The 1-1-1-1 scheme uses a three-point stencil, so boundary closure scheme is required only at the right end ($i = N$). Both case 1 and 2 are supposed to have third-order global accuracy.

Fig. 25(a) shows the eigenvalue spectrum of case 1. The upwind coefficient α for the inner scheme can affect the boundary closure schemes. The eigenvalues show that 1-1-1-1 upwind scheme with positive α values is stable. Increasing α causes the spectrum to move towards negative direction, which means the scheme is more stable. The figure also shows that even with central scheme ($\alpha = 0$) on interior points, second-order boundary closure schemes are still stable though the real parts of eigenvalues are very close to 0. The central scheme is usually considered unstable because it contains no numerical dissipation. However, the boundary closure scheme on a bias stencil (1-0-1-0) at the right end might have stabilization effect as upwind schemes. As a result, the central scheme becomes stable. Comparing three spectrums, we can see the recommend α value from Fourier analysis ($\alpha = 1.5$) is still preferred because it has relatively low dissipation.

Fig. 25(b) shows the eigenvalue spectrum of case 2, where third-order boundary closure schemes are coupled with the 1-1-1-1 scheme. It turns out the eigenvalue spectrum is similar to case 1. No positive real part of eigenvalues is observed for all α choices. It can be concluded from Fig. 25 that both second-order (case 1) and third-order (case 2) boundary closure schemes can be coupled with the 1-1-1-1 scheme. The upwind setting in 1-1-1-1 scheme helps to stabilize boundary closure schemes. The value for α is still chosen to be 1.5 to keep enough dissipation and maintain accuracy at the same time.

Table 2
Selections of inner and boundary closure schemes with 7th-order expected global accuracy.

| | Case 3 | Case 4 | Case 5 |
|--------------------|--------------------------------------|--------------------------------------|--------------------------------------|
| $i = 0$ | Inflow boundary condition | Inflow boundary condition | Inflow boundary condition |
| $i = 1$ | 6th-order 1-2-1-2 scheme (Eq. (113)) | 7th-order 1-3-1-2 scheme (Eq. (114)) | 7th-order 1-3-1-2 scheme |
| $i = 2$ to $N - 2$ | 7th-order 2-2-2-2 scheme (Eq. (18)) | 7th-order 2-2-2-2 scheme | 7th-order 2-2-2-2 scheme |
| $i = N - 1$ | 6th-order 2-1-2-1 scheme (Eq. (116)) | 7th-order 3-1-2-1 scheme (Eq. (119)) | 7th-order 3-1-2-1 scheme |
| $i = N$ | 6th-order 3-0-3-0 scheme (Eq. (118)) | 6th-order 3-0-3-0 scheme | 7th-order 4-0-3-0 scheme (Eq. (120)) |

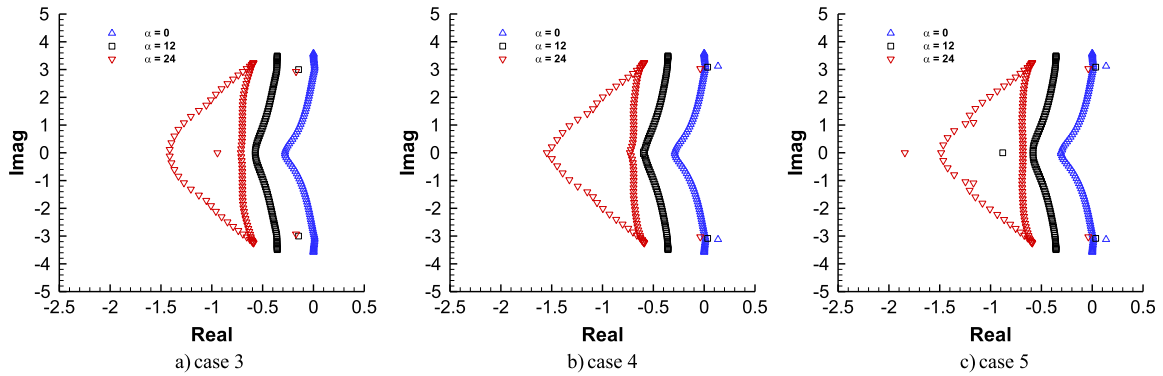


Fig. 26. Eigenvalue spectrum of the 7th-order 2-2-2-2 scheme coupled with three different boundary closure schemes.

Then, the stability of boundary closure schemes is performed for the seventh-order 2-2-2-2 scheme. Table 2 shows three cases with different selections of boundary closure schemes based on the same inner scheme. The 2-2-2-2 scheme uses a five-point stencil and three boundary closure schemes are needed, one for the right boundary ($i = N$) and two for the boundary adjacent points ($i = 1, N - 1$). The MLC scheme with sixth or seventh-order accuracy on bias stencil can be coupled with the 2-2-2-2 scheme to maintain a seventh-order global accuracy.

Fig. 26(a) shows the eigenvalue spectrum of case 3, where sixth-order boundary closure schemes are used. Different from the 1-1-1-1 scheme, the 2-2-2-2 scheme with $\alpha = 0$ is not stable which generates positive real parts in the eigenvalue spectrum. But similarly, increasing α can stabilize the boundary closure schemes. When $\alpha = 12$, which is the recommended value from Fourier analysis above, the sixth-order boundary closure schemes are stable. When α has a value of 24, the dissipation is already very large. So, $\alpha = 12$ is still the recommended choice for the simulation with boundaries.

Seventh-order boundary closure schemes can also be coupled with the seventh-order 2-2-2-2 scheme. However, from the experience of conventional finite difference methods, boundary closure schemes with the same order as the inner scheme may be unstable [1]. Fig. 26(b) shows the eigenvalue spectrum of case 4, where seventh-order schemes are used on the boundary adjacent points. Compared with Fig. 26(a), the continue spectrum distribution does not change obviously, but the positions of discrete eigenvalue points move towards the positive direction in real axis significantly, which indicates the seventh-order boundary closure schemes causes more instability than sixth-order schemes. In Fig. 26(b), the two discrete eigenvalues represented by the black squares have positive real parts, indicating that the 2-2-2-2 scheme with an α value of 12 does not have enough dissipation to stabilize the system. If α is increased to 24, the eigenvalue spectrum becomes non-positive again. However, the numerical dissipation is also increased. Fig. 26(c) shows the eigenvalue spectrum of case 5, where seventh-order boundary closure schemes are also applied on the right boundary. The result of case 5 shows the 2-2-2-2 scheme with α values of 0 and 12 is not stable with seventh-order boundary closure schemes. From case 4 and 5, it can be concluded that the stability decreases when the order of boundary closure scheme is increased, which is consistent with previous experience from Zhong’s finite difference methods [1]. From the analysis above, it is recommended to use sixth-order boundary closure schemes with the seventh-order 2-2-2-2 scheme ($\alpha = 12$), which is case 3 in Table 2.

Through the stability analysis with matrix methods, it is observed that the high-order MLC schemes are less stable with respect to boundary closures than low-order schemes, which is a common feature of high-order finite difference schemes. But due to the compactness of stencil, there are only three boundary closure schemes required even for the seventh-order 2-2-2-2 scheme. As a comparison, Zhong’s fifth-order explicit scheme needs five boundary closure schemes for flow simulations with boundaries. Therefore, the MLC schemes have an advantage in the construction of high-order boundary closure schemes over conventional finite difference schemes.

In Section 3, the new very high-order upwind MLC scheme are analyzed by Fourier analysis and stability analysis with matrix methods. The aliasing in conventional finite difference methods is overcome and spectral-like resolution of the MLC scheme is observed. The dissipative, dispersive, and anisotropic error of the MLC scheme is much smaller than that of conventional finite difference methods. Compared with Zhong’s fifth-order explicit scheme, both the seventh-order 2-2-2-2 scheme and third-order 1-1-1-1 scheme have a much better resolution in the large wavenumber region. Besides, the stencils are more compact because of more degrees of freedom on each grid point. Benefiting from the compactness, high-order

Table 3
Selections of MLC schemes and Zhong's explicit schemes for 1-D linear advection equation.

| MLC scheme | Zhong's explicit scheme [1] |
|---|---|
| 3rd-order 1-1-1-1 scheme ($\alpha = 1.5$) | Zhong's 3rd-order explicit scheme ($\alpha = 0.25$) |
| 5th-order 2-2-1-1 scheme ($\alpha = -1$) | Zhong's 5th-order explicit scheme ($\alpha = -6$) |
| 7th-order 2-2-2-2 scheme ($\alpha = 12$) | Zhong's 7th-order explicit scheme ($\alpha = 36$) |

stable boundary closure schemes are easy to be attained. From both Fourier and stability analysis, the seventh-order 2-2-2-2 scheme with an α value of 12 is supposed to have the best accuracy, and it should be coupled with sixth-order boundary closure schemes for stability, as the case 3 in Table 2.

It should be emphasized that the spectral-like resolution is not simply caused by more total points, including values and derivatives, contained in the stencil. For example, the 3rd-order 1-1-1-1 scheme has a total of 6 points within a double-layer stencil. As a comparison, Zhong's 5th-order explicit scheme has a total of 7 points within a mono-layer stencil. However, the 1-1-1-1 scheme with less total points has much better spectral resolution than Zhong's 5th-order scheme, as shown in Fig. 14. Therefore, the multi-layer framework is the main reason for which the spectral resolution is significantly improved in the MLC schemes. In theory, more layers can be used in the MLC schemes, which means introducing additional equations for higher derivatives. The benefit is that the spectral resolution and the order of accuracy can be further improved with more degrees of freedom. However, the formulation will be too complicated for nonlinear equations such as the Euler and Navier–Stokes equations. The complexity will probably affect the computational efficiency.

4. Numerical results of MLC schemes

This section presents the results of the MLC schemes for the 1-D linear advection equation, the 1-D and 2-D nonlinear Euler equations, and the 2-D compressible Navier–Stokes equations. Numerical solutions are compared with corresponding analytical solutions, and the order of accuracy is evaluated by grid refinement. First, the MLC schemes are applied to the computations of a one-dimensional linear advection. Zhong's fifth-order explicit scheme is also used for comparison. Then, the performances of the MLC schemes on the nonlinear Euler equations are evaluated through the simulation of one-dimensional and two-dimensional entropy waves, one-dimensional acoustic wave, and two-dimensional isentropic vortex. Finally, the MLC schemes are applied to the Navier–Stokes equations, and two-dimensional steady Supersonic Couette flow is simulated. The focus of the numerical tests is on the high-order accuracy and high spectral resolution property when the number of grid points per wavelength is small. Because the MLC scheme is designed for the simulation of smooth flow fields without discontinuity, test cases with shock waves are not considered for the Euler or Navier–Stokes equations in this paper.

4.1. Linear advection equation

In the first place, the new very high-order MLC scheme is tested on the one-dimensional linear advection equation given in Eq. (11), where the wave speed c is set to 1. A sinusoidal wave in x -direction is computed in the simulation, where the exact solution and initial condition ($t = 0$) is given as,

$$u(x, t) = 2 \sin[6\pi(x - t) + 0.5] \quad (73)$$

The computational domain is in an interval of $0 < x < 1$, which includes three wave periods. A uniform mesh with N grid panels is used for spatial discretization. Periodic boundary conditions are set on both ends of the domain. Various upwind MLC schemes are used to solve Eq. (11), along with Zhong's upwind explicit schemes [1] for comparison, as shown in Table 3. All calculations use the fourth-order Runge–Kutta method for time integration. To compare spatial discretization errors and estimate rates of convergence of MLC schemes, the CFL number is set to be a very small value of 0.005 so that the error from the time integration is much smaller than that from spatial discretization. In future simulations, larger CFL numbers can be used which still satisfy the stability condition.

Fig. 27 compares the results of the third and fifth-order schemes mentioned in Table 3 with different grid resolutions ($N = 7, 11, 15$). The goal is to look at how these schemes perform when grid resolution is coarse. In particular, the number of grid points per wavelength is 2.33, 3.67, 5 respectively, when $N = 7, 11, 15$. The simulation is carried out to $t = 1$. As expected, the error increases when gradually decreasing the number of grid points. When $N = 15$ (c), the errors for Zhong's explicit schemes are observable especially with the fifth-order scheme, while the MLC schemes (both 2-2-1-1 and 2-2-2-2) can resolve the wave much better. When $N = 11$ (b), the MLC scheme (both 2-2-1-1 and 2-2-2-2) is still able to resolve the wave very accurately, but both Zhong's fifth and seventh-order explicit schemes show obvious deviation from the exact solution. Finally, when the grid resolution reduces to $N = 7$ (a), the seventh-order 2-2-2-2 scheme still have a very good resolution. The fifth-order 2-2-1-1 scheme is not as accurate as the 2-2-2-2 scheme but also generate reasonable results. In comparison, the results of Zhong's fifth and seventh-order explicit schemes show very large errors, and the solutions do not resemble the exact solution anymore on this very coarse grid. This indicates that the MLC schemes have much better accuracy than conventional finite difference methods on very coarse grids. The MLC schemes maintain excellent resolution

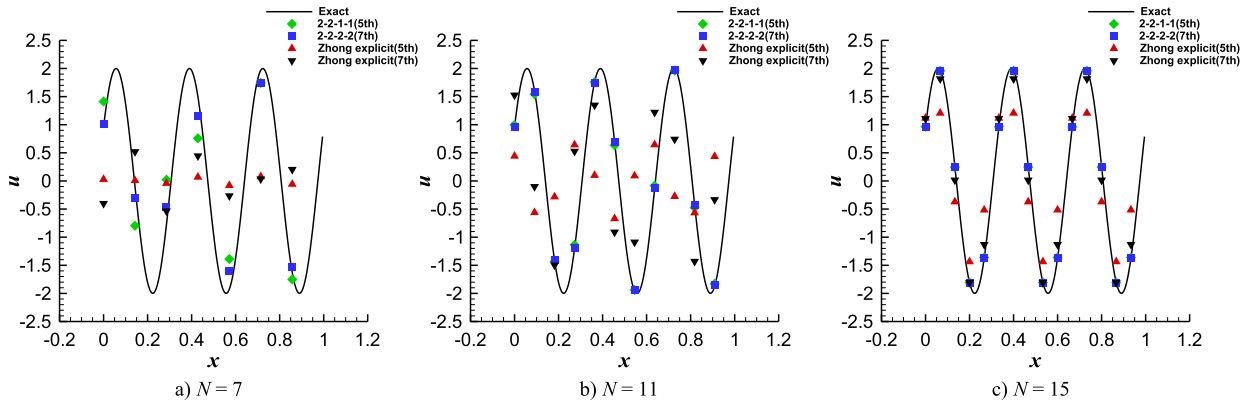


Fig. 27. Comparison of results at $t = 1$ of the MLC schemes and Zhong's explicit schemes with different grid resolutions for the one-dimensional linear advection equation with periodic boundary conditions.

Table 4

Errors and rates of convergence of the 1-1-1-1 scheme (3rd order) and Zhong's explicit scheme (3rd order) for advection equation.

| N | Third-order 1-1-1-1 scheme, $\alpha = 1.5$ | | | | | | Zhong's third-order explicit scheme, $\alpha = 0.25$ | | | | | |
|-----|--|-------|-------------|-------|------------------|-------|--|-------|-------------|-------|------------------|-------|
| | L_1 error | Order | L_2 error | Order | L_∞ error | Order | L_1 error | Order | L_2 error | Order | L_∞ error | Order |
| 5 | 1.40E+00 | – | 1.57E+00 | – | 2.16E+00 | – | 1.45E+00 | – | 1.59E+00 | – | 2.24E+00 | – |
| 10 | 5.62E–01 | 1.31 | 6.42E–01 | 1.29 | 8.69E–01 | 1.31 | 1.15E+00 | 0.34 | 1.26E+00 | 0.34 | 1.77E+00 | 0.34 |
| 20 | 6.76E–02 | 3.06 | 7.56E–02 | 3.09 | 1.07E–01 | 3.02 | 5.52E–01 | 1.06 | 6.12E–01 | 1.04 | 8.62E–01 | 1.04 |
| 40 | 5.65E–03 | 3.58 | 6.28E–03 | 3.59 | 8.88E–03 | 3.59 | 4.54E–02 | 3.60 | 5.05E–02 | 3.60 | 7.15E–02 | 3.59 |
| 80 | 3.93E–04 | 3.85 | 4.37E–04 | 3.85 | 6.17E–04 | 3.85 | 4.06E–03 | 3.48 | 4.51E–03 | 3.49 | 6.37E–03 | 3.49 |
| 160 | 2.54E–05 | 3.95 | 2.82E–05 | 3.95 | 3.98E–05 | 3.95 | 4.36E–04 | 3.22 | 4.84E–04 | 3.22 | 6.85E–04 | 3.22 |

Table 5

Errors and rates of convergence of the 2-2-1-1 scheme (5th order) and Zhong's explicit scheme (5th order) for advection equation.

| N | Fifth-order 2-2-1-1 scheme, $\alpha = -1$ | | | | | | Zhong's fifth-order explicit scheme, $\alpha = -6$ | | | | | |
|-----|---|-------|-------------|-------|------------------|-------|--|-------|-------------|-------|------------------|-------|
| | L_1 error | Order | L_2 error | Order | L_∞ error | Order | L_1 error | Order | L_2 error | Order | L_∞ error | Order |
| 5 | 2.16E+00 | – | 2.36E+00 | – | 3.33E+00 | – | 1.09E+00 | – | 1.23E+00 | – | 1.69E+00 | – |
| 10 | 6.76E–02 | 5.00 | 7.75E–02 | 4.93 | 1.05E–01 | 5.00 | 1.56E+00 | –0.52 | 1.73E+00 | –0.49 | 2.41E+00 | –0.51 |
| 20 | 1.44E–03 | 5.56 | 1.59E–03 | 5.60 | 2.25E–03 | 5.54 | 1.50E–01 | 3.38 | 1.65E–01 | 3.39 | 2.31E–01 | 3.38 |
| 40 | 3.53E–05 | 5.35 | 3.92E–05 | 5.34 | 5.54E–05 | 5.34 | 4.74E–03 | 4.98 | 5.27E–03 | 4.97 | 7.44E–03 | 4.96 |
| 80 | 9.36E–07 | 5.24 | 1.04E–06 | 5.24 | 1.47E–06 | 5.24 | 1.46E–04 | 5.02 | 1.62E–04 | 5.02 | 2.30E–04 | 5.02 |
| 160 | 2.22E–08 | 5.40 | 2.47E–08 | 5.40 | 3.49E–08 | 5.40 | 4.55E–06 | 5.01 | 5.05E–06 | 5.01 | 7.14E–06 | 5.01 |

Table 6

Errors and rates of convergence of the 2-2-2-2 scheme (7th order) and Zhong's explicit scheme (7th order) for advection equation.

| N | Seventh-order 2-2-2-2 scheme, $\alpha = 12$ | | | | | | Zhong's seventh-order explicit scheme, $\alpha = 36$ | | | | | |
|-----|---|-------|-------------|-------|------------------|-------|--|-------|-------------|-------|------------------|-------|
| | L_1 error | Order | L_2 error | Order | L_∞ error | Order | L_1 error | Order | L_2 error | Order | L_∞ error | Order |
| 5 | 1.33E+00 | – | 1.47E+00 | – | 2.05E+00 | – | 8.93E–01 | – | 1.01E+00 | – | 1.38E+00 | – |
| 10 | 1.87E–02 | 6.15 | 2.09E–02 | 6.13 | 2.89E–02 | 6.15 | 1.62E+00 | –0.86 | 1.86E+00 | –0.88 | 2.51E+00 | –0.86 |
| 20 | 1.32E–04 | 7.15 | 1.46E–04 | 7.16 | 2.06E–04 | 7.13 | 2.13E–02 | 6.25 | 2.36E–02 | 6.30 | 3.33E–02 | 6.23 |
| 40 | 8.39E–07 | 7.29 | 9.32E–07 | 7.29 | 1.32E–06 | 7.29 | 1.35E–04 | 7.30 | 1.50E–04 | 7.30 | 2.11E–04 | 7.30 |
| 80 | 4.39E–09 | 7.58 | 4.88E–09 | 7.58 | 6.90E–09 | 7.58 | 9.20E–07 | 7.19 | 1.02E–06 | 7.19 | 1.45E–06 | 7.19 |
| 160 | 1.93E–11 | 7.83 | 2.14E–11 | 7.83 | 3.03E–11 | 7.83 | 6.87E–09 | 7.07 | 7.62E–09 | 7.07 | 1.08E–08 | 7.07 |

for computing components of very small wavelengths, in other words, they can achieve a spectral-like resolution which is the ultimate purpose of the scheme.

In the next place, computational errors of the numerical schemes are calculated, and grid refinement is performed to estimate the rate of convergence. Tables 4 to 6 compare the errors and rates of convergence of different MLC schemes and Zhong's explicit schemes in Table 3. First, the results show that all the schemes can achieve their expected orders of accuracy. All three tables indicate that the MLC schemes have smaller errors and higher rates of convergence than Zhong's explicit schemes with the same designed orders. In Table 4 and Table 6, the estimated orders of the 1-1-1-1 and 2-2-2-2 schemes are almost one order higher than the expected orders (3 and 7) when N is larger than 80, which indicates the MLC scheme is very accurate in the simulation of linear waves. Second, much better accuracies are observed in the MLC schemes on the coarse mesh. For example, Table 4 shows that the error of the 1-1-1-1 scheme is one order smaller in

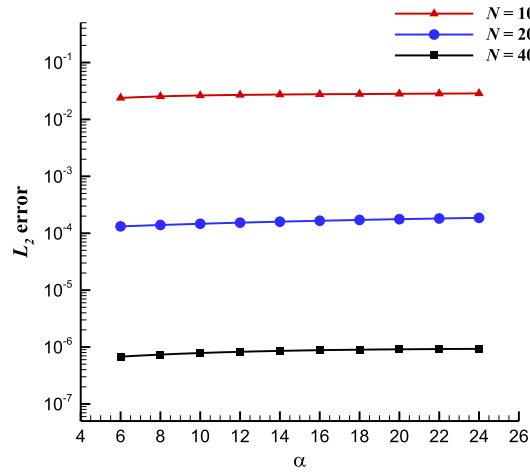


Fig. 28. Evolution of the L_2 error with the α value in the 7th-order 2-2-2 scheme ($t = 1$).

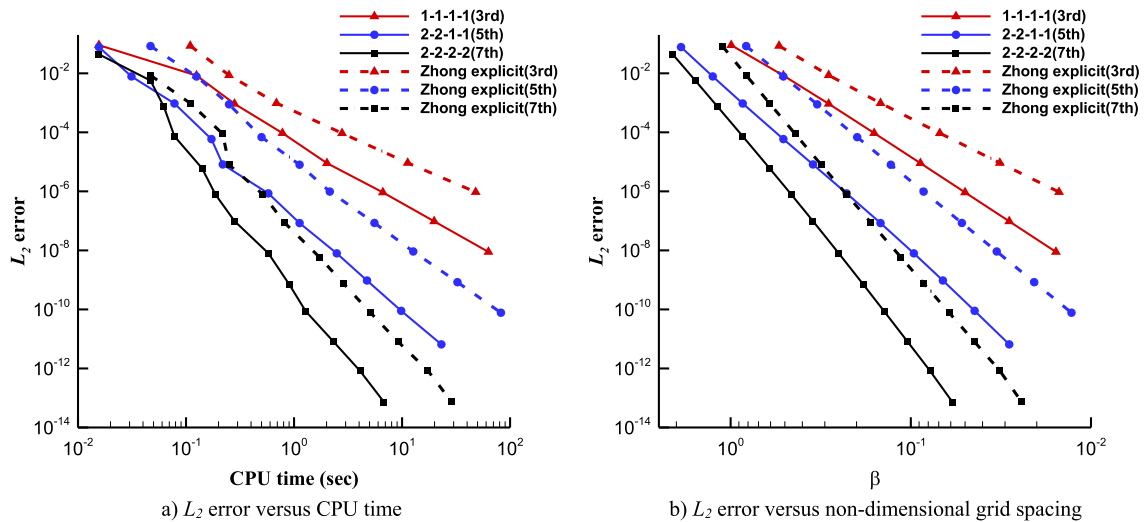


Fig. 29. Computational efficiency of the MLC schemes and Zhong's explicit schemes [1].

magnitude than Zhong's third-order explicit scheme when N equals to 10. The advantage is even more significant for fifth and seventh-order schemes in Table 5 and Table 6, where the MLC schemes are two orders lower in error magnitudes than their counterparts. This quantitative analysis of errors further validates the spectral-like resolution of the MLC scheme.

The parameter α in the upwind MLC scheme is determined based on the Fourier analysis and stability analysis. In Fig. 28, the effect of α values is also investigated in the linear advection simulation with the seventh-order 2-2-2-2 scheme, which has the recommended α value of 12. The L_2 errors with different α values on three sets of grids ($N = 10, 20, 40$) are presented. With the increase of α , the L_2 error grows slightly because of more numerical dissipation; however, the difference is not very significant. Therefore, in the following numerical simulations of this paper, only the results with the recommended α values are presented. It is concluded that the choice of α is not unique as long as it satisfies the stability condition of the interior and boundary closure schemes, as discussed in Section 3; and the recommended α values in Section 2.1 should be appropriate for most practical numerical simulations according to the authors' experience, although it is likely that in some specific cases, the change of α value may significantly affect the results thus it needs to be carefully selected.

There is an issue about computational efficiency of the MLC schemes because one or two auxiliary equations are introduced for one or two-dimensional simulations. However, the original equation becomes exact because the first derivative is available at a grid point, which means it does not need discretization. To show the computational efficiency, Fig. 29 compares the evolutions of L_2 error as a function of CPU time (a) and non-dimensional grid spacing (b) of various MLC schemes and Zhong's explicit schemes. A fixed CFL number of 0.005 is used for all simulations, and errors are measured at $t = 1$. Fig. 29(a) indicates that high-order methods need less CPU time to reach the same accuracy than low-order methods. Between Zhong's explicit scheme and the MLC scheme with the same order of accuracy, the latter converges faster although

Table 7
Required CPU time and grid number (N) at certain magnitudes of L_2 error.

| | CPU time (sec)/ N | | | | | |
|-------------------------------------|---------------------|----------|------------|-----------|------------|-----------|
| | 1.E-02 | 1.E-04 | 1.E-06 | 1.E-08 | 1.E-10 | 1.E-12 |
| 1-1-1-1 scheme (3rd order) | 0.13/37 | 0.78/118 | 6.64/337 | | | |
| Zhong's explicit scheme (3rd order) | 0.25/66 | 2.78/273 | 48.02/1253 | | | |
| 2-2-1-1 scheme (5th order) | 0.03/15 | 0.17/37 | 0.58/83 | 2.48/196 | 9.81/426 | |
| Zhong's explicit scheme (5th order) | 0.13/37 | 0.50/95 | 2.14/222 | 12.69/565 | 82.22/1469 | |
| 2-2-2-2 scheme (7th order) | 0.05/12 | 0.08/22 | 0.19/41 | 0.58/75 | 1.28/134 | 4.08/241 |
| Zhong's explicit scheme (7th order) | 0.05/23 | 0.22/43 | 0.52/83 | 1.72/166 | 5.11/308 | 17.36/588 |

it doubles the degree of freedom and number of equations at each point. When the CFL number is fixed, the time step size is proportional to the grid spacing. Therefore, the total CPU time is dependent on the grid size and the CPU time for a single step. Fig. 29(b) shows the evolution of L_2 error with non-dimensional grid spacing β , which is defined as,

$$\beta = k \cdot h \tag{74}$$

where k is the wavenumber, and h is the dimensional grid spacing. It shows that a high-order scheme allows a larger grid spacing than a low-order scheme to achieve the same accuracy. Furthermore, the MLC schemes have a clear advantage over Zhong's explicit schemes of the same order. As a result, the MLC scheme can achieve the same accuracy with much fewer grid points.

Table 7 shows the required CPU time and grid number (N) for some certain magnitudes of L_2 error. It is clear that the MLC schemes need much fewer grid points than Zhong's explicit schemes to reduce L_2 error to the same magnitude. Benefit from it, the required CPU time is significantly shortened in all MLC schemes compared with their counterparts, and this advantage becomes huge for small error magnitude. For example, to achieve the error magnitude of $1E-10$, the 2-2-1-1 scheme only needs about one-eighth CPU time of Zhong's fifth-order explicit scheme. From Fig. 29 and Table 7, it can be concluded that even the MLC schemes have more equations to solve, they still have very good computational efficiency due to the considerable reduction of grid size. This preceding comparison is for one-dimensional advection equation. In multi-dimensional flow simulations with the Euler or Navier–Stokes equations, the situation becomes more complicated and further investigation is needed.

4.2. Nonlinear Euler equations

Eliminating the viscous term of Navier–Stokes equations in (1) leads to the nonlinear Euler equations for inviscid flows. In the MLC schemes, in addition to the original conservative variable U , the derivatives of U are introduced as additional degrees of freedom. Therefore, it is necessary to introduce auxiliary equations as follows,

$$\frac{\partial U_{x_k}}{\partial t} + \frac{\partial F_{jx_k}}{\partial x_j} = 0 \tag{75}$$

where the subscript x_k represents a directional derivative in the Cartesian coordinates (x_1, x_2, x_3) . The subscript j is a dummy index. For two and three-dimensional simulation, there are two and three auxiliary equations respectively. The Euler equations and the auxiliary equations can be written in vector forms as follows,

$$\frac{\partial}{\partial t} \begin{bmatrix} U \\ U_{x_k} \end{bmatrix} = - \begin{bmatrix} A_j U_{x_j} \\ F_{jx_k x_j} \end{bmatrix} \tag{76}$$

where $A_j = \partial F_j / \partial U$ is the Jacobian matrix and $F_{jx_k} = A_j U_{x_k}$. The first equation is an exact equation, and only the term $F_{jx_k x_j}$ in the auxiliary equations needs an approximation. This term is approximated from F_j and F_{jx_k} , which can be calculated from U and U_{x_k} exactly. Because the operation of Jacobian matrix A_j is expensive, an efficient way to compute F_j and F_{jx_k} is to rewrite F_j as a function of conservative variables U as follows,

$$F_j = \begin{bmatrix} U_{1+j} \\ \frac{U_2 U_{1+j}}{U_1} + p \delta_{1j} \\ \frac{U_3 U_{1+j}}{U_1} + p \delta_{2j} \\ \frac{U_4 U_{1+j}}{U_1} + p \delta_{3j} \\ \frac{U_5 U_{1+j}}{U_1} + p \frac{U_{1+j}}{U_1} \end{bmatrix}, \quad p = (\gamma - 1) \left(U_5 - \frac{\sum_{i=2}^4 U_i^2}{2U_1} \right) \tag{77}$$

where U_i represents the i th component of U . Then, F_{jx_k} can be obtained by taking derivative of Eq. (77) to x_k as follows,

$$F_{jx_k} = \begin{bmatrix} \frac{U_{1+jx_k}}{U_1^2} (U_{2x_k} U_{1+j} + U_2 U_{1+jx_k}) U_1 - U_2 U_{1+j} U_{1x_k} + p_{x_k} \delta_{1j} \\ \frac{U_{1+jx_k}}{U_1^2} (U_{3x_k} U_{1+j} + U_3 U_{1+jx_k}) U_1 - U_3 U_{1+j} U_{1x_k} + p_{x_k} \delta_{2j} \\ \frac{U_{1+jx_k}}{U_1^2} (U_{4x_k} U_{1+j} + U_4 U_{1+jx_k}) U_1 - U_4 U_{1+j} U_{1x_k} + p_{x_k} \delta_{3j} \\ \frac{U_{1+jx_k}}{U_1^2} (U_{5x_k} U_{1+j} + U_5 U_{1+jx_k}) U_1 - U_5 U_{1+j} U_{1x_k} + p_{x_k} \frac{U_{1+j}}{U_1} + p \frac{U_{1+jx_k} U_1 - U_{1+j} U_{1x_k}}{U_1^2} \end{bmatrix}$$

$$p_{x_k} = (\gamma - 1) \left(U_{5x_k} - \frac{\sum_{i=2}^4 U_i U_{ix_k}}{U_1} + \frac{U_{1x_k} \sum_{i=2}^4 U_i^2}{2U_1^2} \right) \tag{78}$$

In this form, F_{jx_k} is only a function of U and U_{x_k} which are the unknowns in Eq. (76).

After F_j and F_{jx_k} are obtained from Eqs. (77) and (78), the new MLC schemes are applied to numerically approximate $F_{jx_k x_j}$ in Eq. (76). Specifically, the one-dimensional MLC scheme in Eq. (12) is used when $j = k$, and the two-dimensional MLC scheme in Eq. (38) is used when $j \neq k$. For the case of $j = k$, the upwind MLC schemes are applied through flux splitting methods. In this paper, a locally global Lax–Friedrichs approach is designed, which is similar to the flux splitting in Zhong’s upwind schemes [1]. The inviscid flux F_j and their derivatives F_{jx_k} , $F_{jx_k x_j}$ are decomposed into positive and negative wave fields as follows,

$$\begin{aligned} F_j &= F_j^+ + F_j^- \\ F_{jx_k} &= F_{jx_k}^+ + F_{jx_k}^- \\ F_{jx_k x_j} &= F_{jx_k x_j}^+ + F_{jx_k x_j}^- \end{aligned} \tag{79}$$

The positive part $F_{jx_k x_j}^+$ and negative part $F_{jx_k x_j}^-$ are approximated by the upwind and downwind MLC schemes respectively, which have the same formula given in Eq. (12), but the opposite sign in α . It is required that the flux F_j^+ and F_j^- contains only positive and negative eigenvalues in their Jacobian matrices respectively. A straightforward approach to construct F_j^+ and F_j^- and their derivatives are,

$$F_j^+ = \frac{1}{2}(F_j + \Lambda U), \quad F_j^- = \frac{1}{2}(F_j - \Lambda U) \tag{80}$$

$$F_{jx_k}^+ = \frac{1}{2}(F_{jx_k} + \Lambda U_{x_k}), \quad F_{jx_k}^- = \frac{1}{2}(F_{jx_k} - \Lambda U_{x_k}) \tag{81}$$

where, Λ is a positive parameter large enough to make F_j^+ and F_j^- to contain only positive and negative eigenvalues. In Zhong’s upwind schemes, Λ is a local parameter, which introduces small dissipation. However, local Λ causes difficulty for the new MLC schemes because Λ needs to be constant for the splitting of F_{jx_k} in Eq. (81). On the other hand, using a constant Λ in the entire domain will introduce large dissipation especially for low order methods such as the third-order 1-1-1 scheme. Therefore, in our locally global Lax–Friedrichs approach, a constant Λ within each stencil is used, which has the form,

$$\Lambda = \max(\lambda_i) \tag{82}$$

and λ_i is a positive parameter chosen to be larger than the local maximum eigenvalues of the Jacobian A_j on point i . When the Euler equations are discretized at a base point i_0 , Λ is set to be the largest λ_i in the grid stencil. Taking one-dimensional 2-2-2 scheme as an example, at the point i_0 , the largest λ_i of the five supporting points ($i_0 - 2 < i < i_0 + 2$) in the stencil is chosen to be Λ . The procedure is repeated for every base point. Compared with using a constant Λ in the entire domain, the locally global Lax–Friedrichs approach has the benefit of maintaining low dissipation. Two-dimensional Fourier analysis in Section 3.2 shows that only the flux splitting for second derivatives ($j = k$) are important to numerical stability. For cross derivatives ($j \neq k$), the central schemes are applied to $F_{jx_k x_j}$ directly for better computational efficiency. After the MLC approximations, Eq. (76) becomes a system of ordinary differential equations, which can be solved by the Runge–Kutta methods.

The discretization described above is performed with respect to the Cartesian coordinates (x_1, x_2, x_3) , and this is straightforward for rectangular physical domains. In general case, the physical domain can have different shapes where curvilinear meshes are required. Therefore, a coordinate transformation between physical and computational domain (ξ_1, ξ_2, ξ_3) will be applied to the governing equations. The discretization with MLC schemes can be applied in the computational domain, which is very similar to the description above. The details of the transformation are not included in this paper for the sake of length.

The boundary conditions of both U and U_{x_k} are needed when the MLC schemes are applied to the Euler equations (76) in a flow simulation with physical boundaries. Most approaches from other finite difference methods still apply to the

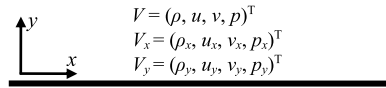


Fig. 30. Schematic of boundary conditions for the MLC schemes on a physical boundary.

boundary conditions of U . However, the boundary conditions of U_{x_k} need to be dealt with in different manners. It should be noted that the boundary condition itself is a big subject, and the optimal boundary conditions for the MLC schemes still need further investigation. In this paper, only one practicable way from many approaches is briefly described. For simplicity, illustration is given for two-dimensional simulations.

It is usually easier to derive boundary conditions on the primitive variables $V = (\rho, u, v, p)^T$ instead of U . Fig. 30 shows a physical boundary along the x -direction, where the boundary value V , the tangential derivative V_x , and the normal derivative V_y need to be determined. Like the analysis for one-dimensional advection in Section 3.3, the derivative boundary conditions can be obtained through governing equations. The Euler equations in two-dimensional case can be written in the primitive form,

$$(A_2 T)V_y = -(A_1 T)V_x - TV_t \tag{83}$$

where the A_1 and A_2 are the Jacobians, and T is defined as $\partial U/\partial V$. The matrices A_1 , A_2 , and T are only functions of V . If the values of V , V_x , and V_t are available on the boundaries, then V_y can be obtained by solving Eq. (83). Therefore, the core problem in boundary conditions becomes determining V , V_x , and V_t on the boundaries. This idea can be applied to different types of boundaries. Some examples are given below.

For a supersonic inflow boundary, V is specified and imposed. Therefore, V_t and V_x can also be obtained by taking a derivative to t and x . For the subsonic inflow, only a part of the flow quantities is specified. Other quantities can be determined by solving characteristic relations, which is termed the characteristic boundary conditions [75]. The characteristic relation also leads to the equation for V_t . The tangential derivatives V_x can be approximated locally from V along the boundary using high-order finite difference methods like Zhong’s compact schemes [1]. Alternatively, we can also derive auxiliary equations for V_x from characteristic relations using the additional degrees of freedom of MLC schemes. For a supersonic outflow boundary, no flow quantities are specified. The boundary conditions are only dependent on information from interior points. They can be obtained by solving Eq. (76) using one-sided MLC schemes, or simply extrapolated from interior values. For a subsonic outflow boundary, p is usually specified. Other quantities are determined by solving characteristic relations. The solution procedure is similar to the case in the subsonic inflow. For a solid wall, the non-penetration condition is applied, in other words, (v, v_x, v_t) is 0. Usually, u and p can be determined from interior points by imposing $u_y = 0$ and $p_y = c$, which is a constant determined by the boundary curvature. Characteristic relations can be used to determine other unspecified quantities in V and V_t . The tangential derivatives V_x can be approximated from V by high-order finite difference methods. For all these examples, the normal derivatives V_y can be obtained through Eq. (83). It is straightforward to convert (V, V_x, V_y) to (U, U_x, U_y) , and the details are not discussed here.

In the following part of this section, the two-dimensional Euler equations in the Cartesian coordinates are solved by the MLC schemes. A rectangular domain is used for simulations and periodic boundary conditions are set for all test cases. Because there is no physical boundary in the domain, uniform grid points are used, and no boundary closure schemes are required. The discretization is performed in physical domain directly with the MLC schemes.

One-dimensional entropy wave

The first test case for the Euler equations is the one-dimensional entropy wave in the x -direction. The same test case is used by Qiu and Shu [60]. The exact solution and initial condition ($t = 0$) is given as follows,

$$\begin{aligned} \rho(x, t) &= 1 + 0.2 \sin(\pi(x - t)) \\ u(x, t) &= 1 \\ p(x, t) &= 1 \end{aligned} \tag{84}$$

where the perturbation only exists in density and temperature. The problem corresponds to a passive convection of a fixed density pattern from the initial condition.

The computational domain is in an interval of $0 < x < 2$, which includes one wave period. A uniform mesh with N grid panels is used to discretize the interval, and periodic boundary conditions are applied on both ends. Both the central and upwind MLC schemes on three different centered stencils (1-1-1-1, 2-2-1-1 and 2-2-2-2) are used for spatial discretization. Same as the calculation of linear advection equation, the fourth-order Runge–Kutta method is applied. The CFL number is a small value of 0.1 to ensure stability and maintain small error from time integration.

The errors of ρ between the numerical and exact solution after simulating for one period ($t = 2.0$) are calculated. The rate of convergence is estimated based on grid refinements. Table 8 shows the results of the third-order 1-1-1-1 schemes, while Table 9 and Table 10 show the fifth-order 2-2-1-1 schemes and the seventh-order 2-2-2-2 schemes respectively. Results of the central scheme ($\alpha = 0$) and upwind scheme ($\alpha \neq 0$) on the same stencil are compared. The first observation

Table 8Errors and rates of convergence based on ρ of the 3/4th-order 1-1-1-1 scheme for the one-dimensional entropy wave.

| N | 1-1-1-1 scheme, $\alpha = 0$ | | | | 1-1-1-1 scheme, $\alpha = 1.5$ | | | |
|----|------------------------------|-------|------------------|-------|--------------------------------|-------|------------------|-------|
| | L_1 error | Order | L_∞ error | Order | L_1 error | Order | L_∞ error | Order |
| 5 | 2.23E-03 | – | 3.16E-03 | – | 1.03E-02 | – | 1.53E-02 | – |
| 10 | 1.27E-04 | 4.14 | 1.87E-04 | 4.08 | 6.81E-04 | 3.92 | 1.01E-03 | 3.92 |
| 20 | 7.42E-06 | 4.10 | 1.14E-05 | 4.03 | 4.40E-05 | 3.95 | 6.66E-05 | 3.92 |
| 40 | 4.57E-07 | 4.02 | 7.10E-07 | 4.01 | 2.74E-06 | 4.01 | 4.23E-06 | 3.98 |
| 80 | 2.84E-08 | 4.01 | 4.43E-08 | 4.00 | 1.70E-07 | 4.01 | 2.66E-07 | 3.99 |

Table 9Errors and rates of convergence based on ρ of the 5/6th-order 2-2-1-1 scheme for the one-dimensional entropy wave.

| N | 2-2-1-1 scheme, $\alpha = 0$ | | | | 2-2-1-1 scheme, $\alpha = -1$ | | | |
|----|------------------------------|-------|------------------|-------|-------------------------------|-------|------------------|-------|
| | L_1 error | Order | L_∞ error | Order | L_1 error | Order | L_∞ error | Order |
| 5 | 2.07E-04 | – | 2.93E-04 | – | 3.78E-04 | – | 5.77E-04 | – |
| 10 | 2.98E-06 | 6.12 | 4.38E-06 | 6.06 | 9.90E-06 | 5.26 | 1.54E-05 | 5.23 |
| 20 | 4.53E-08 | 6.04 | 6.90E-08 | 5.99 | 2.44E-07 | 5.34 | 3.83E-07 | 5.33 |
| 40 | 7.05E-10 | 6.01 | 1.09E-09 | 5.99 | 4.96E-09 | 5.62 | 7.73E-09 | 5.63 |
| 80 | 1.10E-11 | 6.01 | 1.87E-11 | 5.86 | 8.61E-11 | 5.85 | 1.35E-10 | 5.84 |

Table 10Errors and rates of convergence based on ρ of the 7/8th-order 2-2-2-2 scheme for the one-dimensional entropy wave.

| N | 2-2-2-2 scheme, $\alpha = 0$ | | | | 2-2-2-2 scheme, $\alpha = 12$ | | | |
|----|------------------------------|-------|------------------|-------|-------------------------------|-------|------------------|-------|
| | L_1 error | Order | L_∞ error | Order | L_1 error | Order | L_∞ error | Order |
| 5 | 1.24E-05 | – | 1.75E-05 | – | 6.72E-05 | – | 1.04E-04 | – |
| 10 | 4.95E-08 | 7.97 | 7.29E-08 | 7.91 | 3.83E-07 | 7.45 | 5.78E-07 | 7.49 |
| 20 | 1.89E-10 | 8.04 | 2.90E-10 | 7.97 | 1.66E-09 | 7.86 | 2.56E-09 | 7.82 |
| 40 | 1.28E-12 | 7.21 | 2.57E-12 | 6.82 | 7.07E-12 | 7.87 | 1.10E-11 | 7.86 |
| 80 | 2.81E-12 | –1.14 | 3.57E-12 | –0.48 | 6.78E-14 | 6.70 | 1.45E-13 | 6.24 |

from these tables is that the error is very small. In the 1-1-1-1 scheme, the magnitude of error is about 10^{-7} when $N = 80$, which is about the machine epsilon in single precision. For the 2-2-1-1 and 2-2-2-2 schemes, the error is even much smaller. The second observation is that all central schemes ($\alpha = 0$) achieve the expected orders, which is 4, 6, and 8 for the 1-1-1-1, 2-2-1-1, and 2-2-2-2 schemes respectively. The only exception is observed in Table 10 when the error is about 10^{-12} , where the accumulated roundoff error may affect the results. The expected order of the upwind schemes ($\alpha \neq 0$) is one order lower than the corresponding central schemes. However, these tables show that all upwind schemes achieve or even surpass their expected orders. The error of upwind schemes is slightly larger than that of central schemes on the same stencil. This is expected because more dissipation is introduced in the upwind scheme which lowers accuracy. Despite that the central scheme does not have numerical dissipation, the simulation is stable because of the stabilization effect of the fourth-order Runge–Kutta method for time integration.

Two-dimensional entropy wave

The second test for the Euler equations is the two-dimensional entropy wave in (x, y) plane. The exact solution and initial condition ($t = 0$) are given as follows,

$$\begin{aligned}
 \rho(x, y, t) &= 1 + 0.2 \sin(\pi(x + y - (u + v)t)) \\
 u(x, y, t) &= 0.7 \\
 v(x, y, t) &= 0.3 \\
 p(x, y, t) &= 1
 \end{aligned} \tag{85}$$

To be general, there is an angle between the wave vector and convection direction. The wave vector has an angle of $\pi/4$ from the x -axis, and the convection direction is aligned with mean flow velocity. The exact solution of two-dimensional entropy wave is a passive convection. For each location, only density and temperature change during the convection, while the density and temperature patterns from the initial condition are maintained.

The computational domain is a square field within the range of $0 < x < 2$ and $0 < y < 2$, which includes one wavelength in both x - and y -direction. A uniform mesh with N grid panels in both dimensions is used, and periodic boundary conditions on all boundaries are applied. Both the central and upwind schemes on three different centered stencils (1-1-1-1, 2-2-1-1 and 2-2-2-2) are used for spatial discretization. Meanwhile, a fourth-order Runge–Kutta method is applied, and the CFL number is a small value of 0.1 to ensure stability and maintain small error from time integration.

Table 11

Errors and rates of convergence based on ρ of the 3/4th-order 1-1-1-1 scheme for the two-dimensional entropy wave.

| N | 1-1-1-1 scheme, $\alpha = 0$ | | | | 1-1-1-1 scheme, $\alpha = 1.5$ | | | |
|---------|------------------------------|-------|------------------|-------|--------------------------------|-------|------------------|-------|
| | L_1 error | Order | L_∞ error | Order | L_1 error | Order | L_∞ error | Order |
| 5 × 5 | 1.78E-02 | – | 1.78E-02 | – | 1.41E-02 | – | 1.41E-02 | – |
| 10 × 10 | 1.31E-03 | 3.77 | 1.31E-03 | 3.77 | 7.66E-04 | 4.20 | 7.66E-04 | 4.20 |
| 20 × 20 | 8.36E-05 | 3.97 | 8.36E-05 | 3.97 | 4.47E-05 | 4.10 | 4.47E-05 | 4.10 |
| 40 × 40 | 5.27E-06 | 3.99 | 5.27E-06 | 3.99 | 2.74E-06 | 4.03 | 2.74E-06 | 4.03 |
| 80 × 80 | 3.29E-07 | 4.00 | 3.29E-07 | 4.00 | 1.70E-07 | 4.01 | 1.70E-07 | 4.01 |

Table 12

Errors and rates of convergence based on ρ of the 3/4th-order 2-2-1-1 scheme for the two-dimensional entropy wave.

| N | 2-2-1-1 scheme, $\alpha = 0$ | | | | 2-2-1-1 scheme, $\alpha = -1$ | | | |
|---------|------------------------------|-------|------------------|-------|-------------------------------|-------|------------------|-------|
| | L_1 error | Order | L_∞ error | Order | L_1 error | Order | L_∞ error | Order |
| 5 × 5 | 5.09E-03 | – | 5.09E-03 | – | 4.73E-03 | – | 4.73E-03 | – |
| 10 × 10 | 7.98E-05 | 6.00 | 7.98E-05 | 6.00 | 7.55E-05 | 5.97 | 7.55E-05 | 5.97 |
| 20 × 20 | 1.23E-06 | 6.02 | 1.23E-06 | 6.02 | 1.08E-06 | 6.13 | 1.08E-06 | 6.13 |
| 40 × 40 | 1.91E-08 | 6.00 | 1.91E-08 | 6.00 | 1.27E-08 | 6.41 | 1.27E-08 | 6.41 |
| 80 × 80 | 2.97E-10 | 6.01 | 2.97E-10 | 6.01 | 1.37E-10 | 6.53 | 1.37E-10 | 6.53 |

Table 13

Errors and rates of convergence based on ρ of the 3/4th-order 2-2-2-2 scheme for the two-dimensional entropy wave.

| N | 2-2-2-2 scheme, $\alpha = 0$ | | | | 2-2-2-2 scheme, $\alpha = 12$ | | | |
|---------|------------------------------|-------|------------------|-------|-------------------------------|-------|------------------|-------|
| | L_1 error | Order | L_∞ error | Order | L_1 error | Order | L_∞ error | Order |
| 5 × 5 | 1.14E-03 | – | 1.14E-03 | – | 8.13E-04 | – | 8.13E-04 | – |
| 10 × 10 | 5.30E-06 | 7.74 | 5.30E-06 | 7.74 | 2.06E-06 | 8.63 | 2.06E-06 | 8.63 |
| 20 × 20 | 2.09E-08 | 7.99 | 2.09E-08 | 7.99 | 4.76E-09 | 8.76 | 4.76E-09 | 8.76 |
| 40 × 40 | 8.74E-11 | 7.90 | 8.74E-11 | 7.90 | 1.60E-11 | 8.21 | 1.60E-11 | 8.21 |
| 80 × 80 | 2.32E-12 | 5.23 | 2.32E-12 | 5.24 | 4.33E-13 | 5.21 | 4.33E-13 | 5.21 |

Similar to the procedures of the one-dimensional entropy wave, the errors between the numerical and exact solution of ρ at $t = 2$ for various MLC schemes are given in Tables 11 to 13. First, all three tables show that the errors are less than machine epsilon in single precision when grid resolution is fine enough. Compared with one-dimensional results in Tables 8 to 10, the errors of two-dimensional simulations are larger which is caused by the anisotropic errors of numerical schemes. Second, the grid refinement results show that all the central schemes achieve the expected orders, while all the upwind schemes surpass the expected order. Comparing the upwind and central schemes, we observe that the upwind schemes also have smaller errors on the same stencils. Specifically, Table 13 indicates that the 2-2-2-2 upwind scheme is almost one order higher in accuracy than the central scheme, and it almost surpasses the expected order by two.

The results of one-dimensional and two-dimensional entropy wave show that the current new MLC schemes can maintain very small error in the calculation of nonlinear Euler equations, and the expected order of accuracy can be reached or surpassed in the simulation. Particularly, the upwind version of the MLC schemes is preferable in the multi-dimensional simulations.

One-dimensional acoustic wave

In computational aeroacoustics, one of the main challenges is the accurate prediction of the unsteady sound wave in long-distance propagation. Small dissipation and dispersion are required at the same time to ensure the high fidelity of sound wave in the simulation. In this section, a one-dimensional acoustic wave propagation in the x -direction is simulated as a test case for computational aeroacoustics. The propagation medium of the acoustic wave is air in standard atmosphere pressure and room temperature. A cosine wave is superimposed to the static air flow field as the initial perturbation. The initial conditions are given as follows,

$$\begin{aligned}
 u &= u_\infty + \delta\rho, \quad \delta u = \varepsilon a_\infty \cos(\omega x), \quad u_\infty = 0 \text{ [m/s]} \\
 \rho &= \rho_\infty + \delta\rho, \quad \delta\rho = \varepsilon\rho_\infty \cos(2\omega x), \quad \rho_\infty = 1.1771 \text{ [kg/m}^3\text{]} \\
 \frac{p}{p_\infty} &= \left(\frac{\rho}{\rho_\infty}\right)^\gamma, \quad p_\infty = 101325 \text{ [Pa]} \\
 a_\infty &= \sqrt{\gamma \frac{p_\infty}{\rho_\infty}}, \\
 \gamma &= 1.4, \quad \omega = 6\pi, \quad \varepsilon = 10^{-5}
 \end{aligned}
 \tag{86}$$

Table 14

Errors and rates of convergence based on ρ of the 1-1-1-1 scheme (3rd order) and the 2-2-2-2 scheme (7th order) for the acoustic wave.

| N | 1-1-1-1 scheme, $\alpha = 1.5$ | | | | 2-2-2-2 scheme, $\alpha = 12$ | | | |
|-----|--------------------------------|-------|------------------|-------|-------------------------------|-------|------------------|-------|
| | L_1 error | Order | L_∞ error | Order | L_1 error | Order | L_∞ error | Order |
| 5 | 0.00E+00 | – | 0.00E+00 | – | 0.00E+00 | – | 0.00E+00 | – |
| 10 | 3.47E–07 | – | 6.24E–07 | – | 4.20E–06 | – | 5.95E–06 | – |
| 20 | 4.14E–06 | –3.58 | 6.10E–06 | –3.29 | 4.11E–08 | 6.68 | 6.35E–08 | 6.55 |
| 40 | 6.38E–07 | 2.70 | 9.81E–07 | 2.64 | 3.11E–10 | 7.04 | 4.93E–10 | 7.01 |
| 80 | 4.52E–08 | 3.82 | 7.18E–08 | 3.77 | 3.25E–12 | 6.58 | 5.14E–12 | 6.58 |
| 160 | 2.80E–09 | 4.01 | 4.47E–09 | 4.00 | 4.76E–13 | 2.77 | 6.49E–13 | 2.99 |

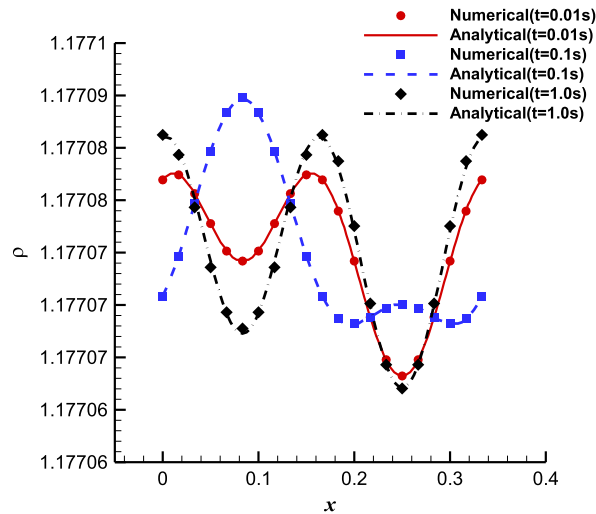


Fig. 31. Density distribution at different simulation time for the 2-2-2-2 scheme (7th order) with $N = 20$.

where ε is the magnitude of initial perturbation, and ω is the wavenumber of perturbations in velocity. The wavenumber of density perturbation is 2ω , and the perturbation in pressure is determined by isentropic relation. The acoustic wave described above is approximately linear because ε is small. Therefore, an analytical solution for comparison can be derived from acoustic wave equation in the following form,

$$\begin{aligned}
 \rho(x, t) &= \rho_\infty + \frac{\varepsilon \rho_\infty}{2} [\cos(2\omega(x - a_\infty t)) + \cos(\omega(x - a_\infty t)) + \cos(2\omega(x + a_\infty t)) - \cos(\omega(x + a_\infty t))] \\
 u(x, t) &= \frac{\varepsilon a_\infty}{2} [\cos(2\omega(x - a_\infty t)) + \cos(\omega(x - a_\infty t)) - \cos(2\omega(x + a_\infty t)) + \cos(\omega(x + a_\infty t))] \\
 p(x, t) &= p_\infty + \frac{\gamma \varepsilon p_\infty}{2} [\cos(2\omega(x - a_\infty t)) + \cos(\omega(x - a_\infty t)) + \cos(2\omega(x + a_\infty t)) - \cos(\omega(x + a_\infty t))] \quad (87)
 \end{aligned}$$

The computational domain is in an interval of $0 < x < 1/3$, which includes one period in the wavelength of initial velocity perturbation. A uniform mesh with N grid panels is used, and periodic boundary conditions on both sides are applied. The third-order 1-1-1-1 MLC scheme ($\alpha = 1.5$) and the seventh-order 2-2-2-2 MLC scheme ($\alpha = 12$) are used for spatial discretization. Meanwhile, a fourth-order Runge–Kutta method is applied to time integration, and the CFL number is a small value of 0.1 to reduce temporal errors.

In the first place, the solution of ρ after computing for one period ($t = 0.01$ s) is used to estimate the rate of convergence of the MLC schemes. The analytical solution in Eq. (87) is not suitable for this estimation, because it is derived from the acoustic wave equations which have embedded error from linearization. As a result, three sets of numerical results with grid refinement are used to estimate the rate of convergence. Table 14 shows the errors and rates of convergence of both the third-order 1-1-1-1 scheme and the seventh-order 2-2-2-2 scheme. Grid refinement results show that both schemes can achieve the expected order, which is 3 and 7 for the 1-1-1-1 and 2-2-2-2 schemes respectively. The exception appears only when the grid is too coarse, or error is already very small. Specifically, the 1-1-1-1 scheme with upwinding surpasses the expected order when $N > 80$.

To evaluate the accuracy of the MLC schemes on capturing long-time solution of the unsteady acoustic wave, the simulation is carried out to 100 times of period ($t = 1.0$ s). Fig. 31 shows the density distributions at three different simulation time when $N = 20$. It shows that a good agreement between the numerical and analytical solution is maintained in the long-time simulation. There is no visible deviation in both phase and amplitude of the acoustic wave for three different

Table 15

Errors and rates of convergence based on ρ of the 1-1-1-1 scheme (3rd order) and the 2-2-2-2 scheme (7th order) for the stationary vortex ($M = 0$).

| N | 1-1-1-1 scheme, $\alpha = 1.5$ | | | | 2-2-2-2 scheme, $\alpha = 12$ | | | |
|----------|--------------------------------|-------|------------------|-------|-------------------------------|-------|------------------|-------|
| | L_1 error | Order | L_∞ error | Order | L_1 error | Order | L_∞ error | Order |
| 20 (2) | 1.74E-03 | – | 1.74E-03 | – | 1.46E-03 | – | 1.46E-03 | – |
| 40 (4) | 1.59E-04 | 3.45 | 1.59E-04 | 3.45 | 5.45E-05 | 4.74 | 5.45E-05 | 4.74 |
| 80 (8) | 8.33E-06 | 4.26 | 8.33E-06 | 4.26 | 2.95E-07 | 7.53 | 2.95E-07 | 7.53 |
| 160 (16) | 3.77E-07 | 4.47 | 3.77E-07 | 4.47 | 7.55E-10 | 8.61 | 7.55E-10 | 8.61 |
| 320 (32) | 2.17E-08 | 4.12 | 2.17E-08 | 4.12 | 2.95E-12 | 8.00 | 2.95E-12 | 8.00 |

simulation time. The small discrepancy mainly appears near the peaks. In fact, the same level of deviation is also observed when N is increased to 40 and 80, which implies that the difference is caused by the embedded error from the linearization of the analytical solution. The same analysis is conducted with the 1-1-1-1 scheme, and similar behavior is observed which is not presented here.

The test case of the one-dimensional acoustic wave indicates that the current very high-order MLC schemes are able to maintain very small dispersive and dissipative errors at the same time. The long-time simulation results are stable and accurate which indicates the MLC schemes can be applied to computational aeroacoustics problems.

Two-dimensional isentropic vortex

To show the performance of the current MLC schemes in vortical flow simulations, a two-dimensional inviscid isentropic vortex in (x, y) plane is simulated. The similar test case is used by Mundis and Edoh [76,77]. The vortex is superimposed to a uniform steady mean flow in the x -direction. The mean flow conditions are set as follows,

$$\begin{aligned}
 p_\infty &= 101325 \text{ [Pa]}, & T_\infty &= 300 \text{ [K]}, & \rho_\infty &= \frac{p_\infty}{RT_\infty} \\
 a_\infty &= \sqrt{\gamma RT_\infty}, & U_\infty &= Ma_\infty \\
 \gamma &= 1.4, & R &= 286.94 \text{ [J} \cdot \text{kg}^{-1} \cdot \text{K}^{-1}]
 \end{aligned}
 \tag{88}$$

where U_∞ is the mean velocity. Mach number M is set to be 0 for stationary vortex, and 0.5 for convective vortex in the following simulations. The initial conditions ($t = 0$) involve the mean flow and a perturbation, which is an isentropic vortex defined as follows,

$$\begin{aligned}
 \delta u &= -\sqrt{RT_\infty} \frac{\varepsilon}{2\pi} (y - y_0) e^{\varphi(1-r^2)}, & \delta v &= \sqrt{RT_\infty} \frac{\varepsilon}{2\pi} (x - x_0) e^{\varphi(1-r^2)}, \\
 \delta T &= -T_\infty \frac{\varepsilon^2(\gamma - 1)}{16\varphi\gamma\pi^2} e^{2\varphi(1-r^2)}, & \frac{\delta p}{p_\infty} + 1 &= \left(\frac{\delta\rho}{\rho_\infty} + 1 \right)^\gamma = \left(\frac{\delta T}{T_\infty} + 1 \right)^{\gamma/\gamma-1}
 \end{aligned}
 \tag{89}$$

where (x_0, y_0) represents location of the vortex center, and $r^2 = (x - x_0)^2 + (y - y_0)^2$. The constants ε and φ are used to describe the strength and width of the vortex. The perturbations in (u, v) and T are defined independently in Eq. (89), while p and ρ can be determined by isentropic relations. In this paper, $\varepsilon = 1$ and $\varphi = 1$ are used. Therefore, the amplitude of perturbation in density $|\delta\rho/\rho_\infty|$ is about 6.27% at the vortex center. The vortex edge is defined at the location where $|\delta\rho/\rho_\infty| = 0.1\%$, corresponding to $r = 1.15$ m. The exact solution of this problem is a passive convection of the perturbed mean flow, and the vortex maintains its structure during the convection. It is appropriate for testing the performance of the MLC schemes in terms of vortex preservation, which is affected by the characteristic of dissipation, dispersion, and anisotropic errors of the MLC schemes.

The computational domain is a square field within the range of $0 < x < L$ and $0 < y < L$, where $L = 22.0$ m. At $t = 0$, the vortex core is located at the center of the domain. A uniform mesh with N grid panels in both dimensions is used, and periodic boundary conditions are set on all boundaries. This domain is large enough to reduce the boundary effects because the initial perturbations on the computational boundaries are negligible. The third-order 1-1-1-1 MLC scheme ($\alpha = 1.5$) and the seventh-order 2-2-2-2 MLC scheme ($\alpha = 12$) are used for spatial discretization. Meanwhile, a fourth-order Runge-Kutta method is applied to time integration, and the CFL number is set to be a small value of 0.1 to reduce temporal errors.

Similar to the previous case of the one-dimensional acoustic wave, a short-time simulation ($t = 0.01$ s) is first conducted to estimate the rate of convergence of the MLC schemes. Both the stationary vortex ($M = 0$) and convective vortex ($M = 0.5$) are tested. Table 15 and Table 16 show the errors and rates of convergence based on the solution of ρ , where Mach number is set to be 0 and 0.5 respectively. It should be noted that N is relatively larger compared with other test cases because of the larger domain in this case. However, the number of grid points within the vortex is very small, which are given in the brackets. The first observation from the tables is that the MLC schemes can surpass their expected orders for both Mach numbers. Specifically, the 1-1-1-1 scheme shows an approximate rate of convergence of 4, while the 2-2-2-2 scheme has about 8th-order rate of convergence. Second, the simulation with $M = 0$ is more accurate than the case of with $M = 0.5$. These tables show that the errors are smaller and estimated orders are higher for stationary vortex ($M = 0$), especially when

Table 16

Errors and rates of convergence based on ρ of the 1-1-1-1 scheme (3rd order) and the 2-2-2-2 scheme (7th order) for the convective vortex ($M = 0.5$).

| N | 1-1-1-1 scheme, $\alpha = 1.5$ | | | | 2-2-2-2 scheme, $\alpha = 12$ | | | |
|----------|--------------------------------|-------|------------------|-------|-------------------------------|-------|------------------|-------|
| | L_1 error | Order | L_∞ error | Order | L_1 error | Order | L_∞ error | Order |
| 20 (2) | 1.66E-03 | – | 1.37E-03 | – | 1.39E-03 | – | 1.35E-03 | – |
| 40 (4) | 2.26E-04 | 2.88 | 1.86E-04 | 2.88 | 6.89E-05 | 4.34 | 5.91E-05 | 4.51 |
| 80 (8) | 1.85E-05 | 3.61 | 1.36E-05 | 3.77 | 5.73E-07 | 6.91 | 5.25E-07 | 6.81 |
| 160 (16) | 1.12E-06 | 4.04 | 9.79E-07 | 3.80 | 3.09E-09 | 7.53 | 2.37E-09 | 7.79 |
| 320 (32) | 7.07E-08 | 3.99 | 6.18E-08 | 3.99 | 1.09E-11 | 8.14 | 8.36E-12 | 8.15 |

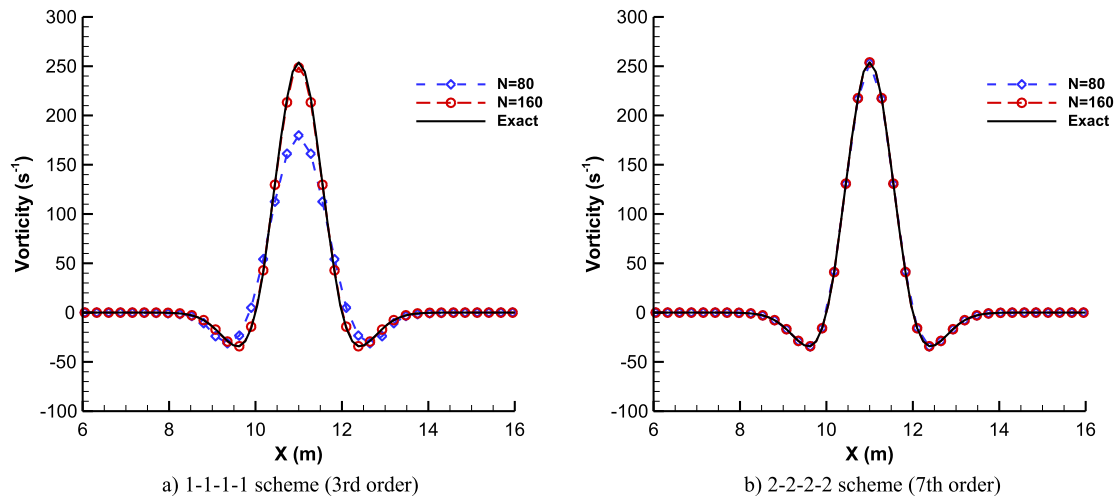


Fig. 32. Vorticity distribution on the centerline in the x -direction for the stationary vortex ($M = 0$) at $t = 1.267$ s.

N is large. This observation indicates that convective vortex is more difficult to be accurately captured than the stationary vortex, which is expected.

After the orders of the MLC schemes are validated in the short-time simulation, a long-time simulation is carried out in the next place. Specifically, the solution at $t = 1.267$ s is evaluated when the vortex has traveled about 100 diameters or 10 domain lengths in space for the case of $M = 0.5$. Figs. 31 and 32 show the vorticity distribution along the centerline ($y = 11$ m) for the stationary and convective vortices respectively. Both figures show that the dissipative and dispersive errors decrease clearly when the grid resolution increases. Specifically, Fig. 32 compares the solution of the 1-1-1-1 and 2-2-2-2 scheme for the case of $M = 0$. When $N = 80$, the 1-1-1-1 scheme has a large dissipative error; on the other hand, the 2-2-2-2 scheme is very accurate, indicating the advantage from a seventh-order of accuracy. When $N = 160$, both the results of the 1-1-1-1 and 2-2-2-2 scheme show very good agreement with the exact solution. Fig. 33 compares these two schemes for the case of $M = 0.5$. The convective vortex shows similar behaviors as the stationary vortex; however, the 1-1-1-1 scheme also shows a phase shift of the vortex besides the reduced amplitude when $N = 80$. In the center of the vortex, the corresponding wavenumber is large. The Fourier analysis in Section 3 shows the MLC schemes have small dissipative and dispersive errors for large wavenumbers. As a result, the vorticity is underestimated in the vortex center for the two cases of $M = 0$ and $M = 0.5$, and the phase speed is changed during the convection in the latter case. It should be mentioned that in the meshes with $N = 80$ and 160, only about 8 and 16 grid points are used to resolve the vortex structure. Therefore, the results in Figs. 31 and 32 also validate the spectral-like resolution of the MLC schemes.

To investigate the anisotropic errors, Figs. 33 and 34 show the density contours for the two cases of $M = 0$ and $M = 0.5$ at $t = 1.267$ s. The results of the 1-1-1-1 scheme when $N = 160$ are compared with the results of the 2-2-2-2 scheme when $N = 80$, both of which are accurate according to Figs. 31 and 32. The isotropic vortex is isotropic which means the structure should be identical in any arbitrary orientation. Therefore, all density contours should be concentric circles in the exact solution. These figures show that both the 1-1-1-1 and 2-2-2-2 scheme generate isotropic density distribution after the long-time simulation, in both stationary and convective vortex cases. In particular, the seventh-order 2-2-2-2 scheme can maintain the isotropy with only 8 grid points distributed in the vortex region ($N = 80$).

Fig. 36 shows the density distributions in the case of $M = 0.5$ along two straight lines passing through the vortex core, at an angle $\theta = 0$ and $\pi/4$ with respect to the x -axis. The results of the 1-1-1-1 and 2-2-2-2 schemes are compared in the same mesh of $N = 160$. The figure shows that the density distributions along the two lines of $\theta = 0$ and $\theta = \pi/4$ agree very well, except that the latter shows slightly larger error at the peak. These results demonstrate that the MLC schemes have very small anisotropic errors, which is consistent with the isotropic density contours in Fig. 35. In the approximation

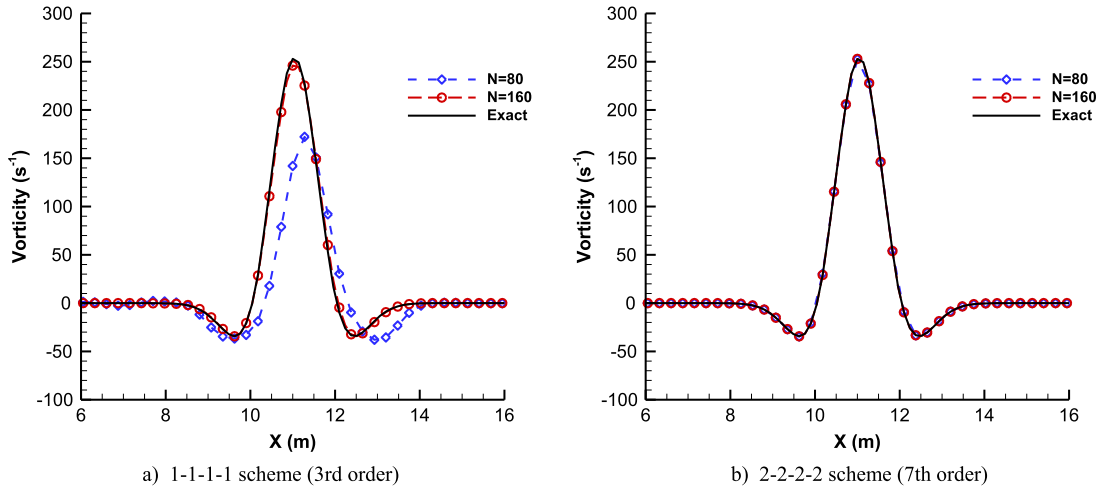


Fig. 33. Vorticity distribution on the centerline in the x-direction for the convective vortex ($M = 0.5$) at $t = 1.267$ s.

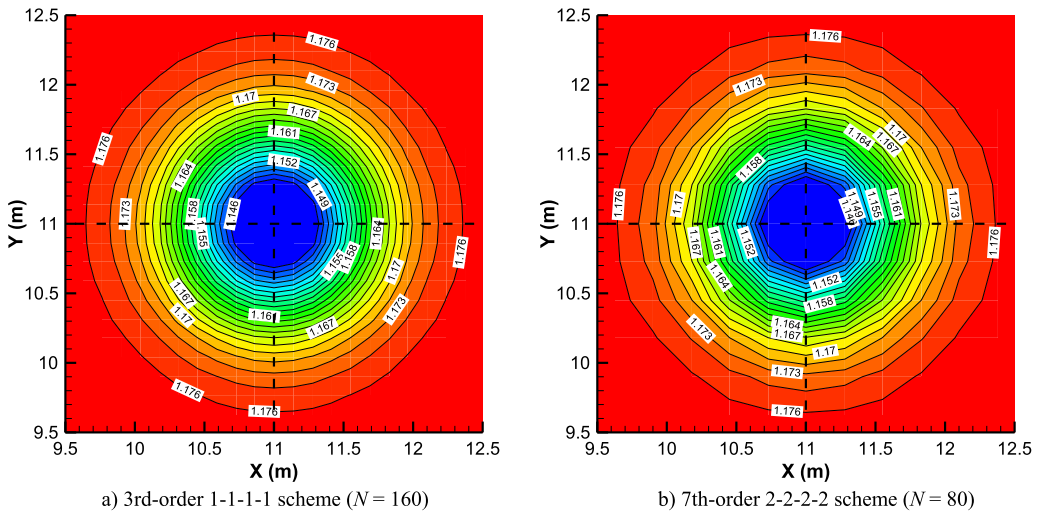


Fig. 34. Density contours in the case of stationary vortex ($M = 0$) at $t = 1.267$ s.

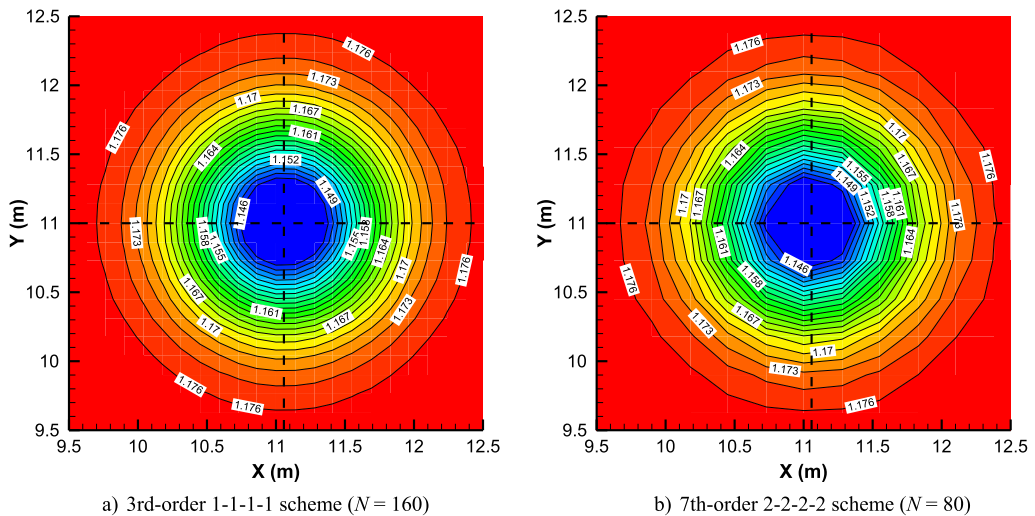


Fig. 35. Density contours in the case of convective vortex ($M = 0.5$) at $t = 1.267$ s.

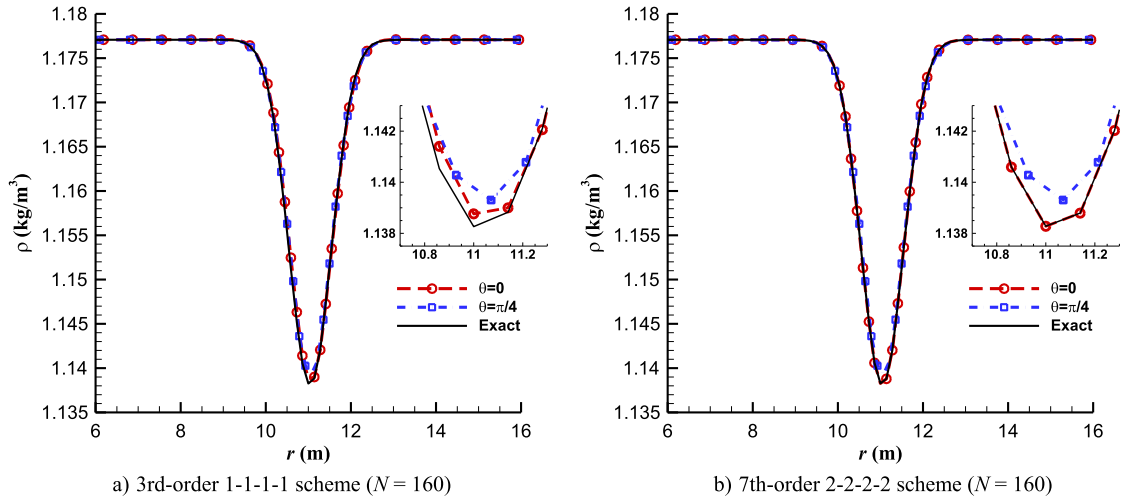


Fig. 36. Density distribution along two centerlines in different orientations ($\theta = 0$ and $\theta = \pi/4$) in the case of convective vortex ($M = 0.5$) at $t = 1.267$ s.

of cross derivatives, our MLC schemes take information from neighboring points in different orientations, instead of doing approximation in a single x - or y -direction as many conventional finite difference methods. Hence, it has the advantage to overcome the anisotropic error.

In this section, the MLC schemes are evaluated for solving the two-dimensional Euler equations in multiple cases involving entropy, acoustic, or vorticity perturbations. The third-order 1-1-1-1 scheme with $\alpha = 1.5$, and the seventh-order 2-2-2-2 scheme with $\alpha = 12$ are used for these simulations. First, all the test cases indicate the expected order of accuracy can be achieved, and the MLC schemes with upwinding even surpass the expected order by one in multiple test cases. Second, the MLC schemes generate satisfying results on coarse meshes with very few grid points, which validate the spectral-like resolution. Particularly, the long-time simulation is performed in the cases of the acoustic wave and isentropic vortex. The result of the acoustic wave shows the high fidelity of small perturbations benefit from the small dissipative and dispersive error of the MLC schemes; the result of the two-dimensional isentropic vortex indicates small anisotropy of the new schemes.

4.3. Navier–Stokes equations for compressible flows

The Navier–Stokes equations for compressible viscous flows have been introduced in Eq. (1). Like the case of the Euler equations, auxiliary equations need to be derived before applying the MLC schemes. Taking gradient on Eq. (1), we obtain the auxiliary equations for the Navier–Stokes equations as follows,

$$\frac{\partial U_{x_k}}{\partial t} + \frac{\partial F_{jx_k}}{\partial x_j} + \frac{\partial F_{vjx_k}}{\partial x_j} = 0 \tag{90}$$

where the subscripts x_k and j are directional derivatives and dummy index respectively, same as in the Euler equations, and v represents viscous flux term. In vector forms, the original Navier–Stokes equations (1) and the auxiliary equations (90) can be written as,

$$\frac{\partial}{\partial t} \begin{bmatrix} U \\ U_{x_k} \end{bmatrix} = - \begin{bmatrix} A_j U_{x_j} \\ F_{jx_k x_j} \end{bmatrix} - \begin{bmatrix} F_{vjx_j} \\ F_{vjx_k x_j} \end{bmatrix} \tag{91}$$

Note that Eq. (91) have the viscous terms on the right-hand side, which is the only difference from Eq. (76). Therefore, the treatment of the first term on the right-hand side of Eq. (91) follows exactly the same procedures for the Euler equations. In the viscous part, the term $F_{vjx_k x_j}$ also needs an approximation. It can be computed by high-order MLC schemes from F_{vj} and F_{vjx_k} , like the treatment for the inviscid part. However, only the viscous flux F_{vj} can be calculated exactly. The first derivatives F_{vjx_k} needs to be numerically approximated which is explained below. The expression of F_{vj} has been given in Eq. (4), and the expression of F_{vjx_k} is derived by taking the derivative of Eq. (4) as follows,

$$F_{vjx_k} = \begin{bmatrix} 0 \\ \tau_{1jx_k} \\ \tau_{2jx_k} \\ \tau_{3jx_k} \\ \tau_{ijx_k} u_i + \tau_{ij} u_{ix_k} + q_{jx_k} \end{bmatrix} \tag{92}$$

Table 17
Summary of boundary conditions for the Navier–Stokes equations.

| | Value | Tangential derivative (x) | Normal derivative (y) |
|-------|--|---|-------------------------|
| p | Zero-gradient fitting | Compact finite difference approximation | Zero |
| u_i | Non-slip wall ($\mathbf{u} = \mathbf{U}_{\text{wall}}$) | Zero | Two-layer extrapolation |
| T | 1) Isothermal wall ($T = T_{\text{wall}}$) | Zero | Two-layer extrapolation |
| | 2) Adiabatic wall (Zero-gradient fitting) | Compact finite difference approximation | Zero |

where the subscript i is a dummy index, and the derivatives of viscous stress, molecular viscosity coefficient, and heat flux can be obtained easily as follows,

$$\tau_{ijx_k} = -\mu_{x_k}(u_{ix_j} + u_{jx_i}) - \mu(u_{ix_jx_k} + u_{jx_ix_k}) + \frac{2}{3}(\mu_{x_k}u_{lx_l} + \mu u_{lx_lx_k})\delta_{ij} \tag{93}$$

$$q_{jx_k} = -\kappa T_{x_jx_k} \tag{94}$$

The molecular viscosity coefficient μ and its derivative can be calculated by Sutherland's law in the form,

$$\mu = \mu_0 \left(\frac{T}{T_0}\right)^{3/2} \frac{T_0 + T_s}{T + T_s} \tag{95}$$

$$\mu_{x_k} = \mu_0 \left(\frac{T}{T_0}\right)^{1/2} \left(\frac{T_0 + T_s}{T + T_s}\right) \left[\frac{3}{2T_0} - \frac{T}{T_0(T + T_s)}\right] T_{x_k} \tag{96}$$

Combining Eqs. (4)–(8) and (92)–(94), we find that F_{vj} and F_{vjx_k} are functions of the primitive variables (u_i, T) and their derivatives in the following form,

$$F_{vj} = f(u_i, T, u_{ix_j}, T_{x_j})$$

$$F_{vjx_k} = f'(u_i, T, u_{ix_j}, T_{x_j}, u_{ix_kx_j}, T_{x_kx_j}) \tag{97}$$

where $i, j, k \in \{1, 2, 3\}$. At every grid point, we know U and U_{x_k} from the solution, so u_i, T and their first derivatives can be obtained easily. However, $u_{ix_kx_j}$ and $T_{x_kx_j}$ in Eq. (97) needs to be approximated by finite difference methods.

The procedures of discretization for Navier–Stokes equations include three steps. Step 1 is the discretization for inviscid flux, which is described in Section 4.2. In Step 2, we apply the central MLC schemes to approximate ($u_{ix_kx_j}, T_{x_kx_j}$) from (u_i, T) and their first derivatives. Then using Eq. (97), the value of F_{vj} and F_{vjx_k} at each point is obtained. In Step 3, we apply the same central MLC schemes to compute $F_{vjx_kx_j}$ from F_{vj} and F_{vjx_k} . After that, all the terms in the right-hand side of Eq. (91) is obtained. It should be noted that the central MLC schemes are applied twice in the approximation of viscous terms. To be consistent, the formulas for these central schemes are the same as those for $F_{jx_kx_j}$ in Step 1. However, $\alpha = 0$ is always used in the viscous terms due to their elliptic property. After the three steps are finished, Eq. (91) becomes a system of ordinary differential equations, which can be solved through the method of lines.

The boundary conditions of U and U_{x_k} are needed for the Navier–Stokes simulations. For the inflow and outflow boundaries, the boundary conditions are very similar to those for the Euler equations. The details are not discussed in this paper for the sake of length. However, the solid wall condition for the Navier–Stokes equations is different, because the viscous effect is dominant near the wall. Flow quantities on the solid wall boundaries are ($p, u_i, T, p_x, u_{ix}, T_x, p_y, u_{iy}, T_y$), where $i = 1, 2, 3$. The subscript x and y represent the tangential and normal direction of the wall, which follows the schematic in Fig. 30. The boundary conditions for ρ can be determined through thermodynamic relations. Specifically, the physical conditions in the Navier–Stokes simulations are: the non-slip condition for u_i , and the isothermal or adiabatic condition for T . Table 17 summarizes the boundary conditions for the Navier–Stokes simulations with the MLC schemes. According to boundary layer equations, the zero-gradient condition for p can be derived, i.e., p_y on the wall is zero. This condition can usually be extended to the Navier–Stokes simulations. Then, a zero-gradient fitting from the interior points can be used to determine p on the wall. The non-slip boundary condition is applied to $\mathbf{u} = (u_1, u_2, u_3)$. There is no relative motion between the wall and its neighboring fluid particles, i.e., $\mathbf{u} = \mathbf{U}_{\text{wall}}$. If the wall is static, all components u_i are 0. Two types of boundary conditions of T can be used, 1) isothermal wall; 2) adiabatic wall. For isothermal case, T is a constant value; and for the adiabatic case, T_y at the wall is zero which means no heat conduction through the wall. In the adiabatic case, T is determined by the zero-gradient fitting from interior temperatures. The tangential derivatives u_{ix} and T_x in the isothermal case are set to be 0. For p_x and T_x in the adiabatic case, they are approximated by Zhong's compact schemes [1] along the tangential direction of the wall. For u_{iy} and T_y in the isothermal case, the two-layer extrapolation can be used.

The two-layer extrapolation and the zero-gradient fitting are very similar, which follows the same multi-layer idea of the MLC schemes. In the following description, we use the T for illustration. The normal derivative is notated as T' for simplicity. For a base point i , the approximation of T' has the form,

$$T'_i = \frac{1}{h} \sum_{l=-L_1}^{L_2} a_l T_{i+l} + \sum_{\substack{m=-M_1 \\ m \neq 0}}^{M_2} b_m T'_{i+m} - \frac{\alpha}{(p+1)!} T_i^{p+1} h^p + \dots \tag{98}$$

where all the coefficients are defined in the same way as in Eq. (12). These two formulas are very similar, both include two layers of information – value and first derivatives. However, the second derivative in Eq. (12) is replaced by the first derivative in Eq. (98). As a result, this approximation of T'_i can be considered as a combination of the interpolation/extrapolation from T'_{i+m} and the finite difference approximation from T_{i+l} . The coefficients a_l and b_m can be derived from the Taylor series expansion. On a boundary point ($i = 1$), one-sided stencils are used ($L_1 = M_1 = 0$), then the formulas for the two-layer extrapolation are obtained, as follows,

$$T'_1 = \frac{1}{h} \sum_{l=0}^{L_2} a_l T_{l+1} + \sum_{m=1}^{M_2} b_m T'_{m+1} \tag{99}$$

For the isothermal wall, all values at the right-hand side of Eq. (99) are known, therefore, T'_1 on the wall can be computed. By using the first derivatives in the inner field which are already solved, the two-layer extrapolation achieved the same accuracy with fewer points compared with finite difference approximations or conventional extrapolation of normal derivatives. Hence, it is more compatible with the MLC schemes. The formulas of the two-layer extrapolations on boundary points with different orders of accuracy are given in Appendix A.2.

In the adiabatic case, T'_1 on the wall is zero, and T_1 is the unknown. With some algebraic operations, Eq. (99) can be written in the following form,

$$T_1 = -\frac{1}{a_0} \left(\sum_{l=1}^{L_2} a_l T_{l+1} + h \sum_{m=1}^{M_2} b_m T'_{m+1} \right) \tag{100}$$

where all the coefficients keep the same values from Eq. (99). The approximation in Eq. (100) is termed the zero-gradient fitting, which also applies to the approximation of boundary pressures.

In the following part of this section, the two-dimensional Navier–Stokes equations in the Cartesian coordinates are solved by the MLC schemes. The results of a steady supersonic Couette flow are presented as an example. The implementation of more complex Navier–Stokes simulations such as hypersonic boundary-layer transition is ongoing.

Steady supersonic Couette flow

The supersonic Couette flow can be considered as a simplified model of the hypersonic boundary layer. The steady-state solutions are one-dimensional functions of wall-normal distance y , while the unsteady Couette flows are two-dimensional transient flows if disturbances exist. More details about can be found in [78].

In the two-dimensional Couette flow, the bottom wall is stationary, and the top wall is moving at a constant velocity U_∞ . The flow conditions are given as follows,

$$M_\infty = 2, \quad Re_\infty = 100, \quad T_\infty = 300 \text{ [K]} \\ U_\infty = M_\infty \sqrt{\gamma R T_\infty}, \quad p = 101325 \text{ [Pa]}, \quad T_w = T_r \tag{101}$$

where γ is 1.4 and the gas constant R is $286.94 \text{ [m}^2 \cdot \text{s}^{-2} \cdot \text{K}^{-1}]$. A small Reynolds number (Re_∞) is used to maintain a laminar and stable flow in the channel. The isothermal conditions are used on the boundaries. The top wall has temperature T_∞ , and the bottom wall temperature T_w is set to be equivalent with the recovery temperature T_r which is calculated by,

$$T_r = T_\infty \left[1 + \frac{(\gamma - 1)}{2} Pr M_\infty^2 \right] \tag{102}$$

with the Prandtl number (Pr) is 0.72. As a result, the bottom wall can also be considered as adiabatic. The viscosity coefficient μ is calculated by Sutherland’s law in Eq. (95), where the constants are set as follows,

$$\mu_0 = 1.7894 \times 10^{-5} \left[\frac{\text{kg}}{\text{m} \cdot \text{s}} \right], \quad T_0 = 288 \text{ [K]}, \quad T_s = 110.3333 \text{ [K]} \tag{103}$$

The exact solution of steady Couette flow can be attained by shooting methods, the details of the solution procedure can be found in [78]. The resulting solution is given in the following implicit form,

$$U_\infty \int_0^{u^*} \mu_0 \left(\frac{T_\infty}{T_0} \right)^{1.5} \left(\frac{T}{T_\infty} \right)^{1.5} \left(\frac{T_0 + T_s}{T + T_s} \right) du^* = \tau_w y \\ T(u^*) = T_\infty \left[1 + \left(\frac{T_w - T_r}{T_\infty} \right) (1 - u^*) + \frac{(\gamma - 1)}{2} Pr M_\infty^2 (1 - (u^*)^2) \right] \tag{104}$$

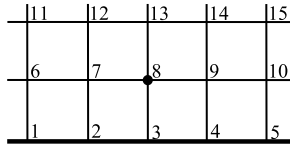


Fig. 37. Stencil for the boundary closure scheme (6th order) for cross derivatives.

where $u^* = u/U_\infty$ is the non-dimensional velocity, and y is the distance from the bottom wall. The subscript ∞ and w represent the top and bottom wall respectively. The solution of T is a function of u^* only. The wall shear stress τ_w in the solution can be calculated from,

$$\tau_w = \frac{U_\infty}{H} \int_0^1 \mu_0 \left(\frac{T_\infty}{T_0} \right)^{1.5} \left(\frac{T}{T_\infty} \right)^{1.5} \left(\frac{T_0 + T_s}{T + T_s} \right) du^* \tag{105}$$

where H is the height of the channel and can be calculated from Re_∞ .

The computational domain is a rectangular field in $0 < x < L$ and $0 < y < H$. The length L in the x -direction is arbitrary for steady simulations because the flow is fully developed. A uniform mesh with 6 grid panels in x dimension and N grid panels in y dimension is used. Periodic boundary conditions are used on inflow and outflow boundaries; non-slip and isothermal wall conditions are applied to the bottom and top walls. The third-order 1-1-1 scheme with $\alpha = 1.5$ and the seventh-order 2-2-2-2 scheme with $\alpha = 12$ are applied to the two-dimensional steady Couette flow simulations. Zhong's fifth-order explicit scheme with $\alpha = -6$ [1] is also applied for comparison. A third-order Runge-Kutta method is used for time integration.

With the existence of solid walls in the Couette flow, the stencils of inner schemes may go beyond the computational domain in the region near the wall. As a result, the boundary closure schemes are also needed. It should be noted that the Navier-Stokes equations are not solved on the walls, instead, the physical boundary conditions are applied. In general, the higher-order inner schemes lead to more complicated boundary closure schemes than the lower-order schemes. For this test case, the third-order 1-1-1 scheme uses a three-point stencil and needs no boundary closure schemes; the seventh-order 2-2-2-2 scheme uses a seven-point stencil and needs the boundary closure scheme at the wall adjacent points. The details of boundary closure schemes coupled with the 2-2-2-2 scheme are described as follows.

The one-dimensional boundary closure schemes have been discussed in Section 3.3, and they are applied to the second derivatives terms u_{xx} and u_{yy} , where u can represent any flow quantities such as F_j , F_{vj} , u_k , and T . Specifically, the sixth-order boundary closure schemes in case 3 as described in Table 2 are selected for the Couette flow simulation with the seventh-order 2-2-2-2 scheme. All the formulas of boundary closure schemes are given in the Appendix A.1. For the cross derivatives terms u_{xy} , the two-dimensional boundary closure schemes are needed. Same as the inner schemes, there are many freedoms in the cross-derivative approximations. As a result, the formula of the two-dimensional boundary closure scheme on a specific stencil is not unique. However, the choice of two-dimensional boundary closure schemes become more complicated than inner schemes, because bias stencils may need to be considered. Here, only a specific sixth-order boundary closure scheme for u_{xy} is presented as an example. The stencil and numbering of the index are shown in Fig. 37 where the bold line represents the wall, and the formula of this scheme is,

$$\begin{aligned} (u_{xy})_{(i,j)=8} = & \frac{1}{h^2} \left(\frac{1}{24}u_1 - \frac{1}{3}u_2 + \frac{1}{3}u_4 - \frac{1}{24}u_5 - \frac{1}{24}u_{11} + \frac{1}{3}u_{12} - \frac{1}{3}u_{14} + \frac{1}{24}u_{15} \right) \\ & + \frac{1}{h} \left(-\frac{1}{2}(u_x)_3 + \frac{1}{2}(u_x)_{13} \right) + \frac{1}{h} \left(\frac{1}{12}(u_y)_6 - \frac{2}{3}(u_y)_7 + \frac{2}{3}(u_y)_9 - \frac{1}{12}(u_y)_{10} \right) \\ & + o(h^6) \end{aligned} \tag{106}$$

It shows that the stencil size is reduced to 3 points in the vertical direction, and it is still the same as the 2-2-2-2 inner scheme in the horizontal direction, which uses 5 points. Therefore, it is still symmetric about the base point 8 in the horizontal direction. It turns out this specific choice above is stable and can maintain the seventh-order accuracy of the 2-2-2-2 schemes in the Couette flow simulations. However, the choice is not unique, and there may exist other approximations which can outperform this specific choice for other simulation problems.

Fig. 38 shows the non-dimensional temperature T^* and velocity u^* distribution generated by the 2-2-2-2 MLC scheme on a coarse mesh with 7 grid points ($N = 6$). A very good agreement without obvious deviation between the numerical and exact solution is achieved, indicating that the spectral-like resolution of the MLC schemes is maintained in the Navier-Stokes simulations. As we can show later, it is difficult to achieve a satisfying resolution on such a coarse mesh using conventional finite difference methods like Zhong's explicit schemes.

To illustrate the high spectral resolution and accuracy of the MLC schemes further, the numerical errors based on T^* of Zhong's fifth-order explicit scheme, the third-order 1-1-1 scheme, and the seventh-order 2-2-2-2 scheme are given

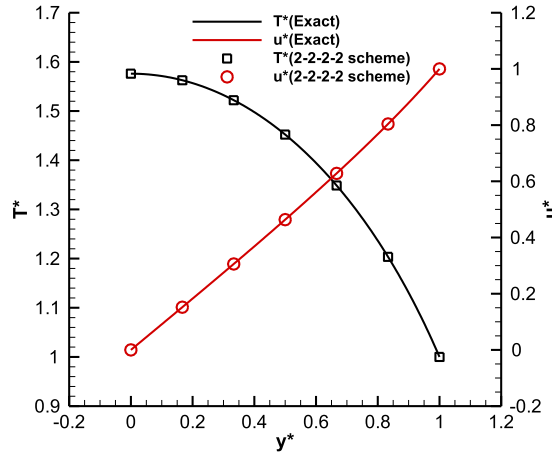


Fig. 38. Non-dimensional temperature and velocity distribution in the steady Couette flow simulation with the seventh-order 2-2-2-2 scheme ($N = 6$).

Table 18

Errors and rates of convergence based on T^* of the seventh-order 2-2-2-2 scheme for steady supersonic Couette flow.

| N | 2-2-2-2 scheme, $\alpha = 12$ | | | | | |
|-----|-------------------------------|-------|-------------|-------|------------------|-------|
| | L_1 error | Order | L_2 error | Order | L_∞ error | Order |
| 8 | 1.06E-06 | | 1.25E-06 | | 1.97E-06 | |
| 16 | 1.79E-08 | 5.88 | 2.22E-08 | 5.81 | 4.13E-08 | 5.57 |
| 32 | 1.12E-10 | 7.32 | 1.37E-10 | 7.35 | 3.52E-10 | 6.88 |
| 64 | 7.29E-13 | 7.27 | 8.99E-13 | 7.25 | 1.55E-12 | 7.82 |

Table 19

Errors and rates of convergence based on T^* of the third-order 1-1-1-1 scheme for steady supersonic Couette flow.

| N | 1-1-1-1 scheme, $\alpha = 1.5$ | | | | | |
|-----|--------------------------------|-------|-------------|-------|------------------|-------|
| | L_1 error | Order | L_2 error | Order | L_∞ error | Order |
| 8 | 7.77E-05 | | 8.81E-05 | | 1.28E-04 | |
| 16 | 7.82E-06 | 3.31 | 9.09E-06 | 3.28 | 1.42E-05 | 3.17 |
| 32 | 5.88E-07 | 3.73 | 7.07E-07 | 3.68 | 1.18E-06 | 3.59 |
| 64 | 4.05E-08 | 3.86 | 5.02E-08 | 3.81 | 8.78E-08 | 3.75 |

Table 20

Errors and rates of convergence based on T^* of Zhong's fifth-order explicit scheme for steady supersonic Couette flow.

| N | Zhong's explicit scheme, $\alpha = -6$ | | | | | |
|-----|--|-------|-------------|-------|------------------|-------|
| | L_1 error | Order | L_2 error | Order | L_∞ error | Order |
| 8 | 1.75E-04 | | 2.07E-04 | | 3.76E-04 | |
| 16 | 6.91E-06 | 4.66 | 8.60E-06 | 4.59 | 1.74E-05 | 4.43 |
| 32 | 2.59E-07 | 4.74 | 3.41E-07 | 4.66 | 8.60E-07 | 4.34 |
| 64 | 9.96E-09 | 4.70 | 1.38E-08 | 4.62 | 4.56E-08 | 4.24 |

in Tables 18 to 20 respectively. The first observation from these tables is that all three schemes can reach the expected orders of accuracy for Navier–Stokes calculation, which is 7 for the 2-2-2-2 scheme, 3 for the 1-1-1-1 scheme, and 5 for Zhong's explicit scheme. Next, comparing the error on the same mesh, we can observe that the 2-2-2-2 scheme shows the smallest errors for all different N values which are consistent with its seventh-order accuracy. On the other hand, a remarkable fact from Table 19 and Table 20 is that the third-order 1-1-1-1 scheme shows smaller error than Zhong's fifth-order explicit scheme when $N = 8$, and their errors are about the same for $N = 16$. Only when $N = 32$ and 64 cases, Zhong's explicit scheme is more accurate than the 1-1-1-1 scheme. This observation can be regarded as a further evidence of the spectral-like resolution, where the lower order MLC scheme shows better accuracy than higher order conventional finite difference methods on coarse meshes, benefited from the additional degrees of freedom on each grid point in the MLC schemes. When the grid resolution is not fine enough, the non-dimensional wavenumber becomes large. Therefore, the accuracy of numerical results mainly depends on the resolving ability in large k region. As analyzed in Section 3.1, our MLC schemes can have very good accuracy even when k is larger than π , which is the limiting resolution of conventional finite difference methods. As a result, they have much better resolution on coarse meshes, and should significantly reduce the requirement of grid numbers for most Navier–Stokes simulations.

5. Discussions and conclusions

In this paper, a new very high-order upwind multi-layer compact (MLC) scheme is derived. The goal of the MLC scheme is to solve, with very high-order of accuracy, flows involving very complex physics but over simple geometries. In the multi-layer idea, the first derivative is introduced on every grid point, and both values and derivatives are used to construct finite difference schemes. As a result, both the accuracy and the spectral resolution can be significantly improved. Even though the MLC schemes introduce additional equations and degrees of freedom, only the auxiliary equations are nontrivial, which contributes to good computational efficiency. The upwind MLC schemes are derived based on the idea of constructing upwind schemes on centered stencils with adjustable parameters to control the dissipation. Two typical examples are the third-order 1-1-1-1 scheme with $\alpha = 1.5$ and the seventh-order 2-2-2-2 scheme with $\alpha = 12$. Fourier analysis is performed to investigate the accuracy and spectral resolution of the MLC schemes, and the stability analysis with matrix method is conducted to analyze the boundary closure schemes. Various flow problems governed by the linear advection equation, the nonlinear Euler equations, and the Navier–Stokes equations are simulated with the new schemes. The main conclusions are listed below.

1. Fourier analysis results show that the dissipative, dispersive, and anisotropic errors of the MLC schemes are much smaller than those of conventional finite difference methods (Zhong's explicit and compact schemes [1]). Due to the additional degrees of freedom, which overcomes the aliasing in conventional finite difference methods, the resolution in large wavenumber region is notably improved while maintaining the compact stencil. Comparison of the 1-1-1-1 scheme and Zhong's fifth-order explicit scheme indicates that even lower order MLC scheme with less total points (values and derivatives) within the stencil can have better resolution and smaller dissipation than higher order conventional scheme. The value of α has an impact on the stability, accuracy, and stiffness of the MLC scheme. Larger α leads to better stability, larger dissipation and it slightly increases dispersion. However, the choice of α is not unique with the following criterion satisfied, which is α should be large enough to ensure the stability of both interior scheme and boundary closure schemes, and it should not be too large to keep small dissipation and avoid stiffness. From the Fourier analysis, the seventh-order 2-2-2-2 scheme with an α value of 12 has the best accuracy and spectral resolution.
2. The eigenvalue spectrum of stability analysis shows that the stable boundary closure schemes can be derived because of the compactness of the stencils. The upwind coefficients play an important role in stabilizing the high-order boundary closure schemes. Like most finite difference schemes, high-order MLC schemes have more severe boundary instability problem than low-order MLC schemes. The seventh-order 2-2-2-2 scheme with $\alpha = 12$ is stable only when coupled with sixth-order boundary closure schemes on the boundary point and boundary adjacent points. The third-order 1-1-1-1 scheme with any non-negative α is stable when coupled with both third-order and second-order boundary closure schemes.
3. Numerical experiments of various one-dimensional and two-dimensional test cases in the linear advection equation, the Euler equations, and the Navier–Stokes equations are performed with the very high-order MLC schemes. All the test cases indicate the MLC schemes can achieve or surpass the expected orders of accuracy. They can generate satisfying results on coarse meshes with very few grid points, which validate the spectral-like resolutions. The computational efficiency is tested on the advection equation, and the results show the MLC scheme can significantly save grid numbers compared with Zhong's explicit scheme, which also leads to shorter CPU time. Particularly, the results of acoustic wave show the small dissipative and dispersive error can be attained simultaneously; the results of two-dimensional isentropic vortex indicate that the MLC schemes have small anisotropy; and the steady Couette flow results show that the application of high-order MLC schemes to the Navier–Stokes equations is successful, which is a good start for simulations of transient flows with more complex physics in the future.

In summary, the new very high-order MLC schemes have the properties of simple formulations, high-order accuracies, compact stencils, and spectral-like resolutions in both one- and two-dimensional cases. Future work will include the application of the MLC schemes to direct numerical simulation of hypersonic boundary-layer transition. In particular, it will be combined with a high-order shock-fitting algorithm, which is considered in Zhong's previous work [1]. The mechanisms of boundary layer stability, receptivity, and transition, which are summarized in [3], will also be investigated using the MLC schemes.

Acknowledgments

This research was sponsored by the Air Force Office of Scientific Research, USAF, under AFOSR Grants #FA9550-15-1-0268, monitored by Dr. Ivett Leyva. The research was also supported by Office of Naval Research (ONR) Grant #N00014-17-1-2343, monitored by Dr. Knox Millsaps previously and by Dr. Eric Marineau presently. The computations are mainly run on XSEDE resources provided by TACC under grant number TG-ASC090076 supported by National Science Foundation. The first author Zeyu Bai would like to acknowledge the financial support from the China Scholarship Council, under Grants #201406030100. The views and conclusions contained herein are those of the authors and should not be interpreted as necessarily representing the official policies or endorsements either expressed or implied, of the Air Force Office of Scientific Research or the U.S. Government.

Appendix A

A.1. Schemes for second derivatives on bias stencils

All the coefficients in Appendix A.1 are defined in accordance with Eq. (12).

0-1-0-1 scheme (2nd order)

$$a_0 = -6, \quad a_1 = 6, \quad b_0 = -4, \quad b_1 = -2. \quad (107)$$

0-2-0-1 scheme (3rd order)

$$a_0 = -\frac{17}{2}, \quad a_1 = 8, \quad a_2 = \frac{1}{2}, \quad b_0 = -5, \quad b_1 = -4. \quad (108)$$

0-3-0-3 scheme (6th order)

$$a_0 = -\frac{97}{6}, \quad a_1 = 0, \quad a_2 = \frac{27}{2}, \quad a_3 = \frac{8}{3}, \quad b_0 = -\frac{22}{3}, \quad b_1 = -18, \quad b_2 = -9, \quad b_3 = -\frac{2}{3}. \quad (109)$$

0-4-0-3 scheme (7th order)

$$a_0 = -\frac{145}{8}, \quad a_1 = -8, \quad a_2 = 18, \quad a_3 = 8, \quad a_4 = \frac{1}{8}, \\ b_0 = -\frac{47}{6}, \quad b_1 = -24, \quad b_2 = -18, \quad b_3 = -\frac{8}{3}. \quad (110)$$

1-0-1-0 scheme (2nd order)

$$a_{-1} = 6, \quad a_0 = -6, \quad b_{-1} = 2, \quad b_0 = 4. \quad (111)$$

1-1-2-1 scheme (5th order)

$$a_{-1} = \frac{63}{22}, \quad a_0 = -\frac{48}{11}, \quad a_1 = \frac{3}{2}, \quad b_{-2} = -\frac{1}{66}, \quad b_{-1} = \frac{19}{22}, \quad b_0 = \frac{19}{22}, \quad b_1 = -\frac{23}{66}. \quad (112)$$

1-2-1-2 scheme (6th order)

$$a_{-1} = \frac{28}{27}, \quad a_0 = -\frac{11}{2}, \quad a_1 = 4, \quad a_2 = \frac{25}{54}, \quad b_{-1} = \frac{2}{9}, \quad b_0 = -2, \quad b_1 = -2, \quad b_2 = -\frac{1}{9}. \quad (113)$$

1-3-1-2 scheme (7th order)

$$a_{-1} = \frac{59}{72}, \quad a_0 = -\frac{115}{18}, \quad a_1 = \frac{9}{2}, \quad a_2 = \frac{19}{18}, \quad a_3 = \frac{1}{72}, \\ b_{-1} = \frac{1}{6}, \quad b_0 = -\frac{8}{3}, \quad b_1 = -3, \quad b_2 = -\frac{1}{3}. \quad (114)$$

2-0-1-0 scheme (3rd order)

$$a_{-2} = \frac{1}{2}, \quad a_{-1} = 8, \quad a_0 = -\frac{17}{2}, \quad b_{-1} = 4, \quad b_0 = 5. \quad (115)$$

2-1-2-1 scheme (6th order)

$$a_{-2} = \frac{25}{54}, \quad a_{-1} = 4, \quad a_0 = -\frac{11}{2}, \quad a_1 = \frac{28}{27}, \quad b_{-2} = \frac{1}{9}, \quad b_{-1} = 2, \quad b_0 = 2, \quad b_1 = -\frac{2}{9}. \quad (116)$$

2-1-1-1 scheme (5th order)

$$a_{-2} = \frac{1}{18}, \quad a_{-1} = 3, \quad a_0 = -\frac{9}{2}, \quad a_1 = \frac{13}{9}, \quad b_{-1} = 1, \quad b_0 = 1, \quad b_1 = -\frac{1}{3}. \quad (117)$$

3-0-3-0 scheme (6th order)

$$a_{-3} = \frac{8}{3}, \quad a_{-2} = \frac{27}{2}, \quad a_{-1} = 0, \quad a_0 = -\frac{97}{6}, \quad b_{-3} = \frac{2}{3}, \quad b_{-2} = 9, \quad b_{-1} = 18, \quad b_0 = \frac{22}{3}. \quad (118)$$

3-1-2-1 scheme (7th order)

$$\begin{aligned} a_{-3} &= \frac{1}{72}, & a_{-2} &= \frac{19}{18}, & a_{-1} &= \frac{9}{2}, & a_0 &= -\frac{115}{18}, & a_1 &= \frac{59}{72}, \\ b_{-2} &= \frac{1}{3}, & b_{-1} &= 3, & b_0 &= \frac{8}{3}, & b_1 &= -\frac{1}{6}. \end{aligned} \quad (119)$$

4-0-3-0 scheme (7th order)

$$\begin{aligned} a_{-4} &= \frac{1}{8}, & a_{-3} &= 8, & a_{-2} &= 18, & a_{-1} &= -8, & a_0 &= -\frac{145}{8}, \\ b_{-3} &= \frac{8}{3}, & b_{-2} &= 18, & b_{-1} &= 24, & b_0 &= \frac{47}{6}. \end{aligned} \quad (120)$$

A.2. Formulas for two-layer extrapolations and zero-gradient fittings

All the coefficients in Appendix A.2 are defined in accordance with Eqs. (98)–(100). The boundary point is numbered as $i = 0$; L_1 and M_1 are 0 which means only points on the inner side of the boundary are used for approximations.

1st order

$$a_0 = -1, \quad a_1 = 1, \quad b_1 = 0. \quad (121)$$

2nd order

$$a_0 = -2, \quad a_1 = 2, \quad b_1 = -1. \quad (122)$$

3rd order

$$a_0 = -\frac{5}{2}, \quad a_1 = 2, \quad a_2 = \frac{1}{2}, \quad b_1 = -2. \quad (123)$$

4th order

$$a_0 = -3, \quad a_1 = 0, \quad a_2 = 3, \quad b_1 = -4, \quad b_2 = -1. \quad (124)$$

5th order

$$a_0 = -\frac{10}{3}, \quad a_1 = -3, \quad a_2 = 6, \quad a_3 = \frac{1}{3}, \quad b_1 = -6, \quad b_2 = -3. \quad (125)$$

6th order

$$a_0 = -\frac{11}{3}, \quad a_1 = -9, \quad a_2 = 9, \quad a_3 = \frac{11}{3}, \quad b_1 = -9, \quad b_2 = -9, \quad b_3 = -1. \quad (126)$$

7th order

$$a_0 = -\frac{47}{12}, \quad a_1 = -16, \quad a_2 = 9, \quad a_3 = \frac{32}{3}, \quad a_4 = \frac{1}{4}, \quad b_1 = -12, \quad b_2 = -18, \quad b_3 = -4. \quad (127)$$

8th order

$$\begin{aligned} a_0 &= -\frac{25}{6}, & a_1 &= -\frac{80}{3}, & a_2 &= 0, & a_3 &= \frac{80}{3}, & a_4 &= \frac{25}{6}, \\ b_1 &= -16, & b_2 &= -36, & b_3 &= -16, & b_4 &= -1. \end{aligned} \quad (128)$$

References

- [1] X. Zhong, High-order finite-difference schemes for numerical simulation of hypersonic boundary-layer transition, *J. Comput. Phys.* 144 (1998) 662–709, <https://doi.org/10.1006/jcph.1998.6010>.
- [2] R.L. Kimmel, Aspects of hypersonic boundary-layer transition control, in: *41st Aerosp. Sci. Meet. Exhib., American Institute of Aeronautics and Astronautics, Reno, Nevada, 2003*, p. 772.
- [3] X. Zhong, X. Wang, Direct numerical simulation on the receptivity, instability, and transition of hypersonic boundary layers, *Annu. Rev. Fluid Mech.* 44 (2012) 527–561, <https://doi.org/10.1146/annurev-fluid-120710-101208>.
- [4] T. Ishihara, T. Gotoh, Y. Kaneda, Study of high-Reynolds number isotropic turbulence by direct numerical simulation, *Annu. Rev. Fluid Mech.* 41 (2009) 165–180, <https://doi.org/10.1146/annurev.fluid.010908.165203>.
- [5] P. Moin, K. Mahesh, Direct numerical simulation: a tool in turbulence research, *Annu. Rev. Fluid Mech.* 30 (1998) 539–578, <https://doi.org/10.1146/annurev.fluid.30.1.539>.

- [6] C.K.W. Tam, Computational aeroacoustics – issues and methods, *AIAA J.* 33 (1995) 1788–1796, <https://doi.org/10.2514/3.12728>.
- [7] C. Bogey, C. Bailly, A family of low dispersive and low dissipative explicit schemes for flow and noise computations, *J. Comput. Phys.* 194 (2004) 194–214, <https://doi.org/10.1016/j.jcp.2003.09.003>.
- [8] C.-W. Shu, High order WENO and DG methods for time-dependent convection-dominated PDEs: a brief survey of several recent developments, *J. Comput. Phys.* 316 (2016) 598–613, <https://doi.org/10.1016/j.jcp.2016.04.030>.
- [9] J.A. Ekaterinaris, High-order accurate, low numerical diffusion methods for aerodynamics, *Prog. Aerosp. Sci.* 41 (2005) 192–300, <https://doi.org/10.1016/j.paerosci.2005.03.003>.
- [10] Z.J. Wang, High-order methods for the Euler and Navier–Stokes equations on unstructured grids, *Prog. Aerosp. Sci.* 43 (2007) 1–41, <https://doi.org/10.1016/j.paerosci.2007.05.001>.
- [11] M. Dubiner, Spectral methods on triangles and other domains, *J. Sci. Comput.* 6 (1991) 345–390, <https://doi.org/10.1007/BF01060030>.
- [12] R.D. Moser, P. Moin, A. Leonard, A spectral numerical method for the Navier–Stokes equations with applications to Taylor–Couette flow, *J. Comput. Phys.* 52 (1983) 524–544, [https://doi.org/10.1016/0021-9991\(83\)90006-2](https://doi.org/10.1016/0021-9991(83)90006-2).
- [13] M.Y. Hussaini, T.A. Zang, Spectral methods in fluid dynamics, *Annu. Rev. Fluid Mech.* 19 (1987) 339–367, <https://doi.org/10.1146/annurev.fl.19.010187.002011>.
- [14] B. Cockburn, S.-Y. Lin, C.-W. Shu, TVB Runge–Kutta local projection discontinuous Galerkin finite element method for conservation laws III: one-dimensional systems, *J. Comput. Phys.* 84 (1989) 90–113, [https://doi.org/10.1016/0021-9991\(89\)90183-6](https://doi.org/10.1016/0021-9991(89)90183-6).
- [15] B. Cockburn, C.-W. Shu, The Runge–Kutta discontinuous Galerkin method for conservation laws V: multidimensional systems, *J. Comput. Phys.* 141 (1998) 199–224, <https://doi.org/10.1006/jcph.1998.5892>.
- [16] J. Qiu, M. Dumbser, C.-W. Shu, The discontinuous Galerkin method with Lax–Wendroff type time discretizations, *Comput. Methods Appl. Mech. Eng.* 194 (2005) 4528–4543, <https://doi.org/10.1016/j.cma.2004.11.007>.
- [17] J. Zhu, X. Zhong, C.-W. Shu, J. Qiu, Runge–Kutta discontinuous Galerkin method using a new type of WENO limiters on unstructured meshes, *J. Comput. Phys.* 248 (2013) 200–220, <https://doi.org/10.1016/j.jcp.2013.04.012>.
- [18] S.K. Lele, Compact finite difference schemes with spectral-like resolution, *J. Comput. Phys.* 103 (1992) 16–42, [https://doi.org/10.1016/0021-9991\(92\)90324-R](https://doi.org/10.1016/0021-9991(92)90324-R).
- [19] K. Mahesh, A family of high order finite difference schemes with good spectral resolution, *J. Comput. Phys.* 145 (1998) 332–358, <https://doi.org/10.1006/jcph.1998.6022>.
- [20] R.K. Shukla, X. Zhong, Derivation of high-order compact finite difference schemes for non-uniform grid using polynomial interpolation, *J. Comput. Phys.* 204 (2005) 404–429, <https://doi.org/10.1016/j.jcp.2004.10.014>.
- [21] R.K. Shukla, M. Tatineni, X. Zhong, Very high-order compact finite difference schemes on non-uniform grids for incompressible Navier–Stokes equations, *J. Comput. Phys.* 224 (2007) 1064–1094, <https://doi.org/10.1016/j.jcp.2006.11.007>.
- [22] P.C. Chu, C. Fan, A three-point combined compact difference scheme, *J. Comput. Phys.* 140 (1998) 370–399, <https://doi.org/10.1006/jcph.1998.5899>.
- [23] H.C. Yee, N.D. Sandham, M.J. Djomehri, Low-dissipative high-order shock-capturing methods using characteristic-based filters, *J. Comput. Phys.* 150 (1999) 199–238, <https://doi.org/10.1006/jcph.1998.6177>.
- [24] A. Harten, High resolution schemes for hyperbolic conservation laws, *J. Comput. Phys.* 49 (1983) 357–393, [https://doi.org/10.1016/0021-9991\(83\)90136-5](https://doi.org/10.1016/0021-9991(83)90136-5).
- [25] A. Harten, B. Engquist, S. Osher, S.R. Chakravarthy, Uniformly high order accurate essentially non-oscillatory schemes, III, *J. Comput. Phys.* 71 (1987) 231–303, [https://doi.org/10.1016/0021-9991\(87\)90031-3](https://doi.org/10.1016/0021-9991(87)90031-3).
- [26] X.-D. Liu, S. Osher, T. Chan, Weighted essentially non-oscillatory schemes, *J. Comput. Phys.* 115 (1994) 200–212, <https://doi.org/10.1006/jcph.1994.1187>.
- [27] G.-S. Jiang, C.-W. Shu, Efficient implementation of weighted ENO schemes, *J. Comput. Phys.* 126 (1996) 202–228, <https://doi.org/10.1006/jcph.1996.0130>.
- [28] Y.-X. Ren, M. Liu, H. Zhang, A characteristic-wise hybrid compact-WENO scheme for solving hyperbolic conservation laws, *J. Comput. Phys.* 192 (2003) 365–386, <https://doi.org/10.1016/j.jcp.2003.07.006>.
- [29] L. Zhang, W. Liu, L. He, X. Deng, H. Zhang, A class of hybrid DG/FV methods for conservation laws I: basic formulation and one-dimensional systems, *J. Comput. Phys.* 231 (2012) 1081–1103, <https://doi.org/10.1016/j.jcp.2011.06.010>.
- [30] L. Zhang, W. Liu, L. He, X. Deng, H. Zhang, A class of hybrid DG/FV methods for conservation laws II: two-dimensional cases, *J. Comput. Phys.* 231 (2012) 1104–1120, <https://doi.org/10.1016/j.jcp.2011.03.032>.
- [31] J.J. Choi, Hybrid spectral difference/embedded finite volume method for conservation laws, *J. Comput. Phys.* 295 (2015) 285–306, <https://doi.org/10.1016/j.jcp.2015.04.013>.
- [32] Y. Liu, M. Vinokur, Z.J. Wang, Spectral difference method for unstructured grids I: basic formulation, *J. Comput. Phys.* 216 (2006) 780–801, <https://doi.org/10.1016/j.jcp.2006.01.024>.
- [33] Z.J. Wang, Y. Liu, G. May, A. Jameson, Spectral difference method for unstructured grids II: extension to the Euler equations, *J. Sci. Comput.* 32 (2007) 45–71, <https://doi.org/10.1007/s10915-006-9113-9>.
- [34] A. Balan, G. May, J. Schöberl, A stable high-order spectral difference method for hyperbolic conservation laws on triangular elements, *J. Comput. Phys.* 231 (2012) 2359–2375, <https://doi.org/10.1016/j.jcp.2011.11.041>.
- [35] Z.J. Wang, Spectral (finite) volume method for conservation laws on unstructured grids: basic formulation, *J. Comput. Phys.* 178 (2002) 210–251, <https://doi.org/10.1006/jcph.2002.7041>.
- [36] Y. Liu, M. Vinokur, Z.J. Wang, Spectral (finite) volume method for conservation laws on unstructured grids V: extension to three-dimensional systems, *J. Comput. Phys.* 212 (2006) 454–472, <https://doi.org/10.1016/j.jcp.2005.06.024>.
- [37] Y. Sun, Z.J. Wang, Y. Liu, Spectral (finite) volume method for conservation laws on unstructured grids VI: extension to viscous flow, *J. Comput. Phys.* 215 (2006) 41–58, <https://doi.org/10.1016/j.jcp.2005.10.019>.
- [38] Z.J. Wang, Y. Liu, Extension of the spectral volume method to high-order boundary representation, *J. Comput. Phys.* 211 (2006) 154–178, <https://doi.org/10.1016/j.jcp.2005.05.022>.
- [39] Z. Haras, S. Ta’asan, Finite difference schemes for long-time integration, *J. Comput. Phys.* 114 (1994) 265–279, <https://doi.org/10.1006/jcph.1994.1165>.
- [40] C. Ashcroft, X. Zhang, Optimized prefactored compact schemes, *J. Comput. Phys.* 190 (2003) 459–477, [https://doi.org/10.1016/S0021-9991\(03\)00293-6](https://doi.org/10.1016/S0021-9991(03)00293-6).
- [41] R. Hixon, Prefactored small-stencil compact schemes, *J. Comput. Phys.* 165 (2000) 522–541, <https://doi.org/10.1006/jcph.2000.6631>.
- [42] J.W. Kim, D.J. Lee, Optimized compact finite difference schemes with maximum resolution, *AIAA J.* 34 (1996) 887–893, <https://doi.org/10.2514/3.13164>.
- [43] X. Liu, S. Zhang, H. Zhang, C.-W. Shu, A new class of central compact schemes with spectral-like resolution I: linear schemes, *J. Comput. Phys.* 248 (2013) 235–256, <https://doi.org/10.1016/j.jcp.2013.04.014>.
- [44] P.C. Chu, C. Fan, A three-point sixth-order nonuniform combined compact difference scheme, *J. Comput. Phys.* 148 (1999) 663–674, <https://doi.org/10.1006/jcph.1998.6141>.
- [45] Y.G. Bhumkar, T.W.H. Sheu, T.K. Sengupta, A dispersion relation preserving optimized upwind compact difference scheme for high accuracy flow simulations, *J. Comput. Phys.* 278 (2014) 378–399, <https://doi.org/10.1016/j.jcp.2014.08.040>.
- [46] C. Cheong, S. Lee, Grid-optimized dispersion-relation-preserving schemes on general geometries for computational aeroacoustics, *J. Comput. Phys.* 174 (2001) 248–276, <https://doi.org/10.1006/jcph.2001.6904>.
- [47] M.K. Rajpoot, T.K. Sengupta, P.K. Dutt, Optimal time advancing dispersion relation preserving schemes, *J. Comput. Phys.* 229 (2010) 3623–3651, <https://doi.org/10.1016/j.jcp.2010.01.018>.

- [48] T.K. Sengupta, V. Lakshmanan, V.V.S.N. Vijay, A new combined stable and dispersion relation preserving compact scheme for non-periodic problems, *J. Comput. Phys.* 228 (2009) 3048–3071, <https://doi.org/10.1016/j.jcp.2009.01.003>.
- [49] C.K.W. Tam, J.C. Webb, Dispersion-relation-preserving finite difference schemes for computational acoustics, *J. Comput. Phys.* 107 (1993) 262–281, <https://doi.org/10.1006/jcph.1993.1142>.
- [50] G. Cunha, S. Redonnet, On the effective accuracy of spectral-like optimized finite-difference schemes for computational aeroacoustics, *J. Comput. Phys.* 263 (2014) 222–232, <https://doi.org/10.1016/j.jcp.2014.01.024>.
- [51] X. Zhong, M. Tatineni, High-order non-uniform grid schemes for numerical simulation of hypersonic boundary-layer stability and transition, *J. Comput. Phys.* 190 (2003) 419–458, [https://doi.org/10.1016/S0021-9991\(03\)00282-1](https://doi.org/10.1016/S0021-9991(03)00282-1).
- [52] S. Pirozzoli, On the spectral properties of shock-capturing schemes, *J. Comput. Phys.* 219 (2006) 489–497, <https://doi.org/10.1016/j.jcp.2006.07.009>.
- [53] S. Pirozzoli, Numerical methods for high-speed flows, *Annu. Rev. Fluid Mech.* 43 (2011) 163–194, <https://doi.org/10.1146/annurev-fluid-122109-160718>.
- [54] C.-W. Shu, High order weighted essentially nonoscillatory schemes for convection dominated problems, *SIAM Rev.* 51 (2009) 82–126, <https://doi.org/10.1137/070679065>.
- [55] D.J. Hill, D.I. Pullin, Hybrid tuned center-difference-WENO method for large eddy simulations in the presence of strong shocks, *J. Comput. Phys.* 194 (2004) 435–450, <https://doi.org/10.1016/j.jcp.2003.07.032>.
- [56] E.M. Taylor, M. Wu, M.P. Martín, Optimization of nonlinear error for weighted essentially non-oscillatory methods in direct numerical simulations of compressible turbulence, *J. Comput. Phys.* 223 (2007) 384–397, <https://doi.org/10.1016/j.jcp.2006.09.010>.
- [57] M.D. Salas, *A Shock-Fitting Primer*, CRC Press, 2009.
- [58] A. Prakash, N. Parsons, X. Wang, X. Zhong, High-order shock-fitting methods for direct numerical simulation of hypersonic flow with chemical and thermal nonequilibrium, *J. Comput. Phys.* 230 (2011) 8474–8507, <https://doi.org/10.1016/j.jcp.2011.08.001>.
- [59] P.S. Rawat, X. Zhong, On high-order shock-fitting and front-tracking schemes for numerical simulation of shock–disturbance interactions, *J. Comput. Phys.* 229 (2010) 6744–6780, <https://doi.org/10.1016/j.jcp.2010.05.021>.
- [60] J. Qiu, C.-W. Shu, Hermite WENO schemes and their application as limiters for Runge–Kutta discontinuous Galerkin method: one-dimensional case, *J. Comput. Phys.* 193 (2004) 115–135, <https://doi.org/10.1016/j.jcp.2003.07.026>.
- [61] J. Qiu, C.-W. Shu, Hermite WENO schemes and their application as limiters for Runge–Kutta discontinuous Galerkin method II: two dimensional case, *Comput. Fluids* 34 (2005) 642–663, <https://doi.org/10.1016/j.compfluid.2004.05.005>.
- [62] J. Zhu, J. Qiu, Hermite WENO schemes and their application as limiters for Runge–Kutta discontinuous Galerkin method, III: unstructured meshes, *J. Sci. Comput.* 39 (2009) 293–321, <https://doi.org/10.1007/s10915-009-9271-7>.
- [63] D.S. Balsara, C. Altmann, C.-D. Munz, M. Dumbser, A sub-cell based indicator for troubled zones in RKDG schemes and a novel class of hybrid RKDG+HWENO schemes, *J. Comput. Phys.* 226 (2007) 586–620, <https://doi.org/10.1016/j.jcp.2007.04.032>.
- [64] H. Luo, J.D. Baum, R. Löhrner, A Hermite WENO-based limiter for discontinuous Galerkin method on unstructured grids, *J. Comput. Phys.* 225 (2007) 686–713, <https://doi.org/10.1016/j.jcp.2006.12.017>.
- [65] H. Luo, Y. Xia, S. Li, R. Nourgaliev, C. Cai, A Hermite WENO reconstruction-based discontinuous Galerkin method for the Euler equations on tetrahedral grids, *J. Comput. Phys.* 231 (2012) 5489–5503, <https://doi.org/10.1016/j.jcp.2012.05.011>.
- [66] H. Luo, Y. Xia, S. Spiegel, R. Nourgaliev, Z. Jiang, A reconstructed discontinuous Galerkin method based on a hierarchical WENO reconstruction for compressible flows on tetrahedral grids, *J. Comput. Phys.* 236 (2013) 477–492, <https://doi.org/10.1016/j.jcp.2012.11.026>.
- [67] S.-C. Chang, The method of space–time conservation element and solution element—a new approach for solving the Navier–Stokes and Euler equations, *J. Comput. Phys.* 119 (1995) 295–324, <https://doi.org/10.1006/jcph.1995.1137>.
- [68] S.-C. Chang, X.-Y. Wang, W.-M. To, Application of the space–time conservation element and solution element method to one-dimensional convection–diffusion problems, *J. Comput. Phys.* 165 (2000) 189–215, <https://doi.org/10.1006/jcph.2000.6610>.
- [69] Z.-C. Zhang, S.T.J. Yu, S.-C. Chang, A space–time conservation element and solution element method for solving the two- and three-dimensional unsteady Euler equations using quadrilateral and hexahedral meshes, *J. Comput. Phys.* 175 (2002) 168–199, <https://doi.org/10.1006/jcph.2001.6934>.
- [70] D.S. Sundar, K.S. Yeo, A high order meshless method with compact support, *J. Comput. Phys.* 272 (2014) 70–87, <https://doi.org/10.1016/j.jcp.2014.04.010>.
- [71] H. Nishikawa, A first-order system approach for diffusion equation. I: second-order residual-distribution schemes, *J. Comput. Phys.* 227 (2007) 315–352, <https://doi.org/10.1016/j.jcp.2007.07.029>.
- [72] H. Nishikawa, A first-order system approach for diffusion equation. II: unification of advection and diffusion, *J. Comput. Phys.* 229 (2010) 3989–4016, <https://doi.org/10.1016/j.jcp.2009.10.040>.
- [73] H. Nishikawa, First-, second-, and third-order finite-volume schemes for diffusion, *J. Comput. Phys.* 256 (2014) 791–805, <https://doi.org/10.1016/j.jcp.2013.09.024>.
- [74] H. Nishikawa, First, second, and third order finite-volume schemes for advection–diffusion, *J. Comput. Phys.* 273 (2014) 287–309, <https://doi.org/10.1016/j.jcp.2014.05.021>.
- [75] T.J. Poinso, S.K. Lele, Boundary conditions for direct simulations of compressible viscous flows, *J. Comput. Phys.* 101 (1992) 104–129, [https://doi.org/10.1016/0021-9991\(92\)90046-2](https://doi.org/10.1016/0021-9991(92)90046-2).
- [76] N.L. Mundis, A.K. Edoh, V. Sankaran, Highly-accurate filter-based artificial-dissipation schemes for stiff unsteady fluid systems, in: 54th AIAA Aerosp. Sci. Meet., American Institute of Aeronautics and Astronautics, San Diego, California, 2016, pp. 1–22.
- [77] A.K. Edoh, N.L. Mundis, A.R. Karagozian, V. Sankaran, The role of dispersion and dissipation on stabilization strategies for time-accurate simulations, in: 54th AIAA Aerosp. Sci. Meet., American Institute of Aeronautics and Astronautics, San Diego, California, 2016, pp. 1–26.
- [78] S. Hu, X. Zhong, Linear stability of viscous supersonic plane Couette flow, *Phys. Fluids* 10 (1998) 709–729, <https://doi.org/10.1063/1.869596>.